UAB

Universitat Autònoma de Barcelona

UAB
Universitat Autònoma de Barcelona

Thesis submitted for the Doctoral Degree from

UNIVERSITAT AUTÒNOMA DE BARCELONA

PhD Program in Materials Science

Plasmon-induced photocurrent generation in metal-semiconductor devices with nanofabricated inverted pyramid arrays

Jinhui HU

Under the supervision of:

Maria Isabel Alonso Carmona (Director)   **Alejandro Rodolfo Goñi (Director)**

Agustín Mihi (Tutor)

Institut de Ciència de Materials de Barcelona

(ICMAB-CSIC)

September 2022

ICMAB

CSIC
CONSEJO SUPERIOR DE INVESTIGACIONES CIENTÍFICAS

Abstract

One of the main challenges in harvesting the near-infrared (NIR) region of the solar spectrum that is wasted by any solar cell, due to the limitation in bandgap that prevents photovoltaic generation, is to exploit alternative ways of photocurrent generation. Despite the great potential shown by photonic/plasmonic architectures in terms of their optoelectronic performance, implementation in devices is still hampered by their low photocurrent generation efficiency and the expensive and low throughput fabrication techniques involved. Therefore, this thesis is devoted to the design and development of NIR light harvesters to improve photocurrent generation while using scalable nanostructuration methodologies such as soft nanoimprint lithography (NIL).

The transparency of silicon in the NIR enables the design of nano/microstructures for implementation in devices to harvest the infrared part of the solar spectrum. Here a strategy is reported that uses arrays of inverted silicon pyramids covered with a thin gold film, which exhibit substantial light absorption in the NIR, below the gap of Si. The absorption stems from the resonant excitation of surface-plasmons at the metal/dielectric interface. The optimization of size and separation of the inverted pyramids proceeded by iteration of the calculation and measurement of the infrared response using finite difference time-domain simulations and Fourier-transform IR spectroscopy, respectively. The calculated near-field distributions are analyzed specifically looking for the presence of hot spots, i.e. nano-sized regions of very high concentration of the electronic charge and strong electromagnetic field enhancement, and their potential for hot-electron generation is discussed.

Furthermore, oblique-angle evaporation was implemented for the fabrication of Si pyramids with partial number of facets covered with gold, which display similar behavior as the fully covered pyramids (4-facet) already studied but which, due to the lower symmetry, exhibit intense hot spots at the apex of the 3-facet covered pyramids. Interestingly, the optical response of the 3-facets and 2-facets Au covered pyramids appears to be strongly dependent

Abstract

on the linear polarization of the incident light, which provides a means to tune the response of the devices, besides varying pyramid size and array pitch. Numerical simulations show that in small size 3-facets pyramids (200 – 300 nm), the hot spots are characterized by electric-field vectors perpendicular to the metal surface, which is a prerequisite for efficient hot-electron emission.

The photoelectrical characterization of Au/Si inverted-pyramid devices with different number of facets covered with gold demonstrates that they can exhibit remarkable responsivity both in the region above and below the Si bandgap, which can be explained by the mechanisms of plasmon-induced resonance energy transfer (PIRET) and hot electron generation, respectively. The magnitude of the hot-electron photocurrents of the 3-facets devices is five times larger than that of the 4-facets counterparts. Homogeneous NIR photo-response is obtained across the whole patterned area of 0.5 cm^2 below the Si bandgap. The photocurrent maps as a function of polarization azimuthal angle in the measured spectral range below Si bandgap exhibit exactly the C_2 symmetry as the absorbance maps.

The concepts were extended to the fabrication of devices using polymeric materials such as the n-type organic semiconductor N2200. A method called "wet embossing" is reported that uses soft nanoimprint lithography to engrave the polymer with the inverted pyramid array during the drying process. Again, strong and tunable absorption below the gap of the polymer is observed, which stems from the resonant excitation of surface-plasmons, also presenting hot spots distributed along the Au/N2200 interface. The photoelectrical response of Au/N2200 devices is similar to that of the Au/Si counterparts, yielding comparable responsivities and remarkable photocurrents in the measured spectral range from visible to NIR, once more corresponding to PIRET and hot-electron generation mechanisms working synergistically.

Acknowledgements

I want to give my deep appreciation to many people who have given me a lot of help during my thesis researches. This thesis cannot be finished without their great help and guidance.

First of all, I would like to give my greatest gratitude to my supervisors, Professor Maria Isabel Alonso Carmona and Professor Goñi Alejandro Rodolfo. They gave me the opportunity to join their group four years ago when I applied for PhD study. In the past four years, they led me into a very interesting research field. When I encountered difficulties in my studies, they always encourage and guide me patiently. Their rigorous attitude and everlasting passion towards scientific research and optimistic attitude towards life are deeply affecting me and making me mature in scientific research and life. I deeply feel so lucky and honored to be one of their postgraduate students.

I would also like to thank my accomplished and kind tutor Professor Agustín Mihi, he gave me a lot of useful suggestion and guidance when I had difficulties with my experiments.

I also want to express my appreciation to our present and previous group members. They gave me a lot of help both in studies and daily life. Dr. Juan Luis Garcia-Pomar helped me with the numerical simulation. Dr. Luis Alberto Pérez taught me the electrical measurement of devices and other characterization methods also gave me many valuable suggestions on experiments. Dr. Pau Molet helped me with the fabrication of soft and hard stamps. Mr. Miquel Casademont gave me a lot of help during the electrical measurement. Without their great help, this thesis could not have reached the present stage. I would like to thank Professor Sebastián Reparaz, Professor Miquel Garriga, Professor Mariano Campoy-Quiles for their useful suggestions about my expeirments and also Mr. Xukai, Miss Minghua Kong, Dr. Camilla Dore, Dr. Mayte Gómez-Castaño, Dr. Martí Gibert-Roca, Mr. Albert Harillo for their kind assistance in my experiments and life.

Last, numerous thanks are given to my family members. Your understanding and support are extremely important to my life. Every success obtained in my life contains your dedication.

Contents

Chapter 1

Introduction (Theoretical background)

1.1 Light matter interaction

From ancient times to nowadays, light consistently plays an essential role in the life of biological species from photosynthesis of plants to the visual information that humans perceive with their eyes and other countless examples. With the development of modern technology, scientists can handle the light in the whole electromagnetic spectrum from gamma rays to the radio waves, which has brought considerable progresses to our daily life. The interaction between light and matter is a key branch of optical and photonics science that has vast applications on the fields of physics, chemistry, biology, and medicine. Therefore, exploring the mechanism of interaction of light with matter further engineering their optical and electromagnetic properties have become of considerable interest for scientific research.

In the past decades, as the research focus has shifted from microscale to nanoscale, the unprecedented capability of light concentration and manipulation has been explored by coupling the light to nanostructured materials, realizing significant optical responses and field enhancements, which provide promising potential to develop the fields of nonlinear optics [1], photocatalysis [2],[3], solar energy harvesting [4], and sensing [5]. This is the case of metamaterials and other designed light management nanomaterials that offer unique optical and electromagnetic responses. Generally, metamaterials are artificial arrangements with periodic structure which achieve unique electromagnetic functionalities from the unit structure rather than from the properties of the constituent materials. That is, metamaterials can be tailored to display electromagnetic responses beyond those accessible to natural limits such as a negative refractive index and optical magnetism. Exploration and utilization of such atypical properties could bridge the gap between the conventional optics and the nanoworld with exciting capabilities from subwavelength focusing to invisibility cloaking, from biophotonics to nanocircuitry in the fields of science and engineering.

In this chapter, I will introduce the theoretical concepts related to the interaction of light with matter of interest for the metamaterials studied in this work. First, starting with the fundamentals of light as electromagnetic waves that propagate in the medium. Then, I consider the optical properties of metal, semiconductors and dielectric materials. In this thesis, the main focus is on the coupling phenomena occurring at metal-semiconductor interfaces.

1.1.1 Fundamentals of light: Electromagnetic wave propagation

The modern electromagnetic theory of light emerged from developments contributed by James Clerk Maxwell in the 1860s. Some years later, Josiah Willard Gibbs and Oliver Heaviside independently formulated the vectorial forms commonly used nowadays. Originally, Maxwell published two famous papers: "On Physical Lines of Force" and "A Dynamical Theory of the Electromagnetic Field". In his theory, he unified the concepts of light, electricity and magnetism, which were later compiled into the four differential equations that are now known as Maxwell's equations. They establish the unifying connection between electromagnetic waves and light, from the extremely long wavelength of radio waves to ultra-short ultraviolet light. Maxwell's equations describe the spatial and temporal propagation of an electromagnetic wave within a material:

$$\nabla \cdot \vec{D} = \rho \tag{1.1}$$

$$\nabla \cdot \vec{B} = 0 \tag{1.2}$$

$$\nabla \times \vec{E} = -\frac{\partial \vec{B}}{\partial t} \tag{1.3}$$

$$\nabla \times \vec{H} = \frac{\partial \vec{D}}{\partial t} + \vec{J} \tag{1.4}$$

Here $\vec{D}$ is the electric displacement, $\vec{B}$ is the magnetic induction, $\vec{E}$ is the electric field, $\vec{H}$ is the magnetic field, ρ is the free charge density and $\vec{J}$ is the current density. In a linear and isotropic medium, the electric displacement $\vec{D}$ and magnetic induction $\vec{B}$ are constituted by two terms: one component is the electromagnetic wave in vacuum and the other is the

polarization ($\vec{P}$) or magnetization ($\vec{M}$), respectively. The constitutive relations are denoted as follows:

$$\vec{D} = \varepsilon_0 \vec{E} + \vec{P} = \varepsilon_0 \varepsilon \vec{E} \qquad (1.5)$$

$$\vec{B} = \mu_0 \vec{H} + \vec{M} = \mu_0 \mu \vec{H} \qquad (1.6)$$

Where ε_0 is the vacuum electric permittivity, μ_0 is the vacuum magnetic permeability. The overall response can be expressed by the relative electric permittivity ε and relative magnetic permeability μ of the medium. Both ε and μ are dimensionless complex numbers (strictly speaking, both are second-rank tensors), depending on the frequency of radiation. The real part illustrates the strength of polarization or the magnetization and the imaginary part describes the absorption loss in the material.

$$\varepsilon = \varepsilon' + i\varepsilon'' \qquad (1.7)$$

$$\mu = \mu' + i\mu'' \qquad (1.8)$$

These two parameters are related to the interaction of the electromagnetic wave with the medium, and by using those two parameters one can describe the response of an electromagnetic wave to a medium: the refractive index n and wave impedance z.

$$n = \sqrt{\varepsilon\mu} \qquad (1.9)$$

$$z = \sqrt{\frac{\mu}{\varepsilon}} \qquad (1.10)$$

The refractive index n is the ratio of the speed of light c in vacuum to its speed v in the medium: n = c/v. The wave impedance z refers to the resistance of material to the wave propagation. These parameters are used to characterize the interaction of light and matter. Therefore, it is necessary to determine their values before designing devices and select suitable material combinations for applications, for example to achieve strong light confinement, high absorption, high transmission, low reflection or other optical functionalities.

1.1.2 Optical properties of materials

One of the most important optical constants of a material is its refractive index which is related to its relative permittivity and relative magnetic permeability. When we work at optical frequencies, i.e. the visible (VIS) and near infrared (NIR) ranges, the medium shows negligible magnetization compared with the electric counterpart. Thus, the relative magnetic permeability of the medium can be taken as $\mu = 1$ and Eq. (1.9) simplifies to $n = \sqrt{\varepsilon}$. In the structures designed in this thesis, we combine material blocks with dimensions in hundreds of nanometers. In this size range, the dielectric constants can still be regarded as that of the bulk. In this doctoral thesis, the optical properties of metals and semiconductors are the key research objects.

1.1.2.1 Optical properties of metals

For metallic materials, their optical responses mainly come from the conduction electrons, endowing them with distinctive shinny appearance. As shown in Figure 1.1, the real part of the electric permittivity $Re(\varepsilon)$ for gold remains negative through the displayed wavelength range. The negative sign can be understood as free electrons oscillating out of phase with the electric field, thus shielding the electromagnetic wave and resulting in a reflectivity that approaches 1. However, when the frequency of incident light is higher than the plasma frequency ω_P, accounting for the oscillations of free electrons it is usually located in the ultraviolet (UV) region, the electrons fail to follow the oscillation of electromagnetic field. In this instance, the metal loses the reflectivity and electromagnetic radiation can penetrate into the bulk despite of its normally high damping.
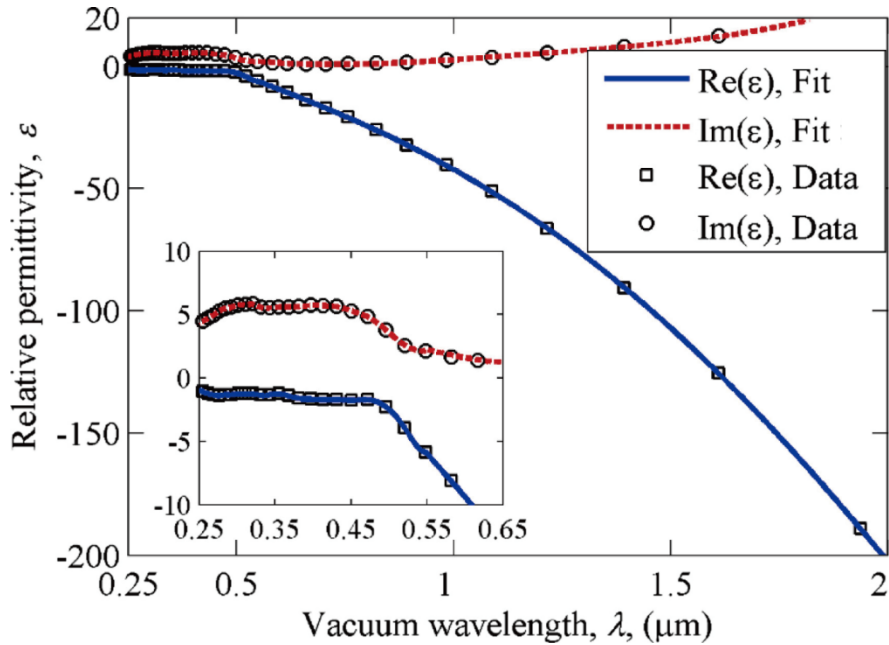
Figure 1.1: The real and imaginary parts of the relative permittivity of gold are plotted as the function of the wavelength from 250 nm to 2 μm. The inset shows in greater detail the material dispersion in the visible and UV ranges [6].

In this thesis, gold is used in the devices for three main purposes. One is the excitation of surface plasmons (SPs) in gold film for hot electron generation from non-radiative decay of SPs and the injection into semiconductor. Another purpose is the surface plasmon energy generated on the nanostructured gold film is directly transferred non-radiatively to the semiconductor through dipole-diople interaction, locally generating electron-hole pairs in the semiconductor. The photocurrent is obtained by the collection of electrons and holes in the electrons. The third purpose is acting as an anti-transmission layer on the metal/semiconductor interface to fully concentrate the incident light in the nanostructured gold film for achieving high absorption.

1.1.2.2 Optical properties of dielectrics and semiconductors

The magnetization of a medium is quite weaker than its electric counterpart at optical frequencies and can be neglected. So, the relative permeability can be regarded as $\mu = 1$ when the magnetic induction approaches the free space and the refractive index gives a simplified

value to n = $\sqrt{\varepsilon}$. Regarding the refractive index, for this thesis and in terms of the materials in the devices, we can distinguish of two types of materials: dielectrics and semiconductors with low and high refractive index.

Dielectrics are materials typically with low refractive index (1 < n < 2) such as glass, diamond, quartz, many metal oxides, resins and polymers. Most of these dielectrics are transparent, with nearly constant permittivity and insignificant imaginary part from visible to mid-infrared range. Due to the lack of absorption within the materials, dielectrics are widely used in the optical elements and antireflection coatings.
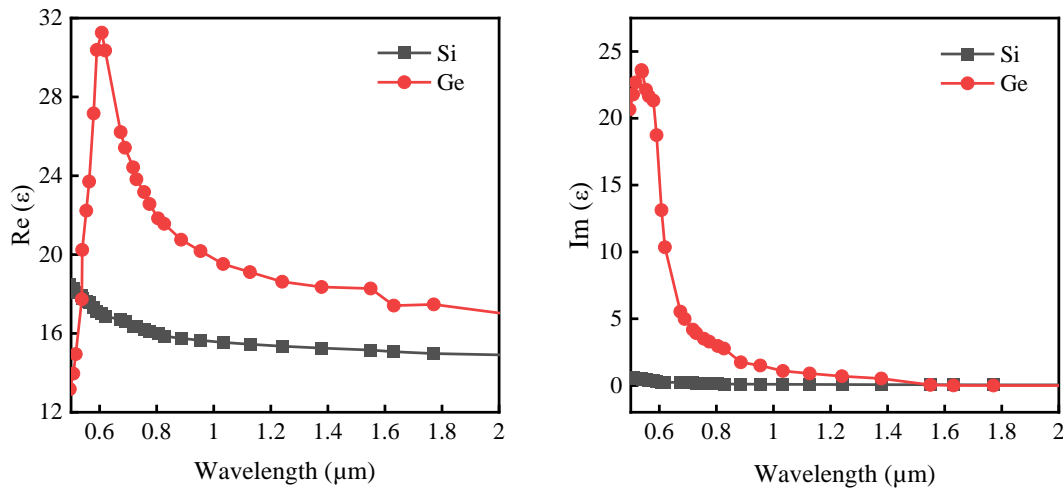
Figure 1.2: Comparison of the permittivity: real (a) and imaginary (b) part of Silicon and Germanium from visible to near infrared. Adapted from Palik handbook [7].

In practice, the optical properties of semiconductor materials lie between those of metals and insulating dielectrics. Semiconductors are materials with usually high refractive index (n > 2). Light in these media is significantly slowed down than in the vacuum. In the near infrared spectral region, semiconductors are normally transparent and having absorption in visible wavelength region, whereas, the dielectric materials show strong absorption in ultraviolet range. The bandgap of semiconductors is located approximately between 0.5 eV ($\lambda \sim 2500$ nm) and 2.5 eV ($\lambda \sim 500$ nm). In this energy range around bandgap, semiconductors display a behavior, ideally, from high transparency to total opacity. Because of the high refractive index of semiconductors that slows down the light traveling in the medium, they are good

candidates for having strong light-matter interaction and light trapping. Semiconductors such as silicon and germanium are low band gap materials with refractive index larger than 3. Both of them show a non-negligible imaginary part of refractive index in the visible region, this is the reason of light absorption (Figure 1.2). Strong absorption in the visible region makes them play a role in the area of photovoltaic [8], they also have applications in the NIR wavelength range such as photodetector [9],[10] due to the low losses required. The intense light trapping in visible and low energy dissipation in NIR range make them appealing materials for metamaterials [11], photonics [12], etc.

1.2 Surface plasmons

Surface plasmons (SPs) give a way to enhance the interaction of light with matter by the collective oscillation of electrons that can give rise to strong electromagnetic fields at the surface of metal nanostructures. Actually, it has been more than a thousand year's history of using light scattering and absorption inherent in the SPs by the combination of precious metal particles with glass to make stained glass vessels and windows. Recently, photonics and plasmonics based on SPs have been adopted to enhance the interaction of light and matter at the level of nanoscale via manipulating light emission [13], propagation [14] and concentration [15]. Plasmonics have become a research hot topic with plentiful applications such as metamaterials [16],[17], cloaking [18] and lasers [19]. Meanwhile, plasmonics also have been employed to improve the performances of photodetectors [10],[20],[21], photovoltaic devices [22],[23] and sensors [24],[25]. There are two existing modes of SPs: either local surface plasmon resonances that are confined to the surface of metal nanoparticle or propagating surface plasmon polaritons on planar interface. In this chapter, both local surface plasmon resonances and surface plasmon polaritons will be introduced.

1.2.1 Localized surface plasmon resonance

Localized surface plasmon resonance (LSPR) is an optical phenomenon generated by the collective oscillation of free electrons in metal nanostructures under excitation with an
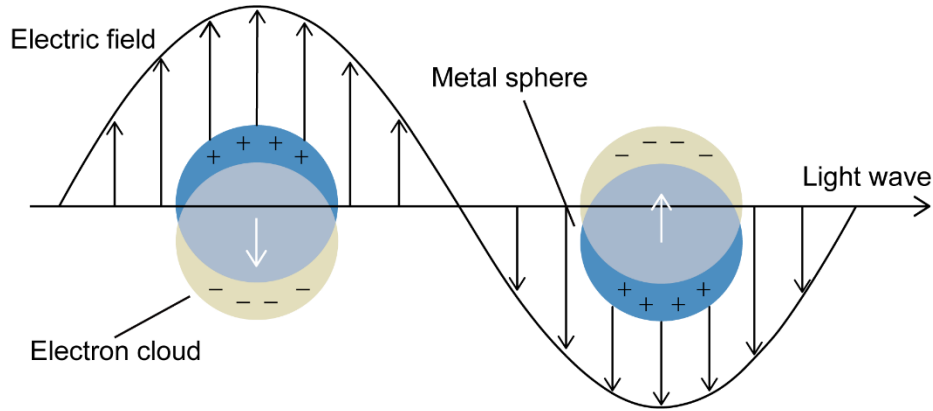
Figure 1.3: Representation of localized surface plasmon resonance in metal nanoparticles.

external electromagnetic field, such that the mutual excitation of electron movement and electromagnetic field produces the resonant oscillation (Figure 1.3). The earliest prototypical application of LSPRs can be dated to the famous Lycurgus Cup that was manufactured in Roman times by embedding glass with nanoscale gold and silver particles, and which are now exhibited at the British museum (see Figure 1.4). Due to the surface plasmon excitation of metallic nanoparticles inside the glass under the illumination of light, the color of Lycurgus Cup changes with the change in location of the source. The cup shows a greenish color when the source is outside the cup and a reddish color when the source is placed inside the cup, which mainly stems from the absorption and scattering effects of light in different wavelength ranges. Up to now, numerous researches in different areas have been developed based on the LSPR of noble metal nanostructures such as biosensor [26]–[28], catalysis [29], and enhanced Raman spectroscopy [29],[30]. The properties of LSPR are highly dependent on the material used and also the shape, size, composition and dielectric environment of metallic nanostructure involved. By manipulating these parameters, the LSPR band wavelength can be tuned throughout the visible, near infrared even to the far infrared spectral region, allowing particular applications where a specific wavelength is desired.

Figure 1.4: The Lycurgus cup, 4th century A.D. The cup shows greenish colour when irradiate from outside (left), and reddish colour when irradiated in the cup (right) [31].

1.2.2 Surface plasmon polaritons

Surface plasmon polaritons (SPPs) are the collective excitation of electrons that travel in a wavelike manner at the interface between a metal and a dielectric with exponential field decay normal to the interface [32]. When the photons are coupled with the free electrons in the metal and satisfy the momentum matching, a surface wave will be generated at the interface between the metal and the dielectric medium. This surface wave consists of the electromagnetic wave propagating in the dielectric and the electron oscillation inside the metal (Figure 1.5a). Waves of SPPs have a short wavelength and a highly localized electromagnetic field enhancement, enabling them to play an important role in nonlinear optics, sensors, optical imaging and plasmonic waveguides [33]–[38]. The characteristics of SPPs are usually determined by the dielectric functions of both metal and dielectric and the frequency of excitation of the light. By regulating those parameters, electromagnetic characteristics of SPPs can be adjusted accordingly. Different from the propagating behaviour of SPPs along the interface, the electric field component perpendicular to the interface of SPPs decays exponentially as the distance from the surface increases. The exponential decay into both media (metal and dielectric) in the perpendicular direction is known as evanescent behaviour or near field characteristic, and exhibits non-radiative attribute of SPPs (Figure 1.5b). SPPs exhibit shorter wavelength and higher frequency than

the incident light, which is the reason that SPPs have better spatial confinement ability and local field enhancement than the ordinary light source. Therefore, it is quite important to master the methods for excitation and regulation of SPPs theoretically. In the following, I will introduce how SPPs are excited, and which are the different modes of SPPs.
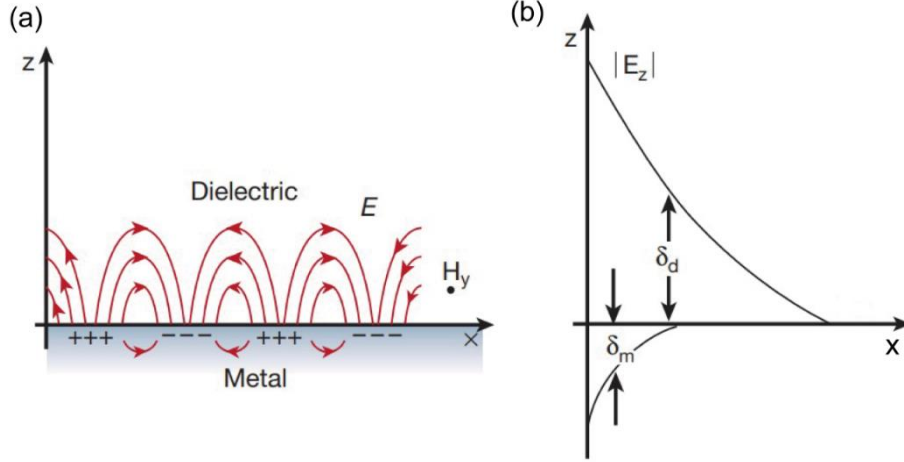
Figure 1.5: (a) Drawing of surface plasmon polaritons (SPPs) at the metal/dielectric interface to illustrate the hybrid mode of electromagnetic fields and surface charges. (b) The electric field components of SPPs decrease exponentially as vertical distances from the interface increase [14].

To comprehend how SPPs are excited, the dispersion relation between wave frequency (ω) and wavevector ($k_{//}$) parallel to interface (the propagation direction) is derived from Maxwell's equation [39], reading as:

$$k_{//} = \frac{\omega}{c} \sqrt{\frac{\varepsilon_d \varepsilon_m}{(\varepsilon_d + \varepsilon_m)}} \qquad (1.11)$$

$$\frac{\omega}{c} = k_0 = \frac{2\pi}{\lambda_0} \qquad (1.12)$$

where ε_d and ε_m are the frequency dependent dielectric functions of dielectric medium and metal, respectively, c is the speed of light in vacuum, k_0 is the wavevector in vacuum and λ_0 corresponds to the wavelength in vacuum.

From the dispersion relation of the SPPs at metal/dielectric interface, Maxwell equations and the boundary conditions of electromagnetic wave on the metal/dielectric interface [32], we obtain that SPPs can only propagate in form of transverse magnetic (TM) polarized waves, i.e. with magnetic field component perpendicular to the propagation plane, whereas transversal electric (TE) polarization mode doesn't exist in SPPs. Figure 1.6 shows in brown the dispersion relation for the photons in free space, while in purple (green) the dispersion relation for the confined (radiative) plasma waves is shown. The dispersion displays two kinds of modes with high energy (green) and low energy (purple). The low energy mode corresponds to a propagating interface wave with exponential decay as shown in Fig. 1.5 (b). The conditions to excite SPPs usually work in visible and near infrared region. The high energy mode, also called Brewster mode, it does not refer to a surface wave but a radiation mode without exponential decay. When $\omega < \omega_{SP}$, the dispersion curve of the low energy mode lies to the right, approaching the dispersion curve of light line. This implies that SPPs have higher wavevector than the light waves at the same frequency. At higher frequencies, SPPs deviate from the light line until it gets to an asymptotic resonant frequency ω_{SP}. When $\omega > \omega_P$, the wave propagates as it travels in the ordinary positive dielectric medium, as given by the theory of Drude. The excitation of SPPs on the interface can confine electromagnetic radiations beyond the diffraction limit, thus, paving the way for the light management at nanoscale.
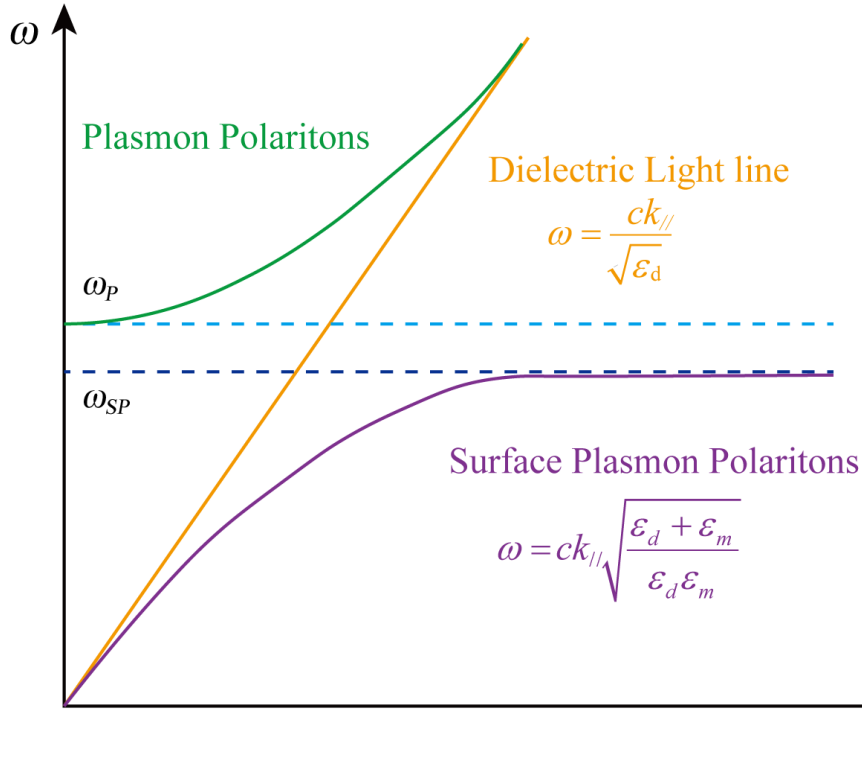
Figure 1.6: Dispersion curves of plasmon-polaritons for an ideal metal/dielectric combination. The mode in green is a propagating wave in the metal, whereas the mode in purple are SPPs of the ideal metal/dielectric interface.

Without damping, high momentum states present in the dispersion of SPPs give a high density of states (DOS) in a narrow frequency region, which affords the research area of "plasmonics" promising traits for applications in the fields of optical sensing and surface-enhanced spectroscopy [40] and other scenarios [15],[41]. However, in view of damping in the propagation of SPPs, which is the actual condition in a metal due to the presence of interband and intraband transitions of electrons, the dispersion curve shows a back-bending behavior (Figure 1.7). This anomalous dispersion has been obtained experimentally by Arakawa et al. [42],[43] However, in real conditions, surface waves are damped through the absorption in the metal with an exponential decay of field intensity. Once the light is converted to the SPPs mode, it propagates along the surface of metal but gradually attenuates due to the absorption losses in the metal. The propagation length of SPPs is thereby restricted by the imaginary part of the SPPs wavevector ($k_{//i}$).
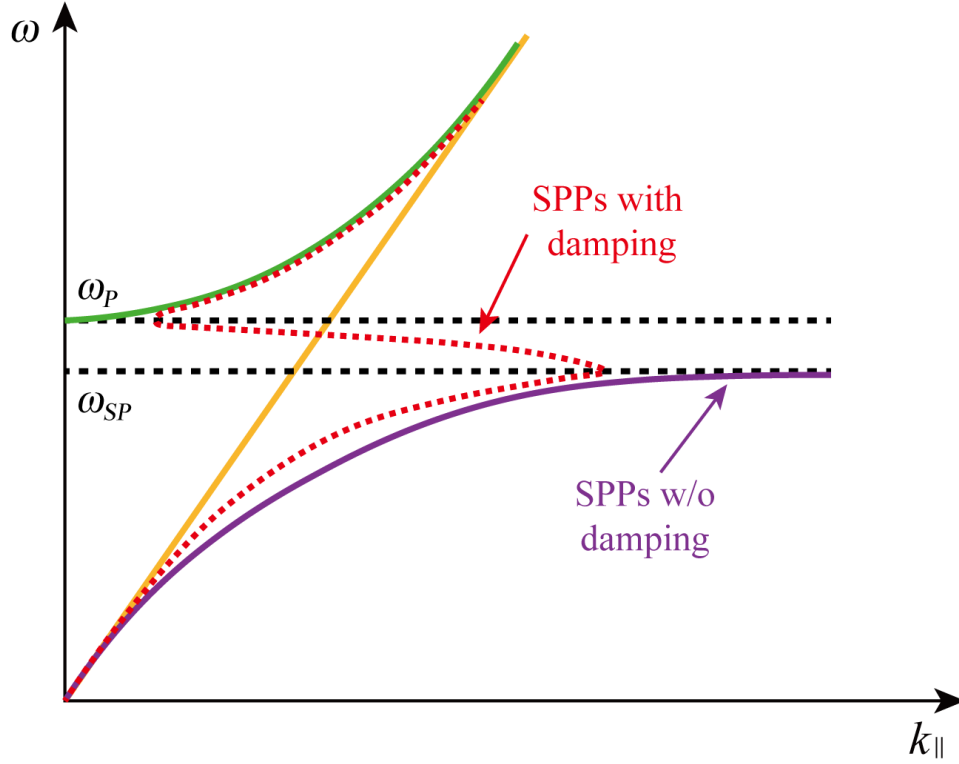
Figure 1.7: Comparison of dispersion curves of SPPs on planar interface with and without damping.

Based on the dispersion relation of SPPs, the propagation length of SPPs is expressed as [14]:

$$\delta_{SPPs} = \frac{1}{2k_{SPPs}} = \frac{2\pi}{\lambda}\left(\frac{\varepsilon_{mr} + \varepsilon_d}{\varepsilon_{mr}\varepsilon_d}\right)^{\frac{3}{2}}\frac{\varepsilon_{mr}^2}{\varepsilon_{mi}} \tag{1.13}$$

where ε_{mr} and ε_{mi} are the real and imaginary parts of the dielectric function of the metal, respectively, that is, $\varepsilon_m = \varepsilon_{mr} + i\varepsilon_{mi}$, where δ_{SPPs} is the propagation length. The propagation length depends on the incident wavelength and dielectric constant of the metal based on Equation (1.13). The propagation length can be much larger than the wavelength. For a metal such as aluminum, the propagating length is 2 μm at a wavelength of 500 nm. For metals with low losses such as silver and gold, they own a comparable propagation length when then wavelength larger than 600 nm. For a shorter incident wavelength in the visible, the propagation length is between 10 to 100 μm, and for a longer wavelength in the near infrared ($\lambda = 1.55$ μm) the propagation length is larger than 0.3 μm.

In conclusion, we have studied the definition and character of the SPPs on metal/dielectric interfaces and distinguished the SPPs according to the dispersion curves of plasmon-polaritons for an ideal metal/dielectric combination. Also, from the equitation (1.13) we know the propagation length of SPPs is inversely proportional to the frequency of incident light and has close relation with the dielectric constant of the surrounding dielectrics. According to the needs of different applications, one can select suitable metal materials, dielectric environment and excitation wavelengths for achieving different goals.

1.2.3 Excitation of SPPs

As analyzed above, the wavelength of SPPs is shorter than the wavelength of incident light. In other words, SPPs of a given frequency own a larger wavevector than the incident light, so their wavevectors do not match each other. To excite SPPs on the metal surface, the SPPs at that same frequency need to match the wavevector of incident light, thus, some means of wavevector compensation are required. A commonly adopted way to compensate the wavevector is to use a prism to achieve total internal reflection (TIR). By using the prism coupling methods, there are two different geometries that can excite the SPPs which are the Kretschmann and the Otto configurations, as depicted in Figure 1.8. The most frequently used configuration is the Kretschmann method [44]. As shown in Figure 1.8a displaying the Kretschmann system, a thin metal film is deposited on top of the prism. As the incident light impinges on the prism with an angle theta (θ) greater than the critical angle of total internal reflection (TIR), a parallel component of wavevector along the surface direction is generated, which can be written as:

$$k_{//} = \sqrt{\varepsilon_{d2}} \frac{\omega}{c} \sin \theta \qquad (1.14)$$

From Equation (1.14), since the refractive index in the prism is larger than in air ($\varepsilon_{d2} > 1(\varepsilon_{d1})$), this leads to the increase of wavevector of incident light. The wavevector $k_{//}$ can be tuned by adjusting the incidence angle of the light. To meet the requirement of wavevector matching, an adequate angle should be chosen in order to make $k_{//}$ equal to k_{SPPs}, allowing the evanescent wave to penetrate into the metal film and coupling with the free electrons, leading

to the collective oscillation of free electrons on the metal surface and establishing the excitation and transport of SPPs. However, one-layer Kretschmann system also has a limitation due to the thickness of the metal film. This configuration is suitable to excite SPPs when the film is thin, but when the metal film thickness increases, the efficiency of the SPPs excitation decreases as the tunnelling distance increases. SPPs cannot be excited through this geometry as the SPPs on the surfaces is greater than the photon wavevector in the prism at all angles. Figure 1.8b shows a two-layer system (a dielectric film with smaller refractive index than the prism is inserted between prism and metal film). By using this structure, electromagnetic radiation tunneling through the deposited dielectric film can excite SPPs at the interface between metal and dielectric under different angles of incidence. In this improved geometry, when the metal film becomes too thick, the Kretschmann system is again ineffective for excitation of SPPs. Otto system can solve this issue by putting a prism close to the metal film (Figure 1.8c). When the light is incident into the structure, it will lead to a total reflection at the bottom of prism and as the wavevector component parallel to the interface matches that of SPPs, then SPPs are excited. Due to the thin air gap between the metal film and prism in Otto system, thickness limitation of metal film is effectively cancelled to achieve the excitation of SPPs.
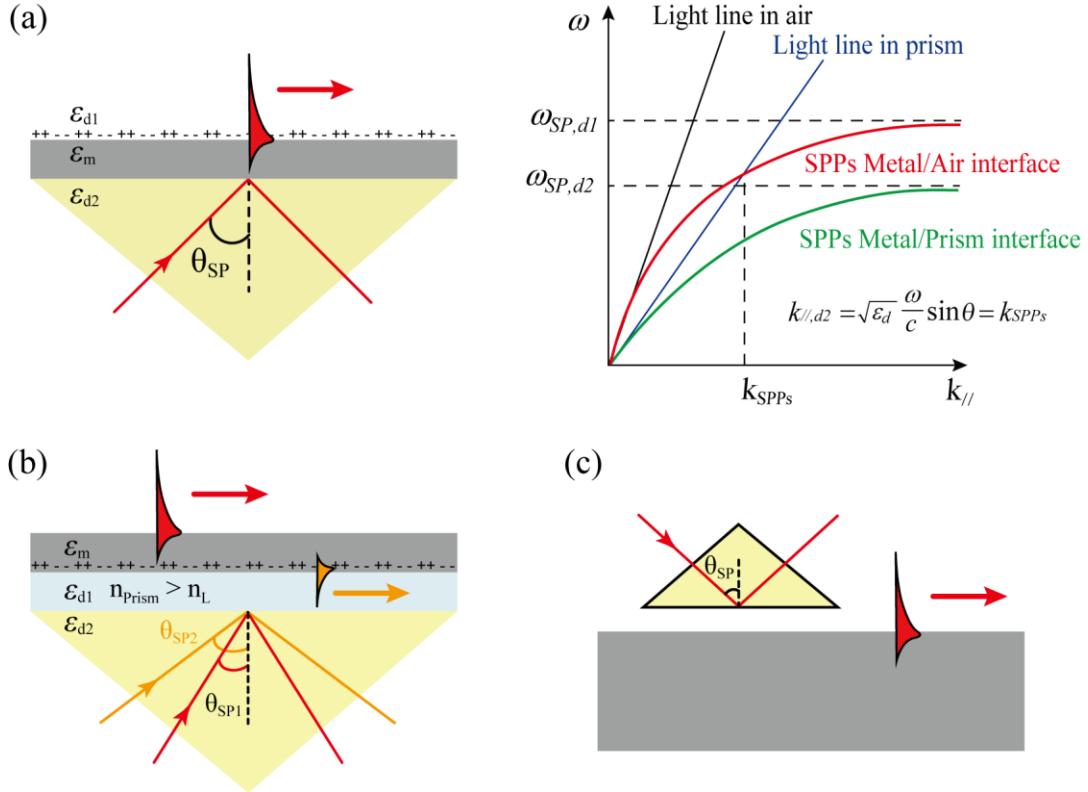
Figure 1.8: SPPs excitation configurations in prism. (a) Kretschmann system (left), corresponding dispersion relation of SPPs and light in dielectric and prism (right). (b) Two-layer Kretschmann system. (c) Otto system [45].

There are also other ways to excite the SPPs. For instance, a tapered metallic probe with size much smaller than the excitation wavelength [32] is placed above the metal surface, which causes the diffraction of the light, increasing the wavevector of incident light to match with wavevector of SPPs (Figure 1.9a). It is well known that a probe acting as light source can move arbitrarily along the direction of metal surface, so the excitation of SPPs can be achieved at any position. As shown in Figure 1.9b, another method is adopting a grating coupling scheme by using metallic grating to impart a wavevector to the incident light to excite SPPs. Microscale to nanoscale technology is used to etch metallic gratings with a periodic pitch. When light falls onto the grating, a certain evanescent diffraction order matches the wavevector of SPPs, which is then excited. As shown in Figure 1.9c, when a scattered near field scattering is generated by putting subwavelength metal particles on top of a smooth metal surface or on a rough metal surface, the SPPs excitation can be realized

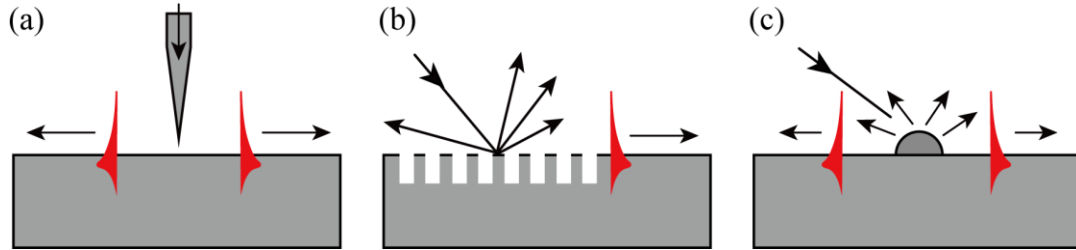without particular arrangements due to the architecture that can easily achieve the wavevector compensation.

Figure 1.9: (a) Highly focused beam excitation. (b) Grating coupling excitation (c) Near-field scattering excitation [45].

1.3 Plasmon-induced hot electrons

This topic will be developed in four parts as follows. First, the introduction and mechanism of the plasmon-induced hot electrons generation. Second, the review of main structures for generation of hot electrons and their multiple applications. Third, the fabrication techniques used for hot electron devices. Finally, examples of devices based on plasmon-induced hot electrons.

1.3.1 Hot electron generation

Electrons with high energy above the Fermi level which are in non-thermal equilibrium with the lattice are referred to as hot electrons. When highly energetic photons are absorbed into a metallic material, hot electrons are generated and emitted from the material via photoelectric effect [46]. A significant progress in this field has been recently stimulated by advances in hot electron generation in plasmonic structures. Surface plasmons generated in a plasmonic structure enable to enhance the light matter interaction through coherent oscillations of the electrons and lead to strong electromagnetic fields on the surface of the metal. Surface plasmons decay readily in a very short femtosecond time scale, either radiatively into re-emitted photons or non-radiatively through intraband or interband excitations, forming energetic hot electron (Figure 1.10). In general, we call this process

Landau damping, it brings about the hot electron generation with an effective temperature higher than that of the lattice and energy induced by the plasmonic resonance. Thus, the generation efficiency of hot electrons is determined by the ratio of non-radiative to radiative processes. For efficient hot electron generation, the re-radiation needs to be suppressed.
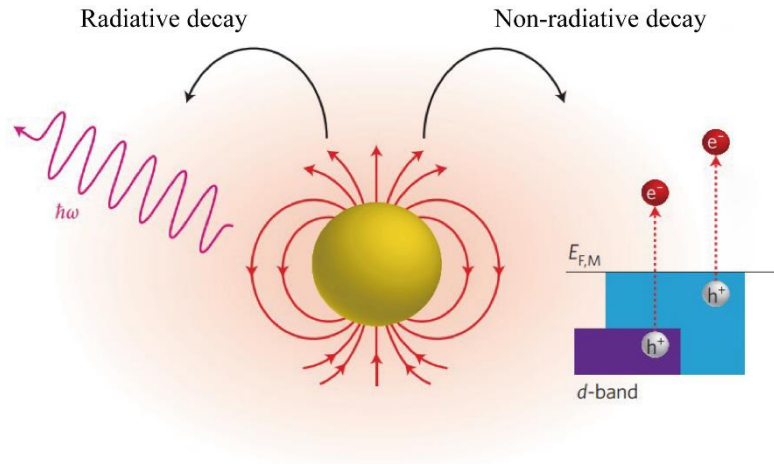
Figure 1.10: Surface palsmon decay and hot electron generation. Localized surface plasmons can decay via reemitted photons or non-radiatively via excitation of hot electrons. (In noble-metal nanostructures, non-radiative decay can occur through intraband excitations within the conduction band or through interband excitations resulting from transitions between other bands (for example, d bands) and the conduction band) [47].

The photoexcitation of localized surface plasmons redirects the flow of light (pointing vector) towards into metallic nanoparticle (Figure 1.11a). Then, Landau damping usually take place in 1~100 fs timescale (Figure 1.11b). During this short time interval, the hot carrier distribution is highly athermal. The plasmon-induced hot electrons have higher energy than the Fermi level while the hot holes with energy below Fermi level. On a timescale ranging from 100 fs to 1 ps, the hot carriers will redistribute energy by electron-electron scattering process (Figure 1.11c). At last, heat is transferred to surroundings of the metallic structure through thermal conduction, this process usually takes place in 100 ps to 10 ns, as shown in Figure 1.11d, the detailed time depends on the metallic material, size and heat transfer properties of the environment [48].

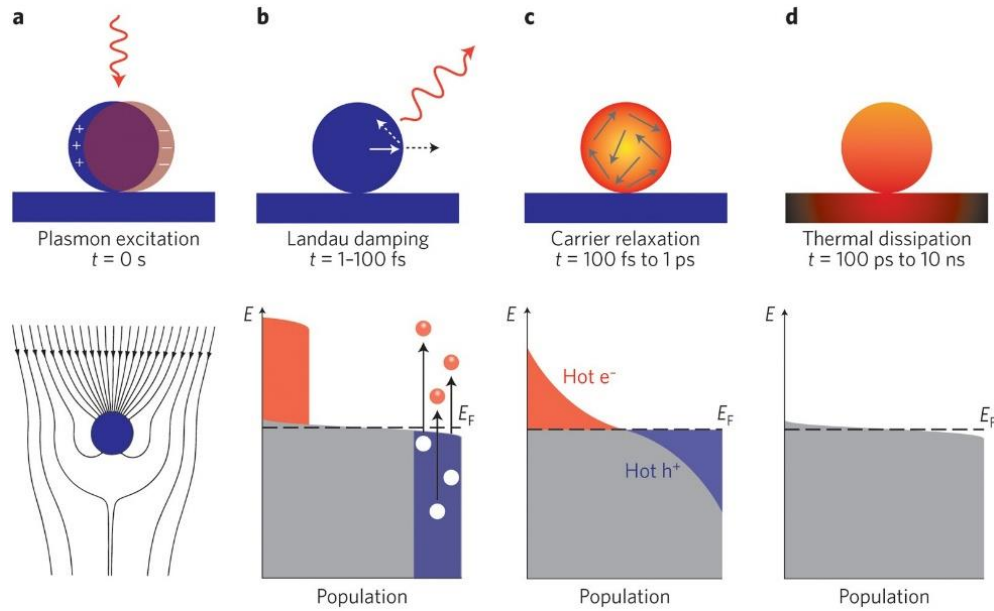**Figure 1.11:** Photoexcitation and relaxation of metallic nanoparticle. (a) Distribution of electromagnetic field under excitation of localized surface plasmon resonance. (b-d) Sketch of the electronic states (grey) following plasmon excitation. Hot electrons are represented by the red area above the Fermi energy E_F and hot holes are represented by the blue area below the Fermi energy E_F. (b) Landau damping takes place in 1 to 100 fs, the non-thermal distribution of electron-hole pairs. (c) The hot carriers will redistribute their energy by electron-electron interaction. (d) Heat is transferred to the surroundings of metallic structure through thermal conduction [48].

1.3.2 Hot electrons transport and injection

For an isolated plasmonic structure, hot electrons will collide with other electrons and photons inside the structure after their generation, finally, this part of energy will be consumed by conversion into to Joule heat [49]. There is an effective mechanism to capture those hot electrons by forming a Schottky barrier with a suitable semiconductor. Figure 1.12 depicts a metal/semiconductor Schottky junction. When the plasmonic metal structure is in contact with the semiconductor, hot electrons with enough energy that are generated by non-radiative surface plasmon decay can get over or tunnel across the Schottky barrier at the metal/semiconductor interface. In this case, the energy of the hot electrons just needs to be higher than the Schottky barrier but it can be considerably smaller than the E_g of the

semiconductor. The process by which hot electrons from the plasmonic structure pass through the Schottky barrier and are injected into the adjacent semiconductor can be summarized into three steps as follows: (1) When light impinges and is absorbed by the plasmonic structure, hot electrons are created due to the non-radiative decay of surface plasmons. (2) Hot electrons travel to the metal/semiconductor interface before thermalization. (3) Hot electrons that overcome the Schottky barrier are injected into the conduction band of the semiconductor through internal photoemission and can be collected by an external circuit as an electric current.
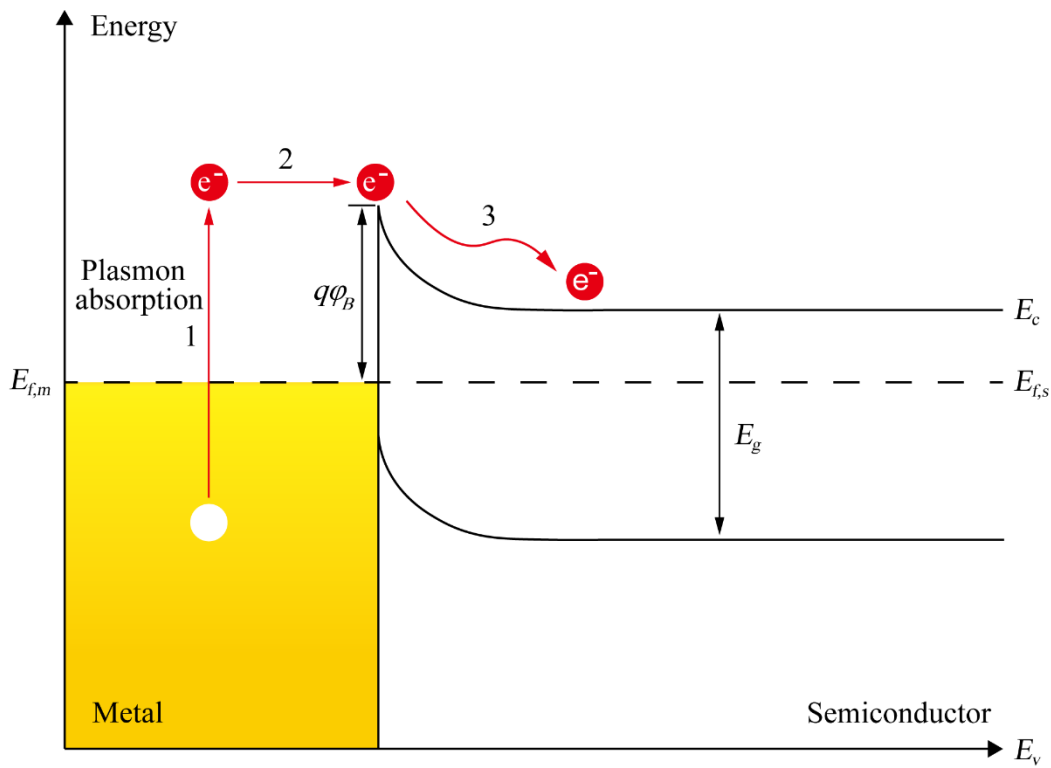
Figure 1.12: Hot-electron transport mechanism from a metal to a semiconductor in three steps: (1) Hot electrons are created due to the non-radiative decay of surface plasmon after light is absorbed on plasmonic metal structure; (2) Hot electrons transfer to the metal/semiconductor interface; (3) Hot electrons possess enough energy to overcome the Schottky barrier to cross from the metal into the conduction band of the semiconductor [46]. Here, the $E_{f,m}$ and $E_{f,s}$ represent the Fermi energy of the metal; E_v and E_c represent the valence and conduction band of semiconductor; $q\varphi_B$ represent the Schottky barrier height of the device; E_g is the bandgap of the semiconductor.

In the past few years, plasmon-induced hot electron conversion scenario has been intensely studied and distinct mechanisms have been proposed: conventional plasmon-induced hot electron transfer (PHET), which is the photoexcited plasmon decays into an electron-hole pair in metal, followed by hot electrons overcoming the barrier being transferred to the semiconductor or other material [50],[51] (Figure 1.13a). The efficiency of PHET is limited by the loss of hot electrons via ultrafast electron-electron, electron-photon scatterings and also the interfacial conservation of electron momentum [48],[52]–[54]. Comparing with conventional PHET mechanism to convert photons into electrical energy, a new pathway called plasmon-induced interfacial charge-transfer transition (PICTT) has been proposed by Wu et al. in Au-CdSe nanorods [55]. This mechanism allows the decay of a plasmon directly into an electron from the metal in a strongly coupled semiconductor acceptor (Figure 1.13b). This strategy can prevent the energy loss from the thermalization of carriers. However, the oscillator strength of charge-transfer transition is weaker than the electronic transition in semiconductors or metals [56]. There is also another effective mechanism for plasmon-induced energy conversion competing with PHET at the interface of metal/semiconductor [57] which is called plasmon-induced resonance energy transfer (PIRET). Due to the interaction between plasmon and exciton, the plasmonic energy is transferred to the semiconductor directly by generating electron–hole pairs in semiconductor (Figure 1.13c). In general, direct plasmonic coupling at metal/semiconductor interface can realize ultrafast plasmon dephasing (< 10 fs) and generate hot electrons in semiconductor to advance the plasmon hot electron transfer as studied by Tan et al. [58], for example, using an Ag nanocluster/TiO_2 system with two-photon photoemission spectroscopy. Moreover, Huang and co-workers [56] found that a strong interface coupling appears in Ag-$CsPbBr_3$ system, the PHET and PIRET process were observed with plasmon-induced electron-hole pair and charge-separated state population in $CsPbBr_3$ system, respectively, and the two processes can occur in 100 fs with a quantum efficiency up to 50% ± 18% and 15% ± 5%, respectively.
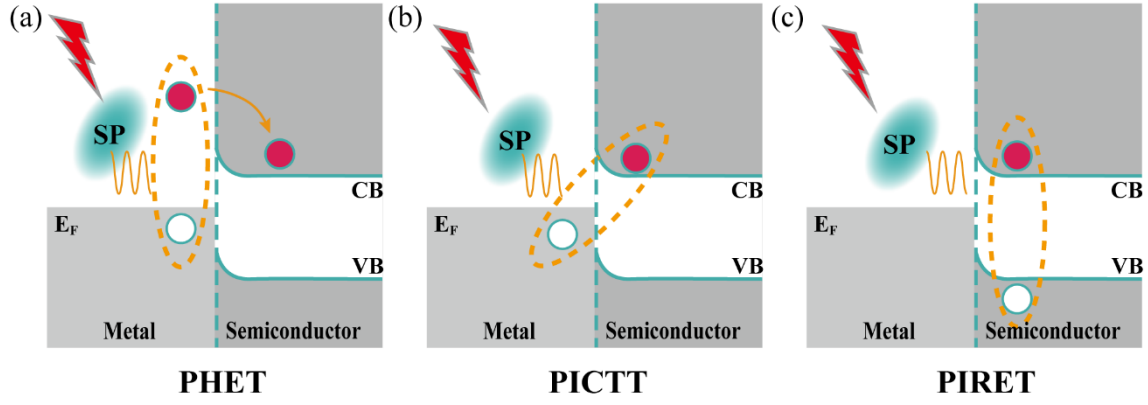
Figure 1.13: Excitation transfer processes at a metal/semiconductor interface. (a) Conventional plasmon-induced hot electron transfer process (PHET). (b) Plasmon-induced charge-transfer transition process (PICTT). (c) Plasmon-induced resonant energy transfer process (PIRET).

1.3.3 Quantification of hot electron injection efficiency

Optoelectronic material devices based on surface plasmon-induced hot electrons have complicated conversion processes such as hot electron excitation, energy relaxation, transfer, reflection at boundaries, etc. To study their mutual relation is crucial for the final performance of the device. Therefore, how to go from a qualitative description of dynamic processes of carriers to the quantification of each process (carrier injection efficiency), in order to further guide the improvement of the performance of hot carrier devices, is a challenging issue nowadays. At the same time, responsivity of the device is also of crucial importance to validate the performance of the plasmon-induced hot electron device. The photoresponsivity *R(ω)* can be calculated as:

$$R(\omega) = A(v)\eta_1(v)\eta_2(v) \tag{1.15}$$

Where, $A(v)$ is the optical absorptivity of the device, which can be determined by measuring the total absorption spectrum of the device, $\eta_1(v)$ is the probability of hot electron transfer through the Schottky interface, depending on the spatial distribution and mean free path (*MFP*) of the hot electrons, and $\eta_2(v)$ is the probability of hot electron emission over the Schottky interface. $\eta_1(v)$ and $\eta_2(v)$ both influence the internal quantum efficiency of the

device. Internal and external quantum efficiency (η_1, η_2) jointly determine the photoelectric conversion efficiency. The total absorption distribution in metal/semiconductor device is calculated numerically using the local ohmic loss, given by [20],[59]:

$$Q(r, \omega) = \frac{1}{2} \varepsilon_i \omega \left| \vec{E}\,(r, \omega) \right|^2 \tag{1.16}$$

where, ε_i is the imaginary part of permittivity function of the absorber; ω is the angular frequency of incident light; $\vec{E}\,(r, \omega)$ is the local electric field at position r, which can be obtained from numerical simulations. This determines the wavelength dependent absorptivity A. Due to the thermal energy loss of hot electrons in the transport step, the probability $\eta_1(v)$ of an electron to reach the M/S interface can be calculated on the basis of the assumption of an isotropic initial momentum distribution and adopting the exponential decay model, which can be denoted as [21],[59]:

$$\eta_1(v) = \frac{1}{2\pi} \int_{\theta_1}^{\theta_2} exp\left[-\frac{d(Z)}{\lambda_e |cos(\theta)|} \right] d\theta \tag{1.17}$$

where, d is the vertical distance of hot electrons generation position to the M/S interface; λ_e is the energy dependent mean free path of the electrons accounting for electron–electron and electron–phonon contributions, and θ is the electron diffusion angle. Therefore, the probability $\eta_1(v)$ of hot electron transport to the Schottky interface depends on the spatial distribution and mean free path of the hot electrons [60]. The photoemission probability $\eta_2(v)$ of hot electrons across the Schottky interface can be approximated using the modified Fowler theory [61]:

$$\eta_2(v) \approx C_F \frac{(hv - q\varphi_B)^2}{hv} \tag{1.18}$$

where, C_F is the device-specific Fowler emission coefficient; hv is the energy of incident photons; $q\varphi_B$ is the Schottky barrier height of the device, which can be extracted from the current-voltage characteristics of the devices.

1.3.4 Hot electron harvesting architecture

A striking result reported by Zhao et al. [62] was that by using TiO_2 films supporting gold or silver particles it was possible to achieve a photocurrent generated on the anode with illumination in the visible wavelength range. This was an inspiring breakthrough because TiO_2 is a wide bandgap (3.2 eV) semiconductor material, hence generating photocurrents on a TiO_2 electrode needs ultraviolet illumination. Zhao et al. explained the possible mechanism is the LSPR in the metallic nanoparticles. After that, multiple researches witnessed photocurrent generation in close-circuit, which can be classified into three steps: hot electron generation, injection and regeneration. This system includes metallic Au and Ag nanoparticles decorating porous TiO_2 (Figure 1.14a left). Tian et al. also observed hot electron injection on TiO_2 by the excitation of LSPR on the gold nanoparticles with illumination in the visible wavelength range [63]. Saji et al. adopted a $SiO_2@TiO_2$ shell covering Au nanoparticle cores for the catalysis of methylene blue. In this architecture, the photocatalysis is due to the plasmon–induced hot electron transfer from gold to the $SiO_2@TiO_2$ thus enhancing the degradation reaction [64]. In these architectures, with light illumination, hot electron transfer from the plasmonic nanoparticle to the semiconductor can lead to the oxidation and reduction reaction carried out on the hole-rich and electron rich electrode. Afterward, compensatory electrons coming from donor sacrificial solution mixing with metallic nanoparticles were injected to the nanoparticles in order to balance the electrons delivered by the plasmonic nanoparticles (Figure 1.14a right). Chen et al. also used the same mechanism that comprising ZnO nanorod arrays with gold nanoparticles for Schottky barrier photovoltaic cells. In this architecture, photoexcited electrons are transported from the gold nanoparticles to the ZnO conduction band, leaving positively charged holes in the gold nanoparticles. The electrolyte solution provides electrons to gold nanoparticle to balance the depleted electrons in gold. Due to the Schottky barrier, the recombination of carrier can be effectively suppressed [65]. The classic and frequently used architecture to get plasmonic hot electrons is the metal-semiconductor Schottky junction (Figure 1.14b). In this system, electrons with enough kinetic energy reaching the metal/semiconductor interface can go across the Schottky barrier and then being injected into the
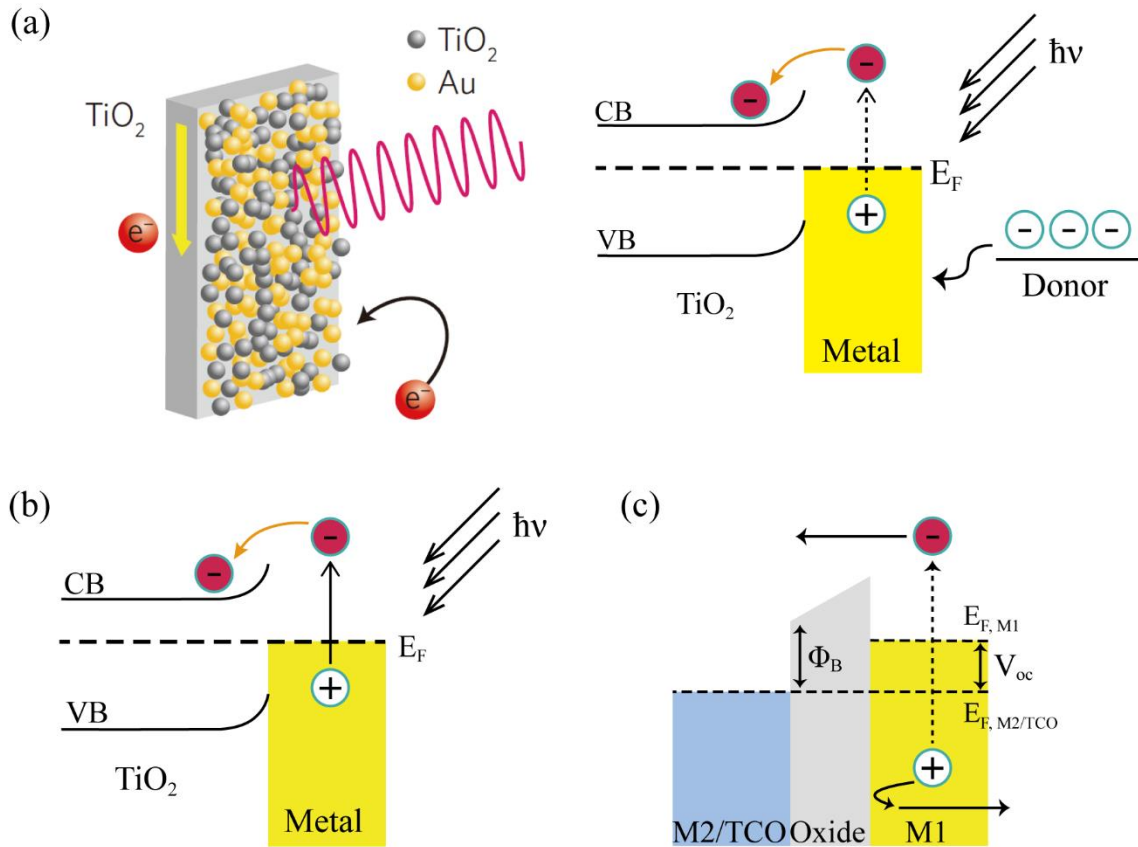
Figure 1.14: Hot electron harvesting architecture. (a) Sketch of the frame proposed by Zhao [62] et al. consisting a nanoporous TiO_2 decorated with Au nanoparticles (left); In this photocatalytic system, energetic electrons from metal are injected to TiO_2 with the donor electrolyte solution compensating the positive holes (right). (b) A metal-semiconductor Schottky diode, electrons are injected to the semiconductor (Silicon, TiO_2 or ZnO) with light irradiation. (c) A metal-insulator-metal (MIM) system that can produce net photocurrent provided the injection between electrode is not balanced.

adjacent semiconductor and collected by external electrode in form of photocurrent [10],[66],[67]. Li et al. reported a metamaterial based on metal (Au)-semiconductor (n-Si) Schottky diode system achieving great enhancement for photodetection [20]. There is also another scheme to collect hot electrons which uses a metal-insulator-metal (MIM) junction (Figure 1.14c). This structure comprises two metallic layers with an insulator layer in between. When operated at low frequencies such as Thz or mid-IR, photoexcited carriers cannot cross the barrier (∼1 eV), typically present in MIM structure for photodetection. Electron injection appears when a bias is applied or the oxide is sufficiently thin [21].

However, due to existence of insulating layer, this MIM structure still remains being of low experimental efficiency.

1.3.5 Figure of merit

In this section the main figures of merit of hot electrons based optoelectronic devices for photodetection and photovoltaic effect are briefly introduced.

1.3.5.1 Photodetection

Photodetectors can be broadly defined as electronic devices that convert an input light signal into an output electrical signal. One of the key parameters to evaluate a photodetector is the responsivity (R). The responsivity is the ratio of output photocurrent to the input light power of the optoelectronic device, which reflects the ability of photoelectric conversion of the photodetector under illumination at different wavelengths, also called spectral sensitivity. The unit of responsivity is denoted as ampere per watt (A/W) in the SI unit system. The external quantum efficiency (*EQE*) also can be used to express the ability of response of devices, which is defined as the ratio of converted electrons to incident photons. For quantification, the value is in the range between 1 to 100%. Additionally, the internal quantum efficiency (*IQE*) equals the ratio of converted electrons to absorbed photons. Generally, for a given device the *IQE* is higher than the *EQE* because the factor 1-R is always less than 1. Dark current (I_d) is another relevant parameter of photoelectric devices, which needs to be minimized to scale-down the consumption of energy and it refers to the small current that flows through the photosensitive devices in the absence of incident photons. In photodetectors, dark current is a background current that can worsen the linearity of the device. Generally, the dark current of a device has correlation with the outside temperature and the applied bias during the test. The ratio of photocurrent to dark current is adopted to evaluate the device performance; only when the ratio is larger than 1, the optical signal is detected. In practical application, we need to have a strong signal current and small dark current. For a given photocurrent, the smaller the dark current, the higher signal-to-noise ratio, and more powerful detectability of weak light signals. Noise equivalent power (*NEP*)

is a measure of sensitivity of detectors, and it is defined as the minimum optical power required for an output signal-to-noise ratio (*SNR*) of 1. A more sensitive detector corresponds to a smaller *NEP*. Normalized detectivity (*D**) is also used to characterize the sensitivity of the device, describing the extreme detection capability for weak signals. The different figures of merit of a photodetector are summarized in Table 1.1.

Table 1.1: Figure of merit of photodetector

Name	Expression	Unit	Definition
Responsivity (*R*)	$I_{ph}/P_{in} = EQE \cdot e/h\nu$	A/W	Photocurrent per incident power
External Quantum Efficiency (*EQE*)	$Rhc/e\lambda$	-	Electron ratio to incoming photon rate
Internal Quantum Efficiency (*IQE*)	$EQE/a(\lambda)$	-	Electron ration to the absorbed photons $a(\lambda)$
Dark current (*I$_d$*)	-	A	Current without irradiation
Δ	I_{photo}/I_d	-	Ratio of photocurrent to dark current
NEP	S_n/R	$W/\sqrt{Hz}$	Noise equivalent power. S_n is the noise spectral power density
D*	$\sqrt{A \cdot \Delta f}/NEP$	Jones (cm·$\sqrt{Hz}$/W)	Normalized detectivity. *A* is the area of detector. *Δf* is the measured width

1.3.5.2 Photovoltaic

Solar cell, also called photovoltaic cell, is designed to directly convert sunlight into electrical power through the photovoltaic effect. (Figure 1.15). The short circuit current (I_{sc}) is the current that flows through the solar cell when the voltage is zero across the solar cell. The open circuit voltage (V_{oc}) is the maximum voltage in a solar cell and this corresponds to zero current. Fill factor (*FF*) is essentially a measure of efficiency of a solar cell and it is defined

as the ratio of maximum power obtained to the product of short circuit current I_{sc} and open circuit voltage V_{oc}. The power conversion efficiency (*PCE*) of solar cells refers to the ratio of the maximum output power to the power of incident light, which directly reflects the performance of solar cells. The briefly summarized figures of merit of the photovoltaics are shown in Table 1.2.

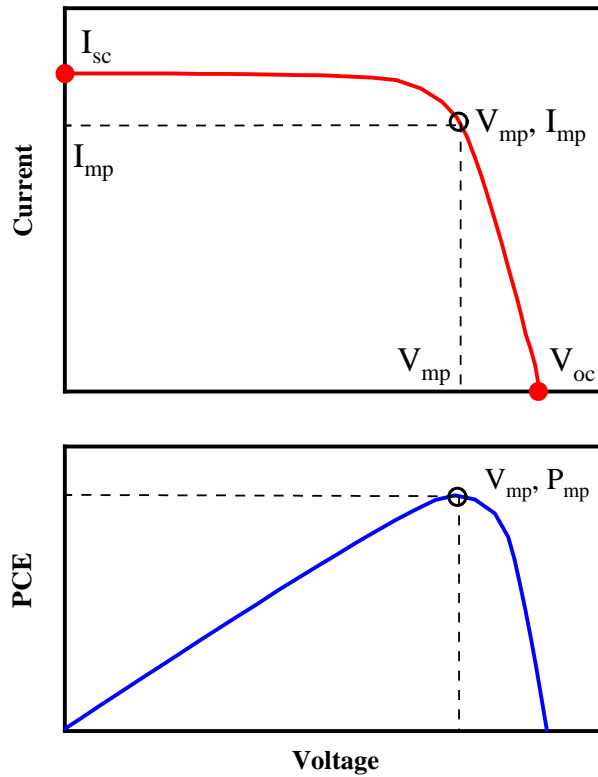
Figure 1.15: Graph of solar cell output current (top) and power (bottom) as a function of voltage. The short-circuit current (I_{sc}) and open-circuit voltage (V_{OC}) as well as the maximum power point (V_{mp}, I_{mp}) are indicated.

Table 1.2: Figures of merit of photovoltaic

Name	Expression	Unit	Definition
Short circuit current (I_{sc})	-	A	-
Open circuit voltage (V_{oc})	-	V	-
I_{mp}	-	A	Current at maximum power point
V_{mp}	-	V	Voltage at maximum power point
Fill factor (*FF*)	$\dfrac{I_{mp}V_{mp}}{I_{sc}V_{oc}}$	-	Ratio of maximum power to I_{sc} and V_{oc}
PCE	$\dfrac{FFI_{SC}J_{SC}}{P_{In}}$	-	Power conversion efficiency

1.3.6 Challenges in hot-electron optoelectronic

On the groundwork of reported hot-electron based photocurrent generation devices, the purpose of this thesis is to tackle the following challenges:

● Plasmonic Schottky diode system: hot-electron based photocurrent generation in plasmonic Schottky diode devices usually adopts a combined plasmonic-metal/semiconductor architecture. In this thesis, we designed and fabricated metal/semiconductor devices textured with periodic nanostructures for photocurrent generation. Two distinct mechanisms are contributing to photocurrent generation, namely, hot-electron injection and PIRET working simultaneously in the spectral range below and above the semiconductor bandgap for achieving a desired photocurrent performance.

● Facile fabrication scheme: hot-electron based photocurrent generation devices generally focuses on maximizing the photocurrent and its efficiency. In the literature, most of the techniques follow high cost and complicated lithography-based fabrication procedures.

In this thesis, we report a low-cost and scalable method to produce the desired architecture, which adopts soft nanoimprinting transfer techniques.

● Competitive performance: multiple efforts have been devoted to research in the area of hot-electron based photocurrent generation devises. However, their performances are still pretty low level compared with the photovoltaic devices. Therefore, we aim at improving the performance of the hot-electron based photocurrent generation devices for potential commercial use.

Chapter 2

Fabrication, characterization and simulation methods

In this chapter, I will introduce the relevant experimental and modelling techniques used in this thesis.

2.1 Deposition methods

2.1.1 Spin coating

Spin coating is one of the most used methods for preparing desired films from liquid solutions onto substrates since it is easy to handle and convenient both for research and also in industrial environments. The process starts with an amount of solution dropped at the center of a substrate, then the spin-coater substrate holder starts rotating and the solution spreads onto the whole substrate, while any excess solution is tossed out of the substrate during the process. The final thickness of the aimed film is dependent on the velocity of spinning and the viscosity of the solution material. Based on the time set during the spin coating process, it is possible to obtain films in which the solvent is totally dried or where some amount of solvent still remains in the film, in which case the film is viscous after the process. In this thesis, sometimes we need such viscous films with solvent inside after spin coating in order to apply a nanoimprinting pattern on the film: We need a semi-dried film to achieve that casting into the master mold results in the desired pattern. In this thesis, we have used a SPS POLOS 150i spin coater to deposit thin films of various resists and polymers on silicon (Si) substrates.

Operation procedure:

For the fabrication of nanoscale inverted pyramids on Si, we spin-coated the SU8 resist. First, a Ge/Si substrate was cleaned with sonication in acetone and ethanol for 2 min separately

and blown dry with N_2. Then, the substrate was baked on a hot plate at 150 ^{o}C for 5 min and let it cool down to room temperature. Subsequently, SU8 photoresist (from Microchem) was dropped on the whole surface of Ge/Si wafer and spin-coated at 2000 rpm for 10 s, a 600 nm thick SU8 film is obtained finally. The Ge/Si substrate with SU8 film was used for further thermal nanoimprinting lithography operation, which is described in chapter 2.3.2.1.

For the fabrication of microscale inverted pyramids on Si substrate, we spin-coated the Shipely 1813 photoresist. First, Ge/Si substrate was cleaned with sonication in acetone and ethanol for 2 min separately and blown dry with N_2. Then, the substrate was baked on a hot plate at 150 ^{o}C for 5 min and let it cool down to room temperature. Finally, Shipley 1813 was dropped on the surface of pre-cleaned substrate and spin-coated at 5000 rpm for 25 s and soft baked at 95 ^{o}C for 1 min. The Ge/Si substrate with Shipely 1813 film was used for further photolithography operation, which is described in chapter 2.2.1.

For the fabrication of metal/organic-semiconductor structure on conductive glass, we spin-coated the N2200 semiconductor solution on ITO glass. First, ITO glass was cleaned with sonication in acetone, isopropyl alcohol for 10 min separately, following with 2 min sonication in water, then blown dry with N_2. Then, the substrate was treated with UV/ozone (UVO) for 20 min. Finally, 8 mg/mL N2200 solution in chlorobenzene was spin-coated on as-treated ITO glass at 600 rpm for 15 s. The ITO substrate with N2200 semi-dried film was used for further solvent assisted nanoimprinting lithography process, which is described in chapter 2.3.2.3.

2.1.2 Molecular beam epitaxy

Molecular beam epitaxy (MBE) is a physical deposition method for epitaxial thin-film growth on a substrate. Molecular beams of the source materials are evaporated and deposited on the substrate in an ultra-high vacuum chamber. The typical characteristics of MBE is that growth takes place in vacuum conditions of the order 10^{-10} mbar or even higher vacuum level, at low deposition rates (usually less than 300 nm h^{-1}) in order to allow the films to grow epitaxially. During the deposition process, RHEED (reflection high-energy electron

diffraction) system may be used to monitor and control the thickness and structure of the crystal layers. The use of RHEED to monitor the thickness of the crystal layer can better guarantee an epitaxial growth, and this system is fundamental in manufacturing of semiconductor devices [68] and essential for the development of nanotechnologies. In this work, MBE method is adopted to deposit both undoped silicon and germanium on the n-type silicon substrate, the latter with suitable thickness to act as a hard mask in the etching process, details are in chapter 3.

Operation procedure:

We used the MBE method [69] in our lab to prepare the Ge/Si wafer. Si and Ge layers were deposited on double-sided polished, n-type (5 Ω.cm) Si wafers. After oxide desorption at 850 °C, a Si layer was grown at 660 °C to obtain an ideal Si surface. Then temperature was decreased to 400 °C and a 30 nm layer of Si was deposited. This low temperature Si (LT-Si) layer has a compliant effect that helps to relax the strain in the subsequently deposited Ge [70]. The temperature was further reduced to 200 °C and a 10 nm layer of Ge was grown. The low temperature prevented Ge atoms from moving on the surface, hindering the Stranski-Krastanow growth mode and kept a flat growth front. While growing the next 20 nm of Ge, the substrate temperature was increased slowly until it reached 400 °C. This growth sequence produced a network of misfit dislocations that prevented build-up of compressive strain in the Ge layer due to the smaller lattice parameter of Si. The dislocations appear mostly within the two low temperature Si and Ge thin sections. In particular, a high density of point defects in the Ge grown at low temperature contributes to effectively relax the mismatch strain and to act as getter sites that reduce the threading dislocation density [71]. The next step consisted of deposition of a 400-nm thick layer of Ge at 500 °C. This layer had little residual compressive strain. Finally, a Si cap layer was deposited on top to protect the Ge surface. This structure was subsequently annealed at 700 °C for 30 min in the same growth chamber. This annealing temperature is sufficient to reduce further the threading dislocation density [72] to a measured value of 1×10^7 cm^{-2}. At the same time, since Ge has a thermal expansion coefficient more than two times larger than Si, a compressive strain develops in the Ge layer when temperature is raised up to 700 °C. The high temperature annealing allows gliding of

the remaining threading dislocations and the 400 nm thick Ge layer becomes nearly strain free again while kept at high temperature. Finally, during a fast-cooling process of the wafer down to room temperature, the Si wafer contracts less than the Ge layer, resulting in a final tensile biaxial strain in the Ge. The highest biaxial tensile strain attainable by this growth procedure is in the range of 0.1 to 0.2%.

2.1.3 Thermal evaporation

Thermal evaporation is a prevalent physical vapor deposition method due to its simplicity. Similar to the above introduced MBE technique, during the thermal evaporation process, a target source material is heated to its evaporation point by joule heating of a boat in high vacuum condition (level of 10^{-6} mbar). The vaporized molecules of source material travel towards the surface of substrate where they nucleate and coalesce together, forming a film of target material. A broad variety of materials can be evaporated through this method such as gold, silver, aluminum, nickel, chrome and molybdenum trioxide, among others. In this thesis, this technique is frequently used for the deposition of metal films either as plasmonic metal layer or the backside electrode.

Operation procedure:

The materials gold and molybdenum trioxide (MoO_3) were evaporated to form the appropriate structures needed in this thesis. In both cases, the vacuum pressures in the evaporation chamber ranged from 1×10^{-6} mbar to 3×10^{-7} mbar, and the deposition rates were stabilized at around 6×10^{-2} nm s^{-1} for gold and 5×10^{-2} nm s^{-1} for MoO_3.

2.2 Photolithography

Photolithography, also called "Optical lithography" or "UV lithography", is a patterning method that uses UV (348~440 nm) light-radiation to expose designed shapes or patterns on a photosensitive polymer known as photoresist. There are two kinds of photoresists, positive and negative (Figure 2.1). In a positive photoresist, when exposed to the light, fragmentation

of the molecular chain appears and the irradiated area becomes soluble to the developer. Hence, after the photoresist layer coated on the substrate to be patterned has been exposed to UV light, every illuminated part of the photoresist will be chemically removed. A negative photoresist shows an exact opposite response, all the portions of photoresist exposed to UV light trigger a crosslinking reaction, thus these regions are insoluble to the developer, the rest unexposed photoresist is removed during the developing process. In this case, the resulting pattern will be the reverse of the photomask. So, as a standard method, photolithography is widely used in the printed circuit board (PCB) and microprocessor fabrication and microelectromechanical systems with extremely high precision of small-size patterns over an entire wafer.
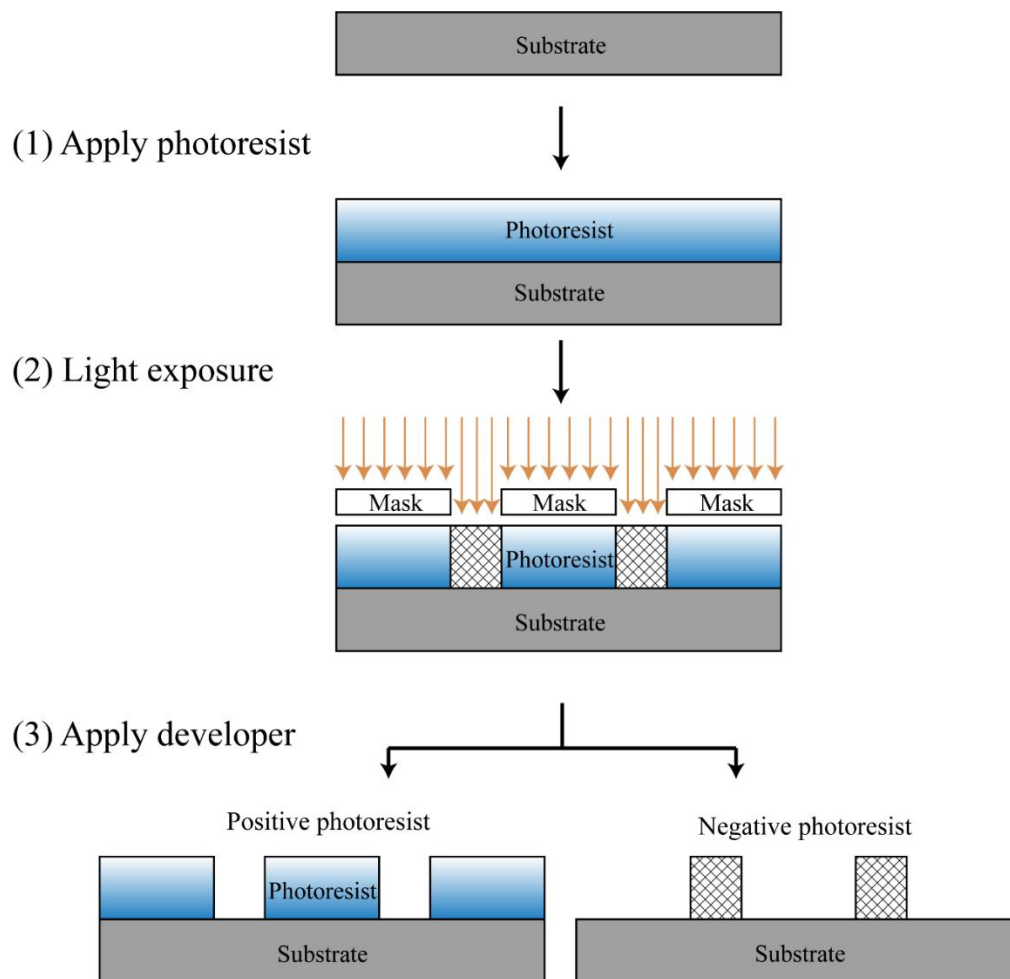

Figure 2.1: Diagram of basic photolithography process displaying both positive and negative photoresist behavior.

Operation procedure:

In this thesis, photolithography technique is used to prepare arrays of holes with diameter of few microns on photoresist for the fabrication of microscale inverted pyramid arrays on silicon substrates through anisotropic wet etching. First, the Ge/Si substrate is cleaned with sonication in acetone and ethanol for 2 min separately and blown dry with N_2. Second, the substrate is baked on a hot plate at 150 ^{o}C for 5 min and let it cool down to room temperature. Third, the positive photoresist Shipley 1813 is spin coated on the pre-cleaned substrate at 5000 rpm for 25 s and soft baked at 95 ^{o}C for 1 min. Fourth, a pattern of holes with the desired diameter and pitch is printed on the resist with a micro-writer (Micro-Writer ML3 from Durham Magneto Optics) under exposition with a 385 nm UV light source. Finally, the wafer is developed for 45 s, rinsed with water, and blown dry with N_2. After this step, the wet etching step to get micro-size inverted pyramid arrays on silicon substrate can be performed, as it is introduced in following section.

2.3 Nanoimprint lithography (NIL)

2.3.1 Introduction to NIL

Nanoimprinting lithography is an emerging technique attracting plenty of interest in the next-generation of lithography methods, basing on the idea of direct replication; First, the resist is coated on the substrate; then a master stamp with a high-resolution pattern is placed on the resist with applied pressure; finally, the patterned resist film covered substrate is stabilized with UV curing or thermal baking and the desired device is obtained. NIL is an attractive technique because of its high resolution, low cost and mass production process characteristic. NIL is not limited by diffraction like optical lithography and it allows features of transferred patterns at submicron scales down to 5 nm with properly designed molds, as reported before [73], similar to more complex and high cost nanofabrication techniques. The master fabrication is critical in the development of cost-effective and high-throughput NIL process. Simple process with high throughput and low cost of NIL fulfills the possibility of minimizing the cost compared with other lithography methods that highly depend on

complex guided electron beam and optical setups. Moreover, the same mold can be recycled many times. These two merits make NIL an attractive method for industrial applications due to the large-area imprint and high throughput. Moreover, NIL is a versatile approach in a sense that a series of materials can be imprinted [74]. Those materials do not need to be radiation sensitive or possess concrete composition or being nanoscale flat on the surface. For the work we have done in this thesis, in general, the process requires a resist that is viscous at a certain time; after the resist is patterned and solidified, the aimed feature is obtained. This approach can transfer the desired pattern directly on the film where we want without any disruption of the fabrication scheme. In many cases, this method can avoid the addition of extra photoresist layers or the need to transfer the patterns by using etching methods. Therefore, these merits have brought the NIL work in the fields such as solar cell [75], metamaterials [76], etc.

Since the imprint lithography idea has been proposed, numerous variations basing on this technique have been developed. The commonly used variations of NIL are differentiated from each other by the fabrication process: T-NIL denotes thermal patterning with pressure, UV-NIL involves UV light curing and S-NIL entails solvent assistance.

2.3.2 Nanoimprinting methods

2.3.2.1 Thermal nanoimprinting lithography (T-NIL)

Thermal nanoimprinting lithography is one of the major approaches in NIL technique. In T-NIL, the patterned materials (*e.g.,* thermoplastic polymer) must be deformable with external pressure. Generally, the elastic modulus of the resist should be lower than the NIL mold during the pressuring process and the resist must have appropriate reflow behavior in order to keep the fidelity of the nano/microstructure. The T-NIL process is implemented at the temperature above the resist glass transition temperature T_g to enhance the fluidity compared with the resist at ambient conditions. Then, the heated resist may stream and fill the cavities of the master mold with a certain pressure. Finally, the master mold is peeled off from the resist when the resist cools down at a temperature below its T_g, so the negative pattern is left

on the resist (Figure 2.2a, b). Here, an adequate lift-off speed of the template from the resist is crucial for obtaining a high-quality feature on the resist. Figure 2.2c shows a SiO_2 pillars array with 10 nm in diameter, which acts as a robust imprint mold to be used in the T-NIL process. As mentioned, T-NIL is a versatile approach that can pattern unconventional materials over large areas. Figure 2.2d shows a wafer-size TOPAS plastic film with features fabricated by using hard silicon with patterns as mold and T-NIL technique.
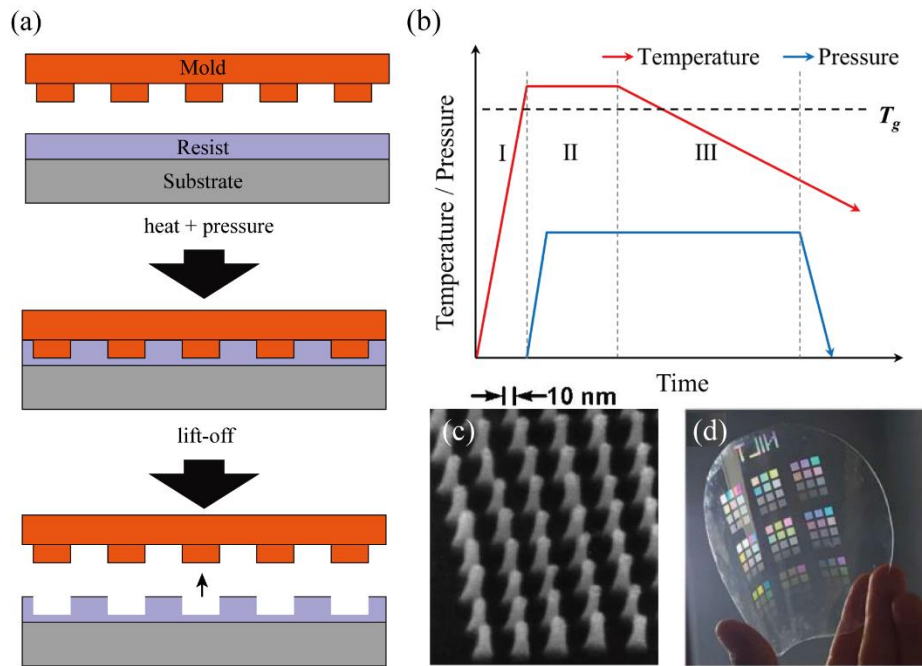
Figure 2.2: Sketch of thermal nanoimprinting process and example of features formed via T-NIL. (a) Sketch of the T-NIL process on resist. (b) Sequence of heat and pressure during thermal nanoimprinting [77]. (c) Mold with 10 nm diameter SiO_2 pillars array [78]. (d) Wafer scale patterned TOPAS film.

Operation procedure:

In this thesis, a soft T-NIL technique was used to imprint arrays of cylindrical holes with diameters of few hundred nanometers on a resist used for the fabrication of nanoscale inverted pyramid arrays on Ge/Si substrates through anisotropic wet etching. First, the pre-cleaned Ge/Si substrate was put in the ozone cleaner for 20 min to improve the hydrophilic character of its surface. Second, on top of the Ge layer, a 600 nm thick SU8 photoresist layer

was spin coated at 2000 rpm for 10 s. Subsequently, different stamps of polydimethylsiloxane (PDMS) were used to imprint square arrays of holes onto the SU8 photoresist. The PDMS mold consisted in arrays of pillars with a diameter of 300 nm and a height of 350 nm but with different lattice parameter (LP) of 400, 500 and 600 nm; the patterns covered an area of 16 mm^2. The nanoimprint step took place on a hot plate at 90 °C, immediately after the coating with the photoresist. For this purpose, the patterned PDMS mold was pressed against the substrate for 30 s and then left to cool down to below the glass transition temperature of the resist. The negative pattern of the PDMS mold was obtained on the SU8 layer by gently stripping off the master, while it continued to cool down to room temperature. The patterned SU8 layer was cured under UV light for 10 min and hard-baked at 160 °C on a hot plate for 30 min. After this step, further dry and wet etching steps were needed to get few hundred nanometer-sized inverted pyramid arrays on the silicon substrate, as will be explained in the following section.

2.3.2.2 UV nanoimprinting lithography (UV-NIL)

The UV-NIL procedure is similar to the one described for T-NIL, but in this case by making use of a photosensitive material. After imprinting, the resist is hardened by UV light exposure causing the cross-linking of polymer chains (Figure 2.3a). Therefore, it needs that the substrate or mold is transparent to those wavelengths (typically UV). Usually, a mold or substrate made of quartz, glass or transparent silicone is used in this system. Despite the UV-NIL technique being limited to light sensitive materials, it still owns advantages. First, UV-NIL can pattern the features in an extremely low pressure which is enough for the liquid resist material (low viscosity) to fill into the mold features. Moreover, the low viscosity allows the resist to spread into the mold in a short time and still keeps high resolution (Figure 2.3b). Furthermore, the particular advantage of UV-NIL over T-NIL is the room temperature treatment for those thermal sensitive materials. Figure 2.3c shows square and hexagonal photonic structure arrays with pattern sizes down to 200 nm fabricated by UV-NIL in Ormostamp on glass.
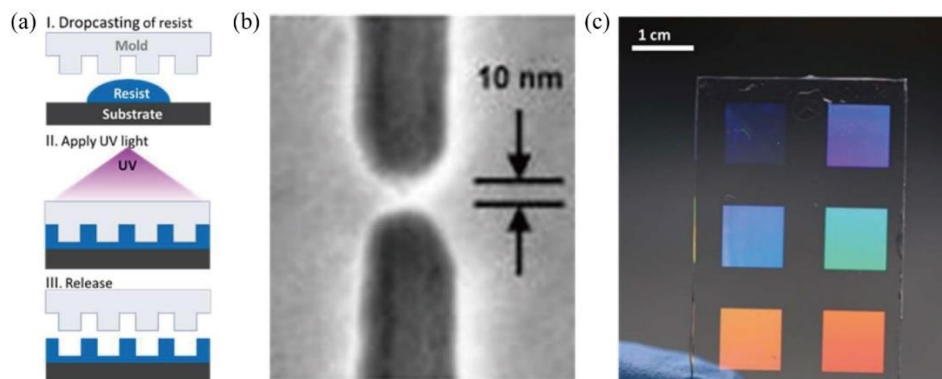
Figure 2.3: Sketch of UV-NIL process and example of features formed via this method. (a) Process steps and element involved. (b) Resolution in 10 nm features [79]. (c) Centimeter size nanometric patterns fabricated in Ormostamp on glass slide.

2.3.2.3 Solvent assisted nanoimprinting lithography (S-NIL)

The S-NIL, as the name indicates, refers to transferring the pattern with the help of solvents. The solvent in the material layer provides the needed viscosity previous to nanoimprint the mold. Before the solvent dries and the material layer is still viscous and wet, the mold is pressed onto the material layer, so the negative feature of the stamp is imposed. After the solvent evaporates (with or without heat), the patterned layer becomes solid with the required feature. Finally, the mold is stripped gently.

In the NIL fabrication, both blade coating and spin coating are frequently used to process material into a layer for the following imprint process, giving the possibility of imprinting while the layer is still humid and soft before the solvent dries totally. Besides, a drop of the proper solvent applied by drop casting to the material layer can also keep the humidification of the material. This technique is suitable for materials that are hard to imprint when dry, but become viscous and malleable to accept features when wet, for instance, some organic donor polymers and inorganic pastes.

Operation procedure:

The S-NIL technique in this thesis is applied to transfer the inverted pyramids to a n-type organic semiconductor film. First, a n-type polymer N2200 solution with concentration of 8 mg/mL in chlorobenzene is prepared and kept under stirring overnight in order to get a homogeneous liquid. Then, the as-prepared N2200 solution is spin coated onto the ITO glass substrate at 800 rpm for 20 s. Third, once the spin coating finishes, the substrate is taken out and imprinted with the fabricated hybrid PDMS stamp (with upright pyramids pattern) immediately to avoid the evaporation of solvent. During the imprint process, a heavy weight is placed onto the PDMS stamp in order to ensure that the PDMS stamp is fully in contact with the polymer layer. At last, once the solvent evaporates, the PDMS stamp is gently peeled off from the polymer N2200 layer which keeps the patterned features on top.

2.3.3 Nanoimprinting molds

2.3.3.1 Hard mold

Comparing with soft nanoimprint lithography that works with soft and flexible molds, "hard" nanoimprint lithography uses nanofabricated molds made of rigid materials that have a sufficient Young modulus like silicon, silicon dioxide or polymeric materials [80]. Because of the stiffness of their relief features, rigid molds can replicate patterns whose resolution have, in principle, no fundamental limitation, but in practice it becomes very difficult. The low flexibility of this kind of grid molds favors development of air bubbles between the substrate and mold during the replication, therefore, high pressure is needed to expel the bubbles out of the printed material. However, any submicron impurity trapped inside will damage both the mold and also the substrate. Thus, this is the reason that processing with hard molds is usually done in clean room conditions. Moreover, the fragility of this kind of grid molds requires the demolding step to be operated with care, sometimes using specific tools.

In this thesis, a hard mold is not adopted to imprint on the final substrate, however, the patterned silicon substrate (hard mold) is used to generate the soft and hybrid molds acting

as soft stamps for direct imprinting on the ultimate substrates, details are introduced in the next subsection.
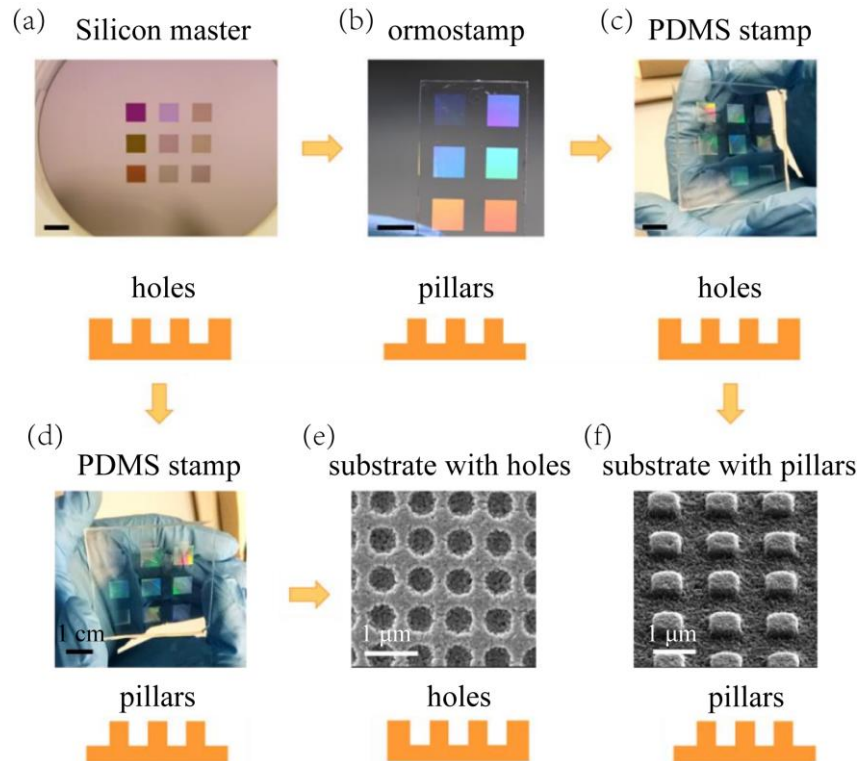

Figure 2.4: Sketch of replication process from original silicon master to the working PDMS stamp. Silicon master (a) is replicated to hard Ormostamp mold (b) to obtain PDMS stamp with holes (c) to imprint reversed pillars on ultimate substrate (f); or obtain pillars on PDMS mold (d) to imprint holes on substrate (e).

Operation procedure:

Pre-patterned silicon masters were purchased from Cemitec (Navarra, Spain). These original masters are fabricated by electron beam lithography, interference and deep UV lithography. The availability of multiple replications of these pre-patterned silicon wafers enables the production of hundreds of replicas, and from these replicas hundreds of replicas more can be generated. The master used in this thesis consists of arrays of holes in a silicon wafer with lattice parameters ranging from 400 to 600 nm in 1 cm^2 areas each (Figure 2.4a).

To obtain replicas from silicon masters, the first step is to silanize the master with an anti-sticking layer of 1H,1H,2H,2H-perfluorooctyl-trichlorosilane (FOTCS) on top. The anti-sticking layer can avoid the adhesion of resist and silicone during the replication, and prevent the damage of original silicon master during the de-molding. The silicon master is placed in a vacuum chamber with 5 µL of the silane for 30 min. In the vacuum atmosphere, the evaporated silane molecules bond covalently to the silicon surface and result in a super hydrophobic surface. Then, the silicon wafer is rinsed with acetone at 150 ºC for 30 min to remove the excess of silane for guaranteeing the smoothness of the master surface, which is crucial in this step.

A hard negative-replica (Figure 2.4b) of the original master can be obtained with Ormostamp (Microresist technology). Ormostamp is a photocurable resist that has high Young modulus (650 MPa) and it is suitable to replicate features with high mechanical stability and high aspect ratio. Thus, using this hard mold with negative pattern we can replicate a soft stamp with the original pattern, and further obtain the negative pattern on the target substrate (Figure 2.4c, f).

Hard UV-NIL technique is used to obtain hard masters with negative pattern. A drop of Ormostamp photoresist is placed on the original master and then covered with a pre-cleaned glass slide gently and making sure that no bubbles remain inside. After the photoresist is fully spread between the two substrates, UV is employed to cure for 5 min and crosslink the photoresist. Finally, to demold the Ormostamp master, it is placed on a hotplate at 160 ºC until the Ormostamp master detaches from the silicon master due to the difference in thermal expansion.

2.3.3.2 Soft mold

A welcomed alternative to hard molds is soft elastomeric molds which can be replicated by casting of silicone elastomeric materials on the patterned grid molds. The material of choice for the soft molds is mainly polydimethylsiloxane (PDMS), which is widely used in microcontact printing [81],[82]. These soft and flexible molds own some advantages with

respect to the issues that appear in hard molds. First, the elastomeric features adapt better and their contact with the surface is less harmful to the substrate. Thus, this enables the soft molds to be used to imprint curved and irregular substrates. Second, PDMS has low surface energy, so no anti-adhesive coating is required for soft molds, as for silicon- or silica-based hard molds. The low surface energy also enables the demolding process faster than for the hard molds pattern transfer, making large scale and roll-to-roll printing more compatible. Third and finally, soft NIL is less sensitive to the surface impurities and contamination than the hard molds, which offers the probability of fabrication of the patterned substrates out of cleanroom environment for cost saving. However, the feature size and imprint resolution of soft PDMS molds are limited to few hundred nanometers due to the low Young modulus (around 2 MPa), so the soft relief features tend to deform with the pressure applied during the imprint process.

In this thesis, NIL only with soft mold is not used due to the less ideal resolution compared with hybrid soft molds which will be introduced in the following subsection. The protocol for the preparation of soft PDMS mold as elastomeric backbone is the same as in the soft mold imprint system.

Operation procedure:

The materials for the preparation of soft PDMS molds in this thesis were ordered from Dow Corning. First, a mixture with ratio of 10:1 of the pre-polymer and curing agent are mixed vigorously and degassed for around one hour (this time depends on the amount of mixture) to remove bubbles from the mixture. Then, the mixture is poured onto the master and left for degassing for one more hour to be sure that the polymer fills the pattern completely. Subsequently, this "liquid" polymer is cured at 100 ºC for one hour. After it is cured, the soft PDMS can be gently detached from the master.

2.3.3.3 Hybrid mold

To overcome the limitations that using soft molds and hard molds, hybrid molds that preserve the advantages of the soft and the hard ones have been developed. A hybrid mold consists of a thin layer of hard material with features which is supported by a much thicker soft material as flexible backbone. The hard material becomes flexible when its layer thickness goes down to micrometers level while still retaining its hardness due to its sufficient Young modulus allowing to imprint features with high aspect ratio [83]. The backbone as a supporting material ensures mechanical stability and flexibility for demolding. These hybrid molds in NIL can transfer features down to few tens of nanometers and are suitable for large-scale industrial production.

In this thesis, the hybrid molds are used to imprint holes and inverted pyramid arrays with different lattice parameters and diameters/side-length. These hybrid molds consist of an imprinting layer of hard PDMS (h-PDMS) with a soft PDMS backbone. Similar to the soft PDMS, h-PDMS is also an elastomeric silicone but with higher (5 times, about 10 MPa) Young's modulus than the soft PDMS and dedicated to the imprint pattern with resolution down to a sub-20 nm scale [84]–[87].

Operation procedure:

The materials for the preparation of hard PDMS in this thesis were obtained from Gelest (USA). First, 9 µl of the catalyst (Platinum divinyltetramethyldisiloxane), 50 µl of the modulator (1,3,5,7-tetramethylcyclotetrasilane), 0.5 g of hydrosilane polymer (hydroxyl siloxane) and 2 ml of toluene (69% wt) are sequentially added into 1.7 g of the vinyl prepolymer (7-8% vinylmethylsiloxane) under stirring. Due to the toluene evaporation, this mixture solution becomes solid within around 20 min. Therefore, while the mixture is still liquid, a drop of it is casted on the master and spread evenly with blowing air, this step ensures that the entire structure is filled with PDMS. Then, the previous step is repeated for two or three times until the full substrate is covered, afterwards the substrate is left for one hour at room temperature and one hour at 60 ℃ for curing the h-PDMS. At last, a soft PDMS backbone is formed on top as introduced in the chapter 2.3.3.2.

2.4 Dry and wet etching

2.4.1 Dry etching-Reactive ion etching (RIE)

RIE is an ion-assisted reactive dry etching process to remove material from a substrate for the production of topographical patterns used in manufacturing of printed circuit boards or other micro- and nano-fabrication procedures. In the etching system, the substrate is placed in a vacuum chamber where the plasma is introduced, then a highly anisotropic etching process starts through the application of energetic ions bombarding the substrate and leading to the plasma chemical etch. Anisotropic etching removes material in specific directions allowing the production of geometric features such as deep trenches and sharp corners in contrast to isotropic etching, which produces a lower resolution concave shape under the photoresist etching mask. RIE is widely used for etching nanoscale features because it will etch in a downward direction with almost no sideways and undercut etching. Another reason for using RIE to obtain small features is the ability of gas species to diffuse into smaller features better than liquids. Moreover, due to the chemically mediated nature of the etching reaction, the RIE shows a selective etching if the constituents are properly chosen. Generally, the etching ratio of the underlying substrate (*e.g.,* silicon) needs to be improved against the patterned mask layer (usually resist). In this thesis, RIE etching technique is used to expose holes on silicon substrates using a combination of O_2 and O_2/SF_6 mixture gases.

Operation procedure:

In this thesis, RIE is used remove the remaining resist and Ge in the holes that are fabricated by T-NIL technique. The holes on the resist covered substrate are imprinted from the pillars with lattice parameter (LP) of 400 nm (diameter: 296 nm, height: 390 nm), LP of 500 nm (diameter: 298 nm, height: 390 nm) and LP of 600 nm (diameter: 330 nm, height: 390 nm). The etching protocol for these three types of holes with different LP is the same.

A PlasmaPro Cobra 100 system (Oxford Instruments) is used for RIE. The residual resist was etched by O_2 plasma at 50 sccm, 12 mTorr and a high field power of 50 W for 2 min, whereas

for the Ge layer a mixture of O_2/SF_6 at 5/30 sccm, 15 mTorr and a high field power of 75 W for 2 min was employed for RIE.

2.4.2 Wet etching-Chemical reagent etching

Wet etching refers to the removal or dissolving of material from a wafer when immersed in liquid chemicals or etchant solutions. Specific patterns are defined on the wafer by means of a hard mask that is deposited and patterned on the wafer prior to the fabrication process using lithographic methods [88]. Selective etchants which preferentially etch the substrate are used. The wet etching process is either isotropic (direction independent) or anisotropic (direction dependent) as shown in Figure 2.5. Generally, most of the wet etching processes are isotropic, which is sufficient for geometries larger than 3 μm. For isotropic wet etching, material (*e.g.,* silicon) is removed uniformly from all the orientations in the chemical such as the acidic mixture of HNA (hydrofluoric, nitric, acetic). For anisotropic etching process, material is removed uniformly in vertical orientation (fewer masks undercut, more removal in vertical walls). Wet etch anisotropic processes take advantage of the fact that the etch rate of crystalline material in the chemical solution depends on the crystal surface that is exposed to the etchant. For example, silicon etching is highly anisotropic in the etchants potassium hydroxide (KOH) or tetramethylammonium hydroxide (TMAH). Etching a (100) silicon wafer would result in a flat and angled wall that ends displaying a pyramidal structure exposing (111) silicon faces. Details are explained in chapter 3.
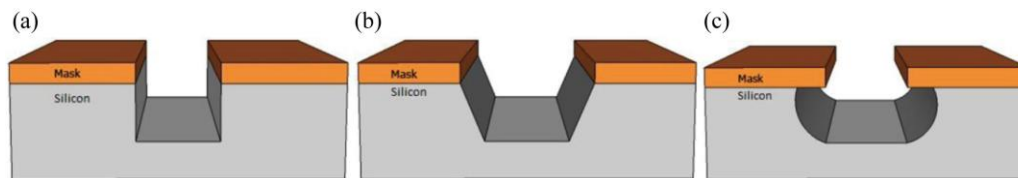

Figure 2.5: Comparison of dry and wet etching processes for silicon (a) Completely anisotropic (b) Partial anisotropic and (3) Isotropic etching of silicon [89].

In this thesis, only anisotropic wet etching method is used to etch the crystalline silicon to produce regular inverted pyramid arrays for the photonic/plasmonic application.

Operation procedure:

Before wet-chemical etching, an adhesion-enhanced KOH-resistant resist is coated on the backside of the 2-sides polished substrate for its acting as a protective layer during the chemical etching. Protective resist AR-PC 503 (ALLRESIST) is spin-coated on the backside of the silicon wafer at 1000 rpm for 60 s and the wafer is baked at 140 ^{o}C for 1.5 min on hot plate. Second, a fresh KOH solution of 33 wt% concentration is prepared and heated up to 85 ^{o}C. Then, anisotropic wet etching is performed by immersing the samples, previously processed with dry etching, in the as prepared KOH solution for 30 s, then immediately taken out to rinse with water and dry with N_2. Finally, the as treated samples are put into a 30% H_2O_2 solution for 5 min in order to remove the remaining sacrificial Ge, then rinsed with water and blown dry with N_2.

2.5 Characterization of the samples

Following the fabrication of nanostructures, the samples received morphological, optical and electrical characterizations using the techniques described in this section.

2.5.1 Morphological characterizations

2.5.1.1 Scanning electron microscopy (SEM)

Scanning electron microscopy is used to characterize the topography and composition of the samples at the nanoscale. Secondary electrons (SE) reveal detailed information of the morphology while the backscattered electrons (BSE) show differences in composition. In structures with different layers, BSE mode can help to distinguish them. A scanning electron microscope Quanta FEI 200 FEG-ESEM was used in this thesis. Both high vacuum condition mode (10^{-5} mbar) at voltages from 15 to 20 kV and low vacuum mode (0.6 mbar water vapor atmosphere) at voltages from 5 to 10 kV were applied depending on the conductivity of the sample. Low vacuum mode is used to alleviate the surface charge that can influence the stability of imaging. For instance, morphology characterization on samples using the n-type

semiconductor polymer, were measured under low vacuum mode to reduce charge-up effects on the polymer layer.

2.5.1.2 Profilometry

Profilometry is used in this thesis to measure the thickness of deposited films. The used equipment is a KLA Tencor D-500 profilometer. The equipment scans the sample horizontally (0.1 mm s^{-1} for our measurement) using a diamond tip to contact the sample with a selected contact force (0.03 mg for our measurement) depending on the film hardness. The vertical and lateral resolution of scanned features can reach a few nanometers and submicron scale, respectively. In general, the film is scratched down to the substrate with a line feature, the height difference is recorded transversely across this line. This characterization has been intensively used to get the thickness of the desired film to be patterned. It also has been used to study the influence of the thickness of the patterned film on the obtained electrical and optical properties of the device.

2.5.2 Optical characterization: Fourier Transform Infrared Spectroscopy (FTIR)

The optical properties of the fabricated structures are characterized by measuring the reflectance (R) and/or transmittance (T) in the visible and near infrared from 400 to 2500 nm wavelength with FTIR. A Bruker Vertex 70 FTIR spectrophotometer attached to an optical microscope (Bruker Hyperion) is used in order to locate the appropriate position of the sample for the measurements. A 20x objective with numerical aperture (NA) of 0.4 and spot size of 160 μm^2 was used for the signal acquisitions. The reflectance measurements were normalized against silver and gold mirrors in visible and infrared regions, respectively, whereas air was used to set the reference for the transmission measurements.

2.5.3 Electrical characterization

2.5.3.1 Current-Voltage (I-V) measurements

Current-voltage measurements (I-V) of the devices allow to extract figures of merit like open circuit voltage (V_{oc}), short-circuit current (I_{sc}), power conversion efficiency (PCE) and fill factor (FF). For the I-V acquisitions we used a AM1.5 solar simulator. The input power density was set to 1 sun using a NIST-traceable calibrated reference cell (Newport 91150 V). The lamp spectrum was acquired by calibrated spectrometers (USB2000 and NIR512, Ocean Optics).

2.5.3.2 Photocurrent measurements

The photocurrent setup consists of a supercontinuum White laser (Fianium PM-SC) coupled to a Fianium monochromator (LLTFContrastTM), with the power calibrated by standard photodiode power sensors (Thorlabs S120C, 400-1100 nm, 50 mW; Thorlabs S122C, 700-1800 nm, 40 mW). The electric characterization was performed with a Keithley 2450 SourceMeter equipment.

2.5.3.3 Responsivity mapping measurements

The responsivity mapping setup consists of the white laser and monochromator combination, with the input power calibrated by a standard Ge photodiode power sensor (Thorlabs S122C, 700-1800 nm, 40 mW). The beam impinged onto the sample through a Mitutoyo near-infrared range 10x objective long working distance lens. The sample was mounted onto a XY Mount (XYF1/M). In the procedure, the sample was moved along the XY plane manually to extract the photocurrent maps. The electric characterization was performed with a Keithley 2450 SourceMeter. Then photocurrent results were converted to responsivity. The data collection was obtained with LabView 2018 developed software.

2.6 Simulation method: Finite-difference time-domain (FDTD)

In this thesis, a numerical simulation software is used to predict the optical and electromagnetic properties of the plasmonic inverted-pyramid structures, aiding their design.

Moreover, these calculations allow to identify the origin of the optical features measured and to optimize the designed structure to accomplish the desired behavior.

Lumerical finite-differences time-domain (FDTD) solutions (www.lumerical.com) was used for the numerical simulations. FDTD was first developed in 1966 by Yee [90]. It works by replacing all the derivatives in Maxwell's equations with finite discrete grids (Yee cells), and their time evolution steps with a leapfrog algorithm. The Maxwell equations are solved for each cell at each time step until a steady state is reached. In our simulations, the geometry and size of the simulated objects are extracted from SEM microscopy as average values over the pattern, to define a unit cell with periodic conditions impinged by a linearly polarized plane wave acting as light source. In practical simulations which cannot be implemented over an infinite space, the perfect matching layer (PML) technique is used to address the propagation of electromagnetic wave into the infinite. Specifically, PML is placed around the simulated structure. The electromagnetic energy is nearly totally absorbed by the boundary when the electromagnetic energy impinges on it. Periodic boundary condition is used along the horizontal direction (x, y axes) to simulate the periodic pyramid array. The reflection, transmission and electromagnetic profiles are acquired by adequately placing power and profile monitors. The accuracy of the calculations depends on the size of the mesh and the time step. Smaller mesh sizes and time steps can improve the accuracy of the results, but will need more memory and be very time consuming. Moreover, the FDTD simulation requires calculating the electromagnetic field over the entire space instead of only inside the object. The calculations are therefore very large. So different sizes of mesh are applied in the simulated structure in order to calculate in an affordable time and memory. For sub-micron structures, 4 nm of mesh is used, while for size in few microns, 10 nm of mesh is used. The complex refractive index of N2200 polymer was obtained from ellipsometry measurement. Gold data was extracted from Johnson and Christy [91], and Molybdenum trioxide (MoO_3) [92], silicon [93], indium tin oxide (ITO) [94] were obtained from known databases.

Chapter 3

Efficient infrared sunlight absorbers based on gold-covered, inverted silicon pyramid arrays

Besides dominating electronics industry, silicon also finds wide applications in photovoltaics, primarily due to its cost-effective and efficient manufacturing process [95]–[97]. However, as in any solar cell, the exploitable spectral range of sunlight is limited by the band gap of the active photovoltaic material, which in the case of silicon is 1.1 eV, leading to an absorption edge roughly at 1100 nm. Thus, nearly half of the solar spectrum remains unabsorbed, namely, the near infrared (NIR) part [98]. To alleviate this situation, a common alternative to photoelectric conversion relies on the mechanism of plasmon-enhanced internal photoemission of hot electrons at metal/semiconductor hetero-structures. NIR photons with energies below the gap of the semiconductor are absorbed by the metal, launching surface plasmons, which, upon relaxation, produce a photocurrent of hot carriers into the semiconductor [54],[99]–[101]. For an overview of the different applications of plasmon-induced hot electrons, including solar energy harvesting, we refer to several recent reviews and references therein [47],[48],[102],[103].

The excellent concentration and light manipulation properties of surface plasmons can be further enhanced by nanostructuring of the metal/semiconductor system [100],[104],[105]. In this respect, silicon offers a fairly simple opportunity for its texturing in the form of both inverted and upright square pyramids, due to the strong anisotropy in the etching speed along different crystallographic planes, when KOH is used as etcher. This kind of nanostructuration of the metal–silicon interfaces has already been used to enhance the performance of Si solar cells [106]–[109]. Furthermore, inverted Si pyramid arrays have been successfully implemented as surface enhanced Raman scattering (SERS) substrates, either directly [110] or by serving as template for the preparation of upright bulk metallic pyramids [111] or pyramidal arrays made of perfectly piled gold nanoparticles [112]. For the purpose of this work, however, the ansatz of implementing both types of pyramids, covered with different

metals (Au, Al and Cu), in internal-photoemission detectors is of great interest. In fact, promising responsivity figures of merit have been already reported for the NIR wavelength range (ca. 1–2.7 μm) [113]–[116].

In this work, we propose a strategy for harvesting NIR sunlight based on the fabrication of silicon inverted-pyramid arrays covered with thin Au films. The textured structures are obtained either by scalable soft nanoimprint lithography (sub-micron size pyramids) or conventional photolithography (few micron-size pyramids), subsequent wet KOH etching and thermal Au deposition. A germanium layer deposited onto the Si wafer by molecular-beam epitaxy (MBE) serves as hard mask in the fabrication process of nano/micro-scale inverted pyramids due to its easy dissolution in hydrogen peroxide (H_2O_2) but high resilience against KOH. Here we show the complete results for two representative pyramid sizes of each size class. By illumination from the semiconductor side with NIR light (wavelengths between 1 and 2.5 microns), surface-plasmon polaritons can be excited at the Au/Si nanostructured interface, leading to well-defined absorption bands in the NIR transmission spectra and the converse features in reflectance. The calculated near-field distributions for the observed surface-plasmon resonances indicate the existence of hot spots along the contour of the pyramids, where the electromagnetic field intensity becomes strongly enhanced (up to two orders of magnitude, depending on pyramid size) with field vector components perpendicular to the pyramid facets. Similar to the lightning-rod effect, all of these factors are predicted to be crucial for photocurrent generation in plasmonic nanostructures. This allows us to foresee great potential for Au/Si pyramidal arrays for the generation of hot-carrier photocurrents by internal photoemission for energy harvesting applications or photodetectors with improved sensitivity in the infrared.

3.1 Results and discussion

Arrays of inverted Si pyramids with sizes roughly between 300 to 700 nm were fabricated by nanoimprint lithography following a similar method as published elsewhere [117]. Different key steps of the fabrication process are depicted in Figure 3.1 together with the resulting nanostructures, as shown by the corresponding secondary electron micrographs

(SEM). The detailed fabrication process of inverted nano-pyramids is described in Chapter 2. As shown by the SEM pictures in Figure. 1e and f, we were able to fabricate high-quality large-area arrays of perfectly ordered and identical inverted Si/Au pyramids.
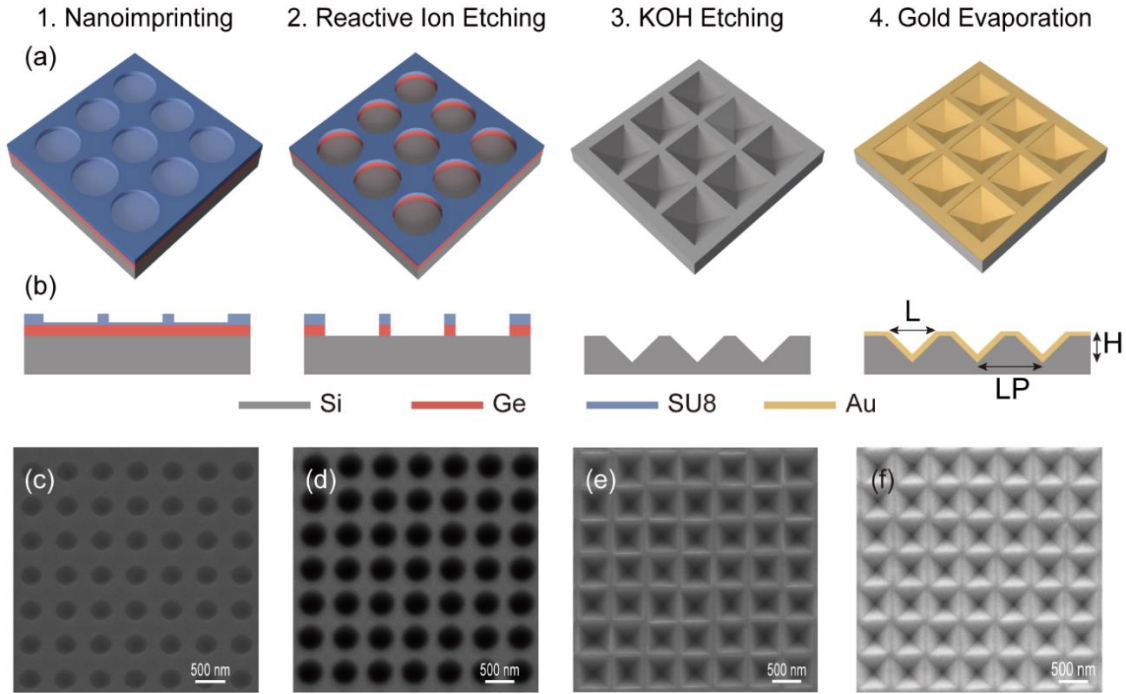

Figure 3.1: Fabrication of the arrays of nano-scale inverted pyramids covered with Au film. (a) Schematic of the main steps of the fabrication process. (b) Corresponding cross-section sketches for each process step (1–4). (c–f) Top view scanning electrons microscopy (SEM) images corresponding to process steps (1–4).

Larger pyramids with sizes ranging from 3 to 5 microns were fabricated by conventional photolithography for practical reasons. A sketch of the different steps of the fabrication procedure is displayed in Figure 3.2. The detailed fabrication process of inverted micro-pyramids is described in Chapter 2.
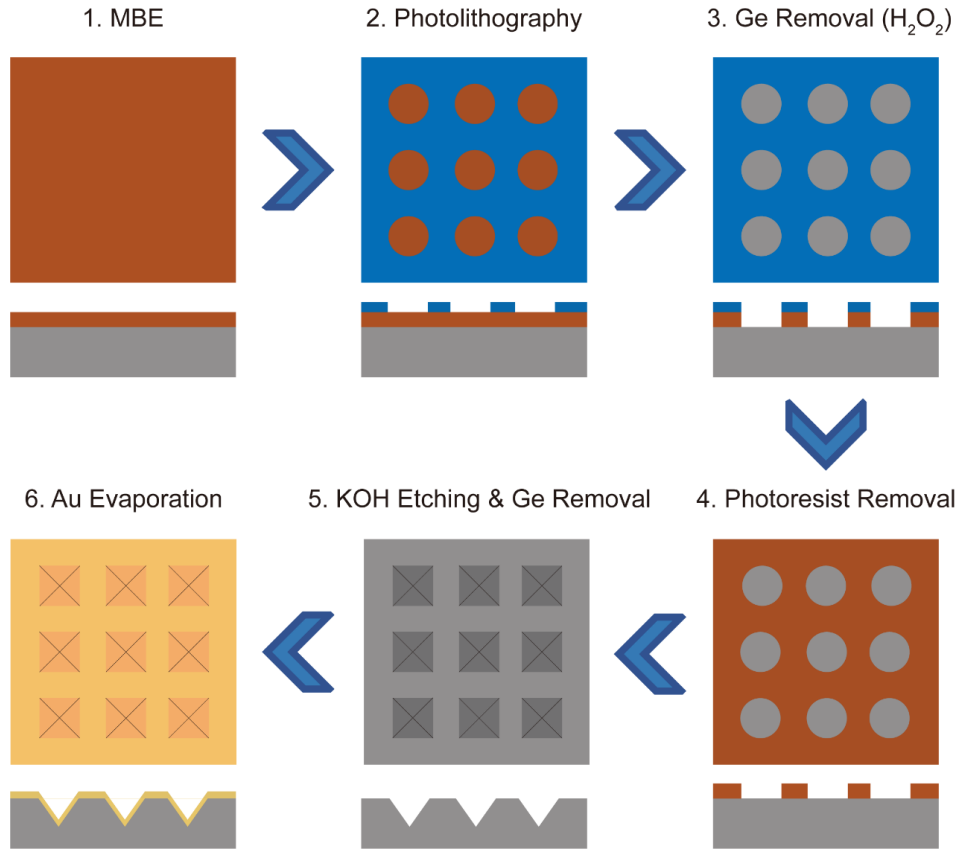
Figure 3.2: Different steps of the fabrication procedure of microns-size inverted pyramids by conventional photolithography and wet KOH etching.

The far-field optical response (reflection and transmission) as well as the near-field distributions of the Si/Au inverted-pyramid structures were simulated using commercial software (Lumerical) based on finite-difference time domain (FDTD) method. The numerical simulations were performed for linearly polarized light at normal incidence from the silicon substrate side and in the NIR wavelength range (1000–2500 nm). Literature data were employed to account for the wavelength-dependent refractive index and extinction coefficient of gold [91] and silicon [7]. The geometry of the simulated structures was obtained from the SEM micrographs of the actual samples. Figure 3.3 shows sketches of the geometry employed for the FDTD simulations regarding direction of incidence of the light, given by the wave vector **k**, its linear polarization corresponding to the electric field vector **E** with respect to the plane of the monitor (purple planes) used for the calculation of the near fields. Calculations were performed for two different planar monitors passing through the centre of a pyramid either bisecting two facets (0° monitor) or along two diagonals (45°

monitor). In this configuration, the incident light was either S- (perpendicular) or P-polarized (parallel) to the monitor plane, as indicated by the sketches in Figure 3.3.
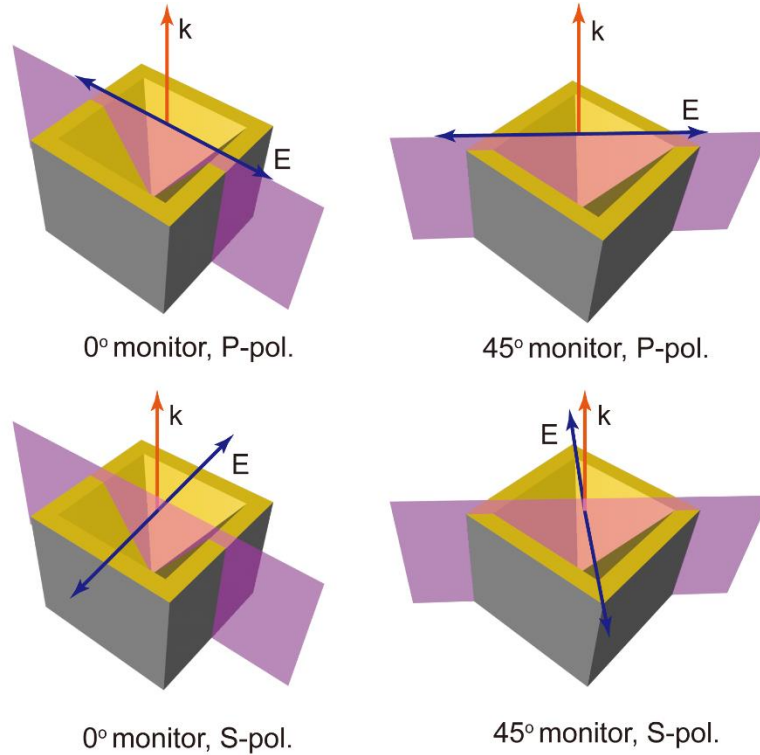

| 0° monitor, P-pol. | 45° monitor, P-pol. |
| 0° monitor, S-pol. | 45° monitor, S-pol. |

Figure 3.3: Sketches of the geometry used for the FDTD calculations including the cross-section monitor planes passing through the centre of the inverted pyramids either bisecting two facets (0° monitor) or along two diagonals (45° monitor). The light with wave vector k is either S-polarized or P-polarized, i.e. perpendicular or parallel to the monitor plane, respectively.

A single inverted pyramid was set as the unit cell for the simulations (Figure 3.4) using periodic boundary conditions (PBC) along the x and y axes and perfectly matched layer conditions along the z-axis. The pyramid and the surrounding medium were divided into a mesh for computing the finite differences. A variable mesh-size method with a minimum element size of 4 nm was adopted to save computational time and resources. For microscale pyramids, hence, the smallest mesh size was 20 nm.
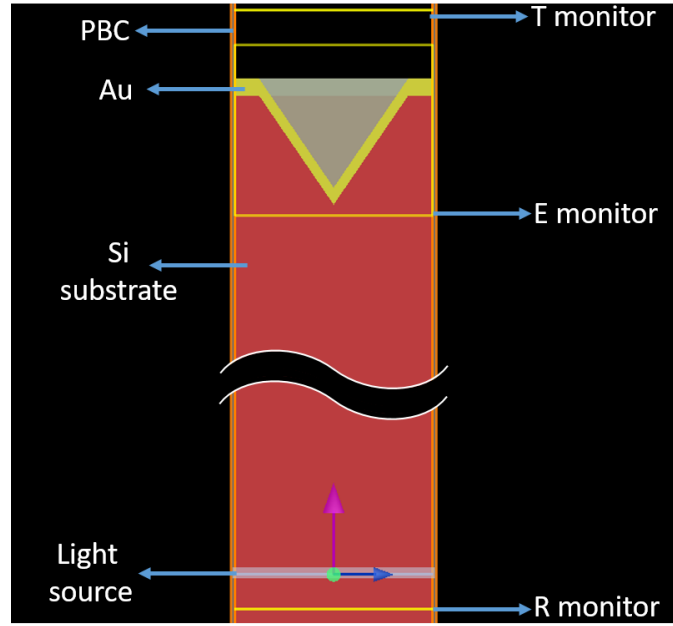
Figure 3.4: FDTD simulation model of the inverted-pyramid unit cell with periodic boundary conditions (PBC). Different elements are indicated by arrows like the light source, the Si substrate, the gold layer as well as the reflection (R), transmission (T) and electric-field (E) monitors.

Figure 3.5 shows SEM images of two representative arrays of inverted pyramids after the deposition of the thin gold film. The notation for the morphological parameters is shown in the sketches of Figure 3.1, which includes the pyramid base length L and height H as well as the lattice parameter LP of the array. Figure 3.5 thus displays the results for an array of small (L = 470 nm) and large (L = 4.1 μm) inverted pyramids. In both cases, the arrays exhibit extremely high regularity in shape and size of the pyramids. The insets to both panels of Figure 3.5 show a magnified view of a single pyramid, indicating again in both cases that the inverted pyramids are fully developed after KOH etching and that the surface of the deposited gold is continuous and smooth. We note that the regularity and high quality of the produced arrays typically extend over the entire pattern area up to 10×10 mm^2.
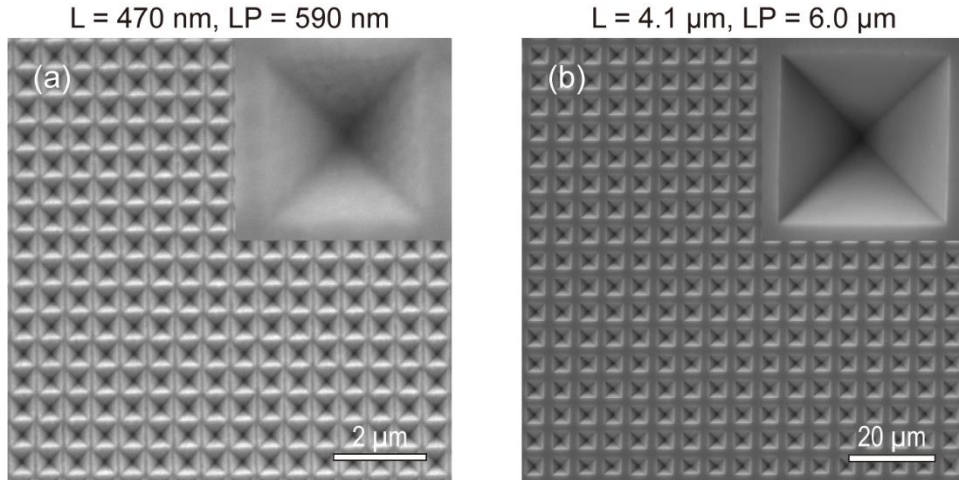
Figure 3.5: Inverted pyramid arrays covered with a 50 nm thick Au film. (a) SEM top-view image of representative small inverted pyramids with average L = 470(20) nm and LP = 590(20) nm. (b) SEM top-view image of representative large inverted pyramids with average L = 4.1(2) μm and LP = 6.0(2) μm. Insets: High resolution images of a single pyramid. Numbers in parenthesis indicate the experimental uncertainty.

Before discussing the optical properties of the inverted-pyramids, we show the results of a pre-screening of some array parameters, performed for sub-micron size pyramids in view of the computational cost of the FDTD calculations. For a given pyramid size the lattice parameter LP or pitch is crucial for the tuning of the optical response of the array. Figure 3.6 shows contour plots of the normalized absorption, calculated as a function of the incident wavelength and the lattice parameter LP, for an array of inverted pyramids with L = 500 nm covered with a 50 nm thick Au layer. It is instructive to analyse first the results of Figure 3.6 in more detail. For a given lattice parameter the normalized absorption exhibits a series of maxima which correspond to the different plasmon polaritons excited by the incident (white) light. From the evolution of the different maxima with increasing LP we can clearly distinguish between two types of plasmon polaritons [118]. The ones exhibiting a clear dispersion are called Bragg modes and correspond to propagating extended modes with strong photonic character. In contrast, the dispersionless modes (vertical lines in the LP versus wavelength plot) are called Mie modes and correspond to strongly localized modes. From the plot on Figure 3.6 it is clear that for any lattice parameter there is always certain

degree of mixing between Mie and Bragg modes. As shown below, this has an impact on the plasmonic/photonic character of the near field associated with the different polariton modes.
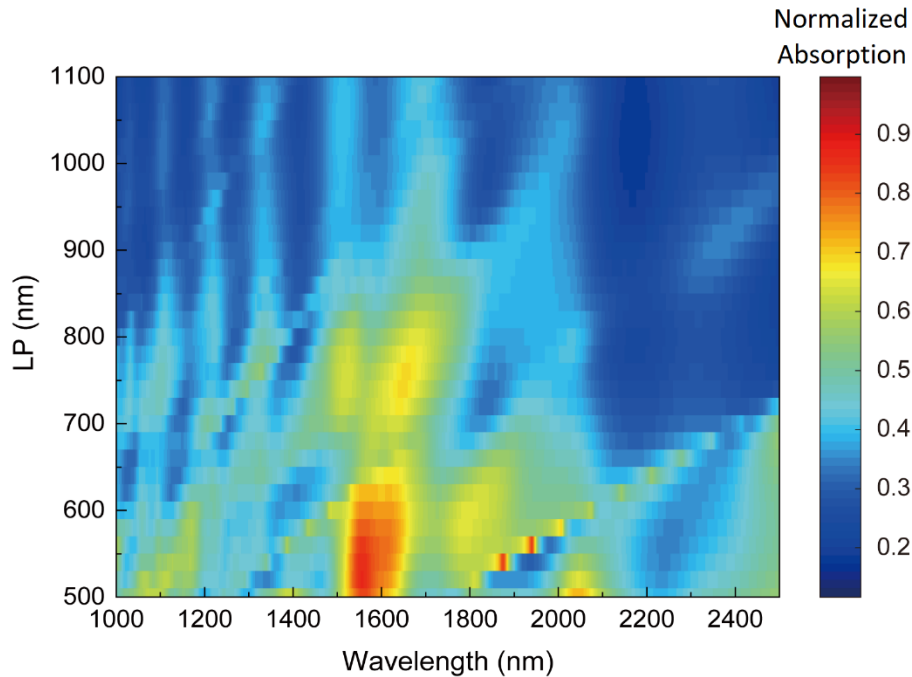

Figure 3.6: Contour plots of the normalized absorption as a function of the incident wavelength and the lattice parameter LP for an array of inverted pyramids with L = 500 nm covered with 50 nm of gold.

Regarding the dependence of the absorption on the array lattice parameter LP, we infer from the plot of Figure 3.6 that the resonances quickly loose intensity with increasing LP values. This is a consequence of the obvious fact that with increasing array pitch but constant pyramid size the ratio between patterned/flat areas also decreases. We have thereafter fabricated arrays with lattice parameters only 10% to 20% larger than the pyramid base size. In Figure 3.7, we also show the pre-screening of the gold layer thickness. The result is again straightforward: with increasing Au thickness light absorption increases rapidly from zero to a saturation value, reached above a thickness of ca. 30 nm. Consequently, we deposited routinely 50 nm of gold, so as to obtain smooth, strongly-absorbing Au layers.
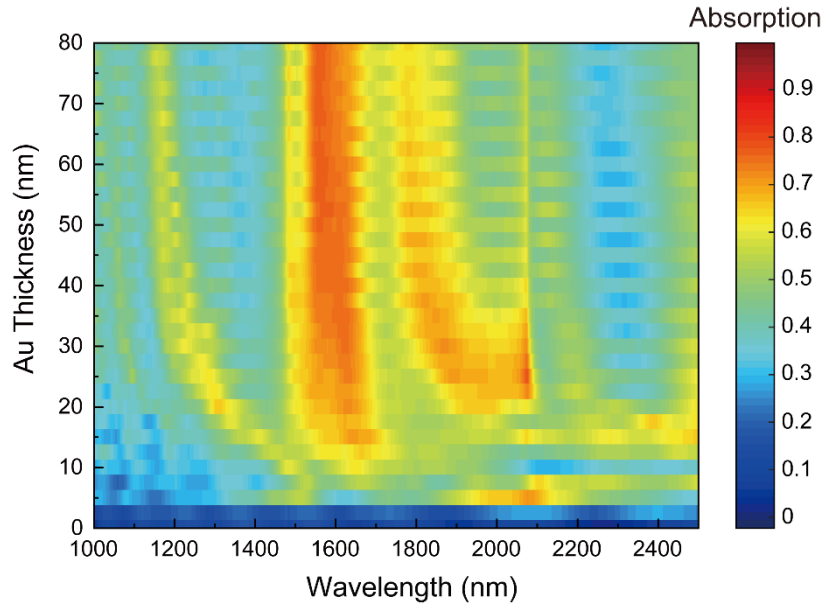
Figure 3.7: Contour plots of the normalized absorption as a function of the Au film thickness for a structure with L= 500 nm, LP= 600 nm.

Figure 3.8 shows reflectance spectra measured in the NIR range (1000 to 2500 nm) of a small-pyramid array (L = 470 nm, LP = 590 nm) before and after its coating with Au. The light, incident from the substrate side (indicated by its wave vector **k**), was either unpolarised or linearly polarized perpendicular to two pyramid facets (denoted as 0°) or along two pyramid diagonals (denoted as 45°), as depicted in Figure 3.3. For bare inverted pyramids without Au film, the overall reflectance for unpolarised light (black curve) is roughly featureless, ranging from 37–48%. In contrast, the thin gold layer has large impact on the optical response of the array (red, blue, green curves). From 1000 to 2000 nm the reflectance baseline decreases to less than 30%, but exhibiting a prominent broad peak at about 1600 nm. Above 2000 nm, the reflectance suddenly jumps to a constant value of ca. 56%. This edge-like profile arises from an optical phenomenon known as Rayleigh anomaly (RA), which is associated with light diffracted parallel to the surface of the regular array, acting as a grating [119]. The lowest order RA occurs at a wavelength given by:

$$\lambda_{RA} = n_{Si} \cdot LP \tag{1}$$

where $n_{Si} = 3.3$ is the refractive index of silicon in the NIR and LP is the lattice parameter of the array. In this case (LP = 590 nm), the Rayleigh anomaly is expected to occur at a wavelength of ca. 2 microns, in good agreement with the results of Figure 3.8. We point out that the Rayleigh anomaly coincides with the onset of diffraction [119]. This means that for longer wavelengths than λ_{RA}, any feature occurring in the optical reflectance (or transmission) of the periodic metallic nanostructure can solely be due to excitation of non-propagating, localized plasmon-like polaritons.
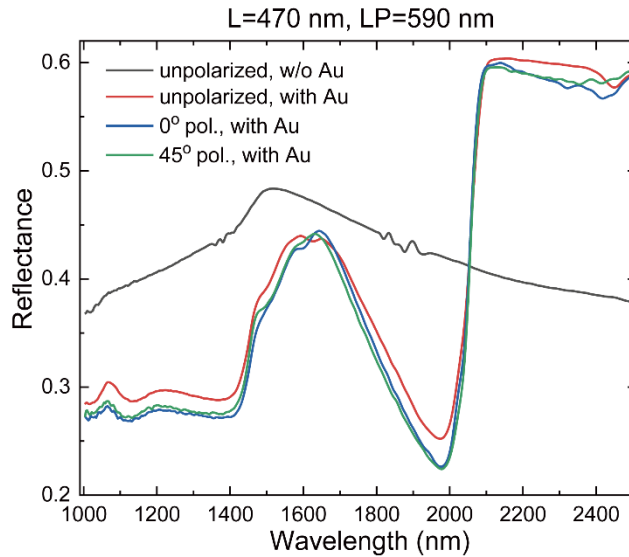

Figure 3.8: Measured reflectance spectra of an array of small inverted pyramids (L = 470 nm, LP = 590 nm) without and with Au layer for normal incidence from the Si substrate side and for different polarizations: unpolarised, 0° and 45° polarization.

Interestingly, the results of Figure 3.8 also indicate that the far-field optical response of the inverted pyramid array is fairly insensitive to the degree of polarization of the incident light. All three curves (red, blue, green) of the Au-coated array fall essentially on top of each other, having only qualitatively insignificant differences. This is simply due to the perfect square symmetry of the pyramidal array, which makes all three cases (unpolarized, 0° and 45° linear polarization) equivalent from the point of view of the (vectorial, time averaged) electromagnetic field distributions. In fact, linearly polarized light at 0° can always be decomposed into two equal 45° components and, viceversa, light linearly polarized along the

pyramid diagonals can be decomposed into two equal 0° components. The unpolarized case is just the combination of both linear polarizations.

The results for the optical response of the fabricated structures are summarized in Figure 3.9, where we show the measured and calculated normalized absorbance in the NIR spectral range from 1000 to 2500 nm for two representative examples: An array with small (L = 470 nm, LP = 590 nm) and one with large (L = 4.1 μm, LP = 6.0 μm) inverted-pyramids covered or not with gold. The absorbance is directly obtained from the normalized reflectance (R) and transmittance (T), computed as A = 1 − R − T. We first point out that the agreement between experiment and theory is very satisfactory, qualitatively as well as quantitatively. In both cases, the introduction of the Au film leads to a strong increase in absorbance in the whole infrared region. For the small gold-covered inverted pyramids the overall measured absorbance is close to 80% for wavelengths below that of the Rayleigh anomaly. The two wavelengths, 1290 and 1950 nm, where the normalized absorbance reaches unity in the calculated response (see Figure 3.9a), correspond to the excitation of strong plasmon-polariton resonances. The corresponding near-field distributions are discussed below. For the large pyramids, the addition of the Au layer also causes an increase of the absorbance, though the effect is moderate in comparison with the small pyramids. The average absorbance thus increases from ca. 25% to 40%. Since the transmittance is nearly zero, this means that much of the light in the NIR range is reflected by the large, microns-size pyramids (about 60% of the light in average). We point out that after eqn (1) the Rayleigh anomaly is expected for the large pyramid array to occur at around 20 μm. This wavelength obviously falls outside the spectral range of our experiments. Hence, resonances associated with the various maxima observed in the spectra of Figure 3.9b correspond to propagating Bragg photon-like polaritons. In general, for these large sizes and due to the very high refractive index of Si, the texturing of the Au/Si interface is not effective for IR light absorption, working the array as a reflection grating.
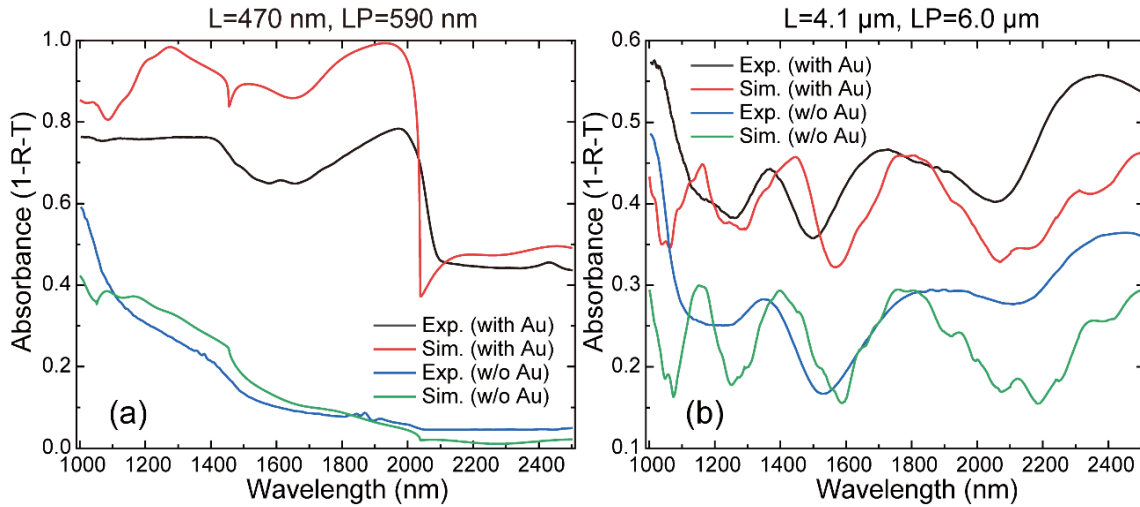
Figure 3.9: Measured and simulated absorbance $(1 - R - T)$ in the NIR spectral range of a representative (a) small (L = 470 nm, LP = 590 nm) and (b) large (L = 4.1 µm, LP = 6.0 µm) inverted-pyramid array with and without Au film.

Regarding the comparison between experiment and the numerical FDTD simulations, a clarification should be made. Whereas in the case of small pyramids the good agreement is almost for free, for large pyramids a special treatment of the theoretical data is required. We recall that the reflection experiments were carried out at normal incidence from the Si substrate side. Most of the light is then back-reflected from the textured Au/Si bottom interface. For large pyramids the onset of diffraction occurs at $\lambda_{RA} \sim 20$ µm, thus, in the NIR range from 1 to 2.5 µm a substantial portion of the light will be diffracted into higher orders. The propagation direction of these high-index modes forms large angles with respect to the substrate normal. Due to the large refractive index of Si, most of these higher-order modes undergo total reflection at the top Si/air interface and, hence, they cannot be detected. In addition, the small numerical aperture of the microscope objective used in the experiments ends up further restricting the collection of light to the zeroth order. As a consequence, we have written a script to pick up only the zeroth order contribution to the reflectance out of the FDTD simulations. In this way, we are able to attain reasonably good agreement between theory and experiment for micron-size pyramids, for example, as shown in Figure 3.9b. For submicron-size pyramids the zeroth order dominates the reflectance of the Au/Si inverted pyramid array, hence, no special treatment of the simulations is required.

Before discussing the near-field properties of the pyramidal arrays, it is instructive to revise the state of the art regarding the best possible conditions for hot-electron generation. In particular, we would like to bring to the fore the tight relation that exists between plasmon-resonance hot spots and hot-electron emission. For clarity, the discussion is based on a concrete example of a hot-electron device like the one depicted in Figure 3.10. The physical picture where the energy of the incident photon is entirely transferred to a single electron, which is ejected from the metal, holds only for the photoelectric effect with UV photons but certainly not for plasmon-resonance driven processes with photons in the NIR spectral range. In the latter case, when the photon excites a plasmon-polariton mode, its energy is distributed among a significant fraction of hot electrons, all having energies close to the Fermi energy [100],[101]. This is one of the main drawbacks of this kind of devices because most of the photoexcited hot carriers would not have enough energy to pass across the Schottky barrier (see Figure 3.10). There is, however, a way to circumvent this problem through quantum confinement. At the nanoscale, energy quantization effects cause the spreading of the electronic density of states, such that the energies of hot carriers after photoexcitation of the plasmon can be larger than the barrier height. This has been shown, for example, by computing the non-equilibrium plasmonic electron distributions of gold slabs, spheres and cubes embedded in Si [100] or water [104] with different sizes. For slab thicknesses below 30 nm a strong increase in the average efficiency of electron injection is observed [100] and, for a similar (linear) size of 5 nm, the total number of excited electrons increases by two or three orders of magnitude each time the shape changes from slab to sphere and from sphere to cube [104].
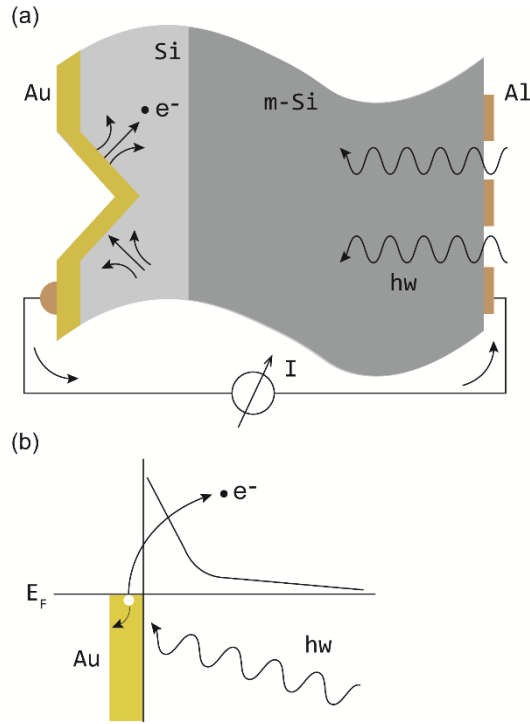
Figure 3.10: (a) Sketch of a possible hot-electron internal-photoemission Au/Si/n-Si/Al device based on inverted pyramids. (b) Profile of the electron potential along the dashed line in (a).

Another key issue for the generation and injection of hot electrons is the lightning-rod effect related to the enormous electrical field enhancements that occur when free charge is spatially concentrated in nano-sized regions. In fact, a comprehensive theoretical analysis of the hot-electron injection from metallic (Ag) nanostructures of different shapes into a semiconductor (TiO$_2$) with a similar band schema, as the one sketched in Figure 3.10b, shows that large field enhancement factors up to ca. 100 can be achieved in the NIR-visible spectral range for silver nanorods of large aspect ratio (length = 20 nm, diameter = 6 nm) [120]. Moreover, the generation rate of hot electrons is shown to be proportional to the square of the field enhancement factor [120]. However, the best example of the importance of hot spots for hot-electron generation is probably the work of Sousa-Castillo et al. [105], where it is shown how to boost the photocatalytic activity of TiO$_2$ nanoparticles by decoration of gold nanostars (best case scenario) with the titania nanoparticles themselves. The effect is ascribed to the ability of nanostars to locally create large electromagnetic field enhancements around their spikes, when illuminated with solar light, leading to strongly incremented hot-electron

populations at the metal–semiconductor interfaces. The authors even suggest describing this photocatalytic regime as driven by plasmonic hot spots [105].

Hence, in order to elucidate the potential of a given plasmon–polariton resonance for generating hot electrons by internal photoemission, we have analysed the spatial distribution of the near electromagnetic field, searching for hot spots. Such a distribution is obtained as the integrated response over the entire duration of the FDTD simulation. Calculations were carried out for certain special wavelengths using different planar monitors, corresponding to cross sections along pyramid facets (0°) or pyramid diagonals (45°) with light either S- or P-polarized (perpendicular or parallel, respectively) with respect to the corresponding monitor plane. Whereas the polarization turned out to be irrelevant for the far field, it is crucial for the local variations of the near field, the latter depending strongly on the plasmonic character of the polariton being excited.

Figure 3.11 shows the results of FDTD simulations as far as the near field is concerned, carried out for the same small pyramid array, whose far-field response was calculated previously, and for two special wavelengths, 1290 and 1950 nm, where the calculated reflectance reaches unity (see Figure 3.9a). As illustrated by the contour plots of Figure 3.11, for small pyramids the enhancement of the intensity of the electric-field component ($|E|^2/|E_0|^2$) for P-polarized light at the two selected wavelengths peaks mainly at different points in the very vicinity of the Au/Si interface. This is clear indication of the strong plasmonic character of these resonant modes, at least of its P-polarized component. Whereas for the 0° monitor the E-field intensity enhancement is typically greater than a factor ten, for the 45° monitor the enhancements can reach up to two orders of magnitude. In contrast, for S-polarized light (perpendicular to the plane of the monitors) the electromagnetic field is concentrated in regions close to the pyramid facets and tip but clearly separated from the Au/Si interfaces, as depicted in Figure 3.12. This is evidence of an outspoken photonic character of the S-polarized component; the maximum intensity enhancement remaining always below one order of magnitude.
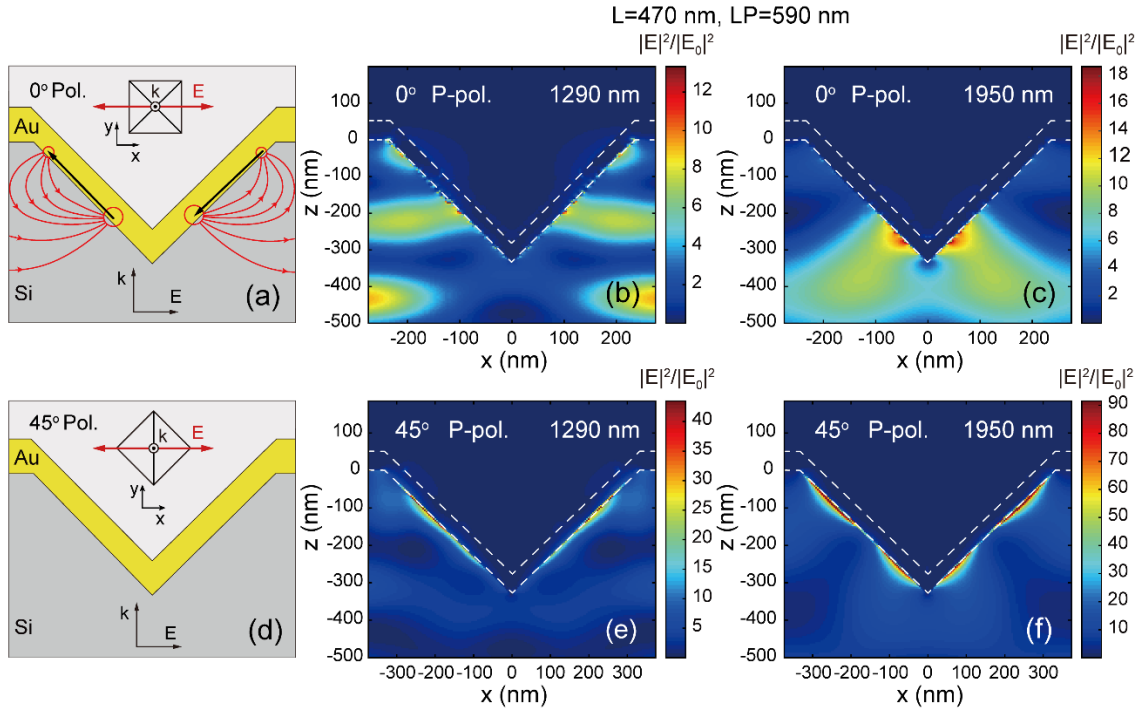
Figure 3.11: Near-field properties of small inverted pyramids (L = 470 nm, LP = 590 nm) covered with 50 nm of Au. (a) Sketch of the geometry and polarization configuration for a planar monitor corresponding to a cross section through the middle of the pyramid along two facets (0° monitor). K is the wavevector of the light and E the electric field component. (b) and (c) Near-field distribution for P-polarized light in the 0°-monitor plane for resonances at 1290 nm and 1950 nm, respectively. (d) Idem (a) but for a monitor along diagonals of the pyramids (45° monitor). (e) and (f) Idem (b) and (c) for P-polarized light in the 45°-monitor plane.
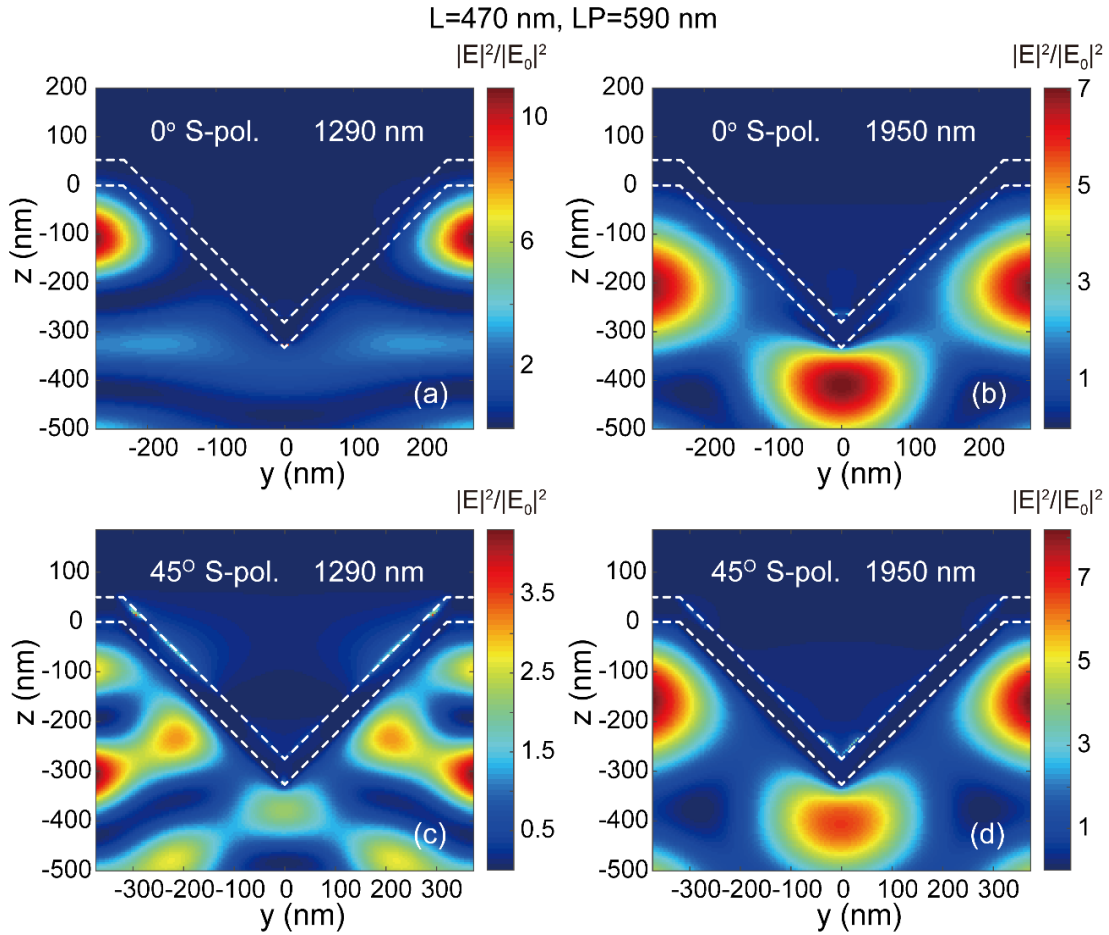
Figure 3.12: Near-field properties of small inverted pyramids (L=470 nm, LP= 590 nm) covered with 50 nm of Au. The light is in all cases S-polarized, i.e. perpendicular to the monitor plane. (a),(b) Case of 0º monitor, S-polarized light of 1290 nm and 1950 nm, respectively. (c),(d) Case of 45º monitor, S-polarized light of 1290 nm and 1950 nm, respectively.

From the point of view of the possible application for the generation and injection of hot electrons into the semiconductor, it is clear that the S-polarized components are useless. In contrast, the near fields associated with the P-polarized components present two key features. On the one hand, they produce large concentrations of charges at points or localized regions right on the surface of the inverted pyramids, the so-called hot spots, which produce extremely high electric fields. On the other hand, the electric-field vectors are perpendicular to the metal surface at the hot spots. This can be visualized in Figure 3.13, where we overlay the electric-field vectors to the intensity contour plots of Figure 3.11 for the 0° monitor. As

discussed before, both hot-spot features are instrumental for obtaining high hot-electron photocurrents in metallic nanostructures [104],[105]. An inspection of the field lines obtained from the FDTD calculations reveals that the hot spots on each facet correspond to the end-point charges of a sort of electrical dipole, oscillating with the same frequency of the incident light. Furthermore, the two dipoles in confronted facets are by symmetry in exact opposition. The sketch in Figure 3.11a illustrates the disposition of both induced dipoles. The effective net charge at each end of the dipoles or the charge separation might vary for different modes (wavelengths) and different monitors but for pyramid of this size we always find that NIR light induces two dipoles in opposition on the pyramid facets. This has an important consequence for the spatial distribution of hot spots. In particular, this explains why, contrary to intuition, the pyramid tip is never a hot spot. The reason is that the electric fields generated by each but opposite dipole exactly cancel each other at the pyramid tip.
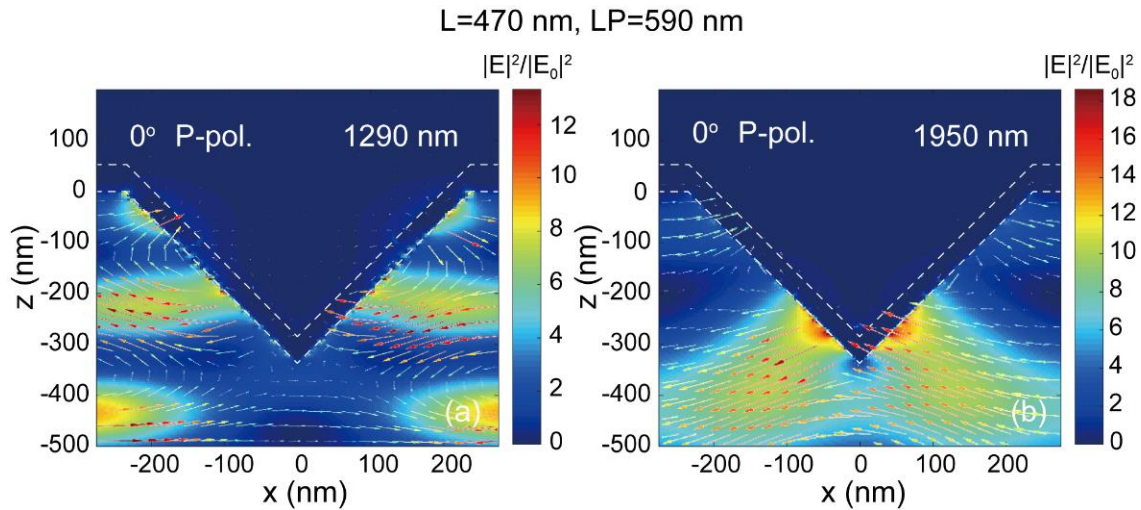

Figure 3.13: Visualization of the electric-field vectors for the near-field distributions calculated for P-polarized light, 0º monitor, at (a) 1290 nm and (b) 1950 nm for a small Au-covered, inverted pyramid array (L=470 nm, LP= 590 nm), corresponding to Figure 3.11b and 3.11c.

For large, microns-size pyramids their potential for hot-electron generation is less encouraging. Figure 3.14 displays the contour plots of the electric-field intensity of an array of large pyramids (L = 4.1 μm, LP = 6.0 μm) at two resonant wavelengths of 1450 and 1760 nm for both P and S-polarized NIR light with respect to a $0°$ monitor. The field-intensity

distribution reveals that these modes possess mainly photonic character, i.e. they are Bragg-like modes. Except for a few moderately intense hot spots for P-polarization at 1450 nm, all other field enhancements occur away from the metal surface in the space between the pyramids inside the silicon. The hot spots, however, now correspond to the end points of a series of dipoles aligned in head-to-tail manner along the pyramid facets.
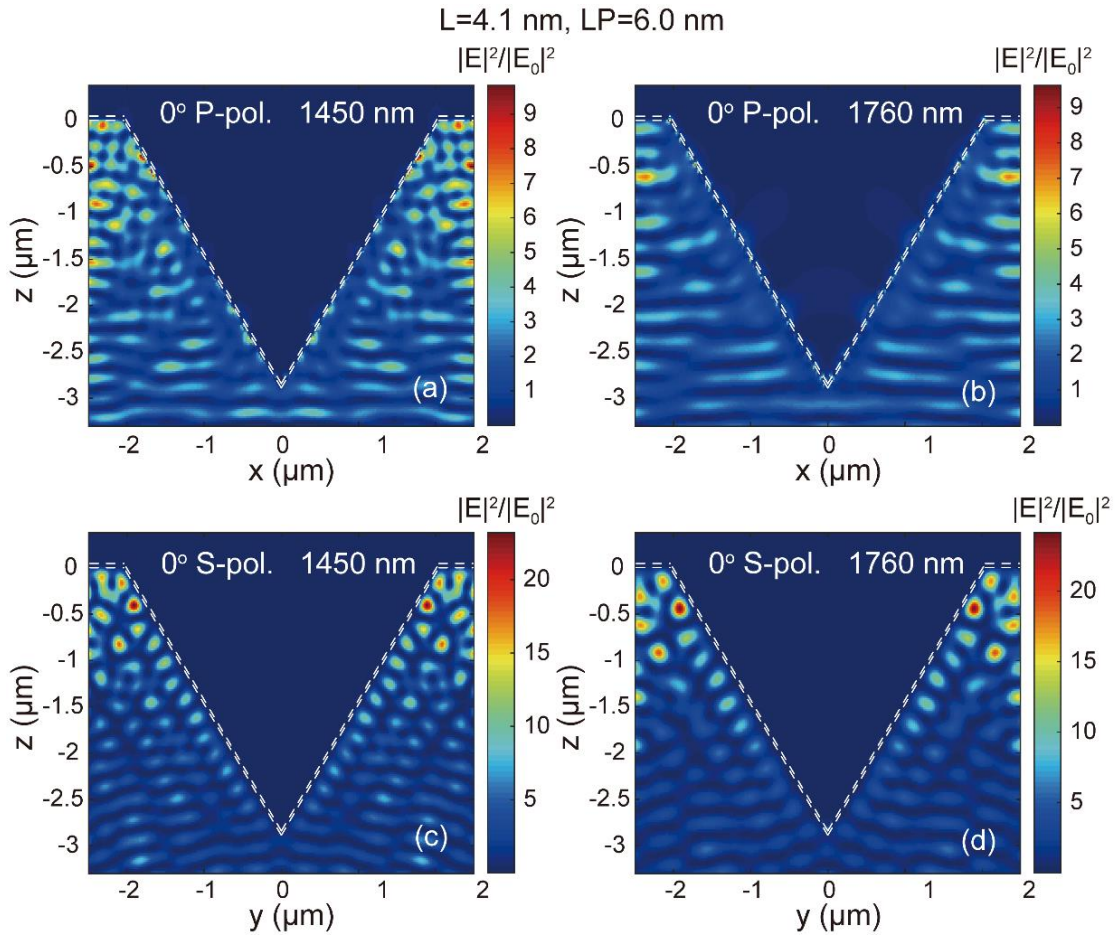

Figure 3.14: Near-field distribution of the electric-field intensity across 0° monitors for (a), (b) P-polarized light of 1450 nm and 1760 nm, respectively, and (c), (d) for S-polarized light of 1450 nm and 1760 nm, respectively, in the case of an array of gold-covered, large inverted pyramids (L=4.1 µm, LP= 6.0 µm).

3.2 Conclusions

In summary, an interesting alternative to current NIR light harvesters was presented, which is a plasmonic metamaterial based on micro/nanostructuring of silicon wafers by engraving arrays of inverted pyramids covered with a thin gold film, readily fabricated by scalable nanoimprint lithography combined with wet etching using KOH. For sub-micron-size pyramids the overall absorbance in the NIR spectral range (1 to 2.5 µm) can exceed 80%, which is shown to be due to the resonant excitation of plasmon polaritons sustained by the pyramidal array. Finite-differences time-domain simulations revealed that the near field associated with the plasmonic component of the polariton modes excited by NIR light presents several hot spots distributed throughout the Au/Si interface, characterized by strong enhancements of the electric-field intensity of up to two orders of magnitude. The existence of these hot spots is a prerequisite for enhanced photocurrents generated by internal photoemission of hot electrons from the metal into the semiconductor. Taken together, this points to the great potential of this type of Au/Si plasmonic/photonic nanostructures for their implementation not only in NIR harvesting devices but also for the application in infrared photo-detection, photo-catalysis, or cell photo-stimulation in the biological IR window, for example.

Chapter 4

Optical properties of inverted Si pyramids with partial number of gold-covered facets

The 4-facets Au/Si device with arrays of inverted pyramids as studied in Chapter 3, displayed high optical absorption in the near infrared spectral range from 1000 to 2500 nm due to the resonant excitation of plasmon polaritons sustained by the pyramidal array. The numerically simulated near field associated with the plasmonic component of the polariton modes excited by the NIR light presents several hot spots distributed along the Au/Si interface with strong enhancement of the electric-field intensity. The symmetrical structure of the device renders electric fields generated at each facet but opposite dipoles exactly cancel each other at the pyramid tip. Hence, hot spots are never observed at the pyramid tip, which is the desirable position to achieve injection of hot electrons for the inverted pyramids based photocurrent generators.

In this work, we adopted an innovative technique of oblique-angle gold evaporation on inverted silicon pyramids for breaking the structural symmetry of the Au/Si pyramid devices in the expectation of a redistribution of electric field towards the apex while still keeping high field enhancement. The hot spots at the apex of pyramids will result in electric-field vectors perpendicular to the metal surface, which is critical for increasing the probability of hot electrons injecting into the semiconductor. Moreover, the intense electric field at the tip can also help accelerating the injection of hot electrons.

With this concept in mind, in this work, we fabricated Si pyramids with partial number of gold-covered facets and characterized their optical properties. Numerical simulations of their near and far field properties have been performed to complete the study.

4.1 Results and discussion

The fabrication of inverted pyramids with partial number of gold covered facets shares the same method as we used for the full coverage, as described in Chapter 2 but with a crucial difference in the gold evaporation stage. Following the same pyramid fabrication protocol, a series of inverted pyramids with different L and LP are obtained. As we know, due to the different etching rate of silicon facets (100) and (111) in KOH solution, the etching rate of (100) facet is faster than the (111) facet which leads to a characteristic V-shaped cavity with side angle of 54.7° left on the Si wafer (Figure 4.1a). For the deposition of gold on the 4 facets of a pyramid, the angle of Si substrate with respect to the evaporation direction is kept at 0° during the evaporation, which means that the evaporated gold source vertically reaches to the whole surface of the Si substrate, i.e. all the Si surface will be covered with gold (Figure 4.1b). For the deposition of gold on solely 3 facets of the pyramids, the inclination angle of Si substrate is set at 35.3° during evaporation, in order that one of the side facets is turned to a vertical position. This vertical facet will preclude gold deposition whereas the other 3 facets become covered with gold, as illustrated in Figure 4.1c. For the deposition of gold on only 2 pyramid facets, the oblique angle of Si substrate is now set at 45° during the evaporation, in order that two adjacent facets are kept at vertical position. These two vertical facets will remain gold free, whereas the other 2 facets are covered with gold (Figure 4.1d). In this way, we prepared a batch of holders with different oblique angles and fixed the Si substrates on top, placing them in the evaporator chamber with vacuum pressure ranging from 1×10^{-6} to 3×10^{-7} mbar. The gold deposition rate was stabilized at around 6×10^{-2} nm s^{-1}. After the evaporation, samples were released from the holders, and we obtained the pyramid arrays with gold covered 2, 3 and 4 facets. These samples were used for further optical characterizations. A summary of all the geometrical parameters of the fabricated and simulated structures is presented in Table 4.1
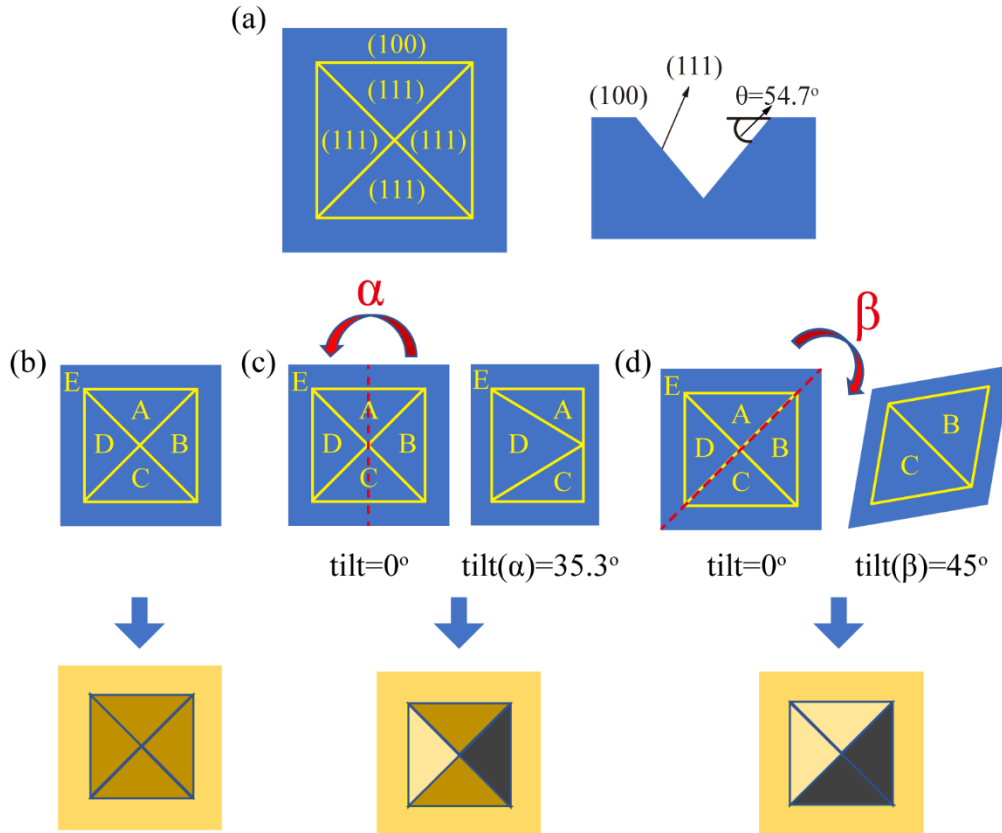
Figure 4.1: Illustration of gold deposition on Si substrates with pyramids. (a) Exposed facets of inverted pyramid on Si wafer. (b) Normal incidence deposition of gold on 4 facets of inverted pyramid. (c) Deposition of gold on 3 facets of inverted pyramid with 35.3º oblique angle. (c) Deposition of gold on 2 facets of inverted pyramid with 45º oblique angle.

Table 4.1: Geometrical size parameters of the fabricated and simulated structures: pyramid side length (L), lattice parameter (LP), pyramid height (h) and the thickness (t) of the gold deposited on top.

L (nm)	LP (nm)	h (nm)	t (nm)
340	400	240	50
450	500	318	50
515	600	364	50
320	500	226	50
240	500	170	30

There is a variation of gold thickness between the side facets of the pyramids and the flat surface of Si substrate (Figure 4.2). For gold coverage of 4 facets (Figure 4.2a), the thickness of gold on all the facets of the pyramid is equal to each other but thinner than the region between the pyramids (Figure 4.2c). For gold coverage of 3 facets (Figure 4.2b), the thickness of gold on the facet which is opposite to the vertical facet during the metal deposition is higher than the other two gold covered facets and the region between pyramids (Figure 4.2d), the latter which is now tilted. Figure 4.2e shows a SEM image of the device with 35.3º oblique angle gold deposition on 3 facets. The facet appearing with black color is the one without gold deposited on top, the two adjacent facets with slight bright color are covered with gold but with a smaller thickness than the facets with brighter color. A similar procedure was used to calculate the thicknesses for the gold coverage on two facets, that is the Au thickness of each facet was the nominal one (on the flat surface for normal incidence) but corrected by the cosine of the angle formed by the evaporation direction and the normal to the facet surface. Of course, we have used these thicknesses, as inferred from the geometry of the evaporation configuration, for all the numerical simulations of the near and far field properties of the devices with 4, 3 and 2 gold-covered facets.
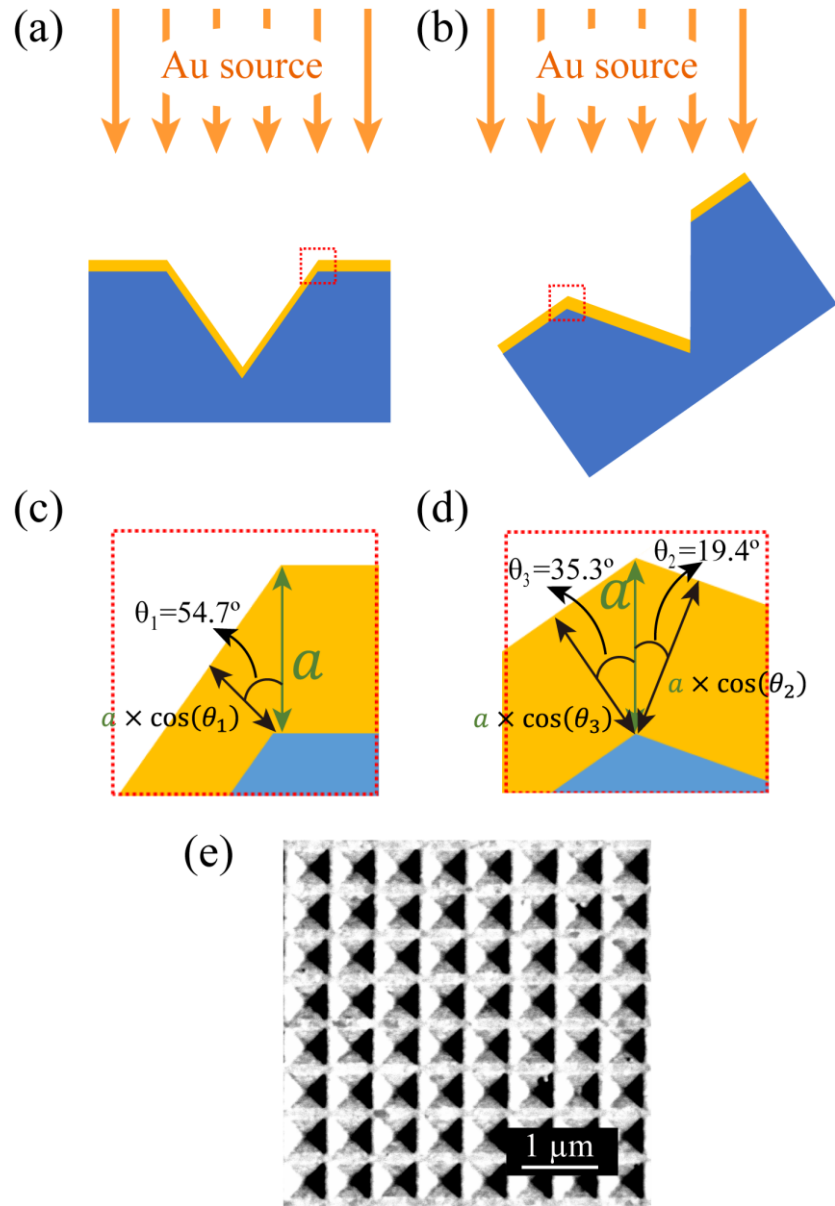
Figure 4.2: Gold on different facets of pyramid. Illustration of gold deposition without (a) and with (b) oblique angle (35.3º). (c) Thickness of gold on facets of pyramid without oblique metal deposition, corresponding to the dotted square area in (a). (d) Thickness of gold on facets of pyramid with 35.3º metal deposition, corresponding to the dotted square area in (b). (e) SEM image of device with 35.3º angle gold deposition (3 facets of pyramids covered with gold).

After the deposition of gold on Si substrates textured with arrays of inverted pyramids, a SEM characterization was carried out to check the morphology of the device surfaces. SEM

images of devices with pyramid array parameters equal to L = 515 nm and LP = 600 nm are shown in Figure 4.3. Before gold deposition, the inverted pyramids with regular shape and periodicity are etched in the Si substrate (Figure 4.3a, e). With 0° tilt angle gold deposition, 4 facets of pyramids are covered with gold, showing a perfect metal layer on the entire exposed Si surface (Figure 4.3b, f). With 35.3^o tilt angle gold deposition, it is clearly observed that only 3 pyramid facets have a bright color because they are covered with gold, whereas the remaining dark facet has no gold on top (Figure 4.3c, g). For 45° tilt angle gold deposition, only 2 facets of the pyramids are covered with gold (bright color), the remaining 2 facets with black color are uncovered (Figure 4.3d, h). For all these depositions, the thickness of the gold layers was large enough, to ensure a *continuous* (no pinholes, no cracks) gold film.
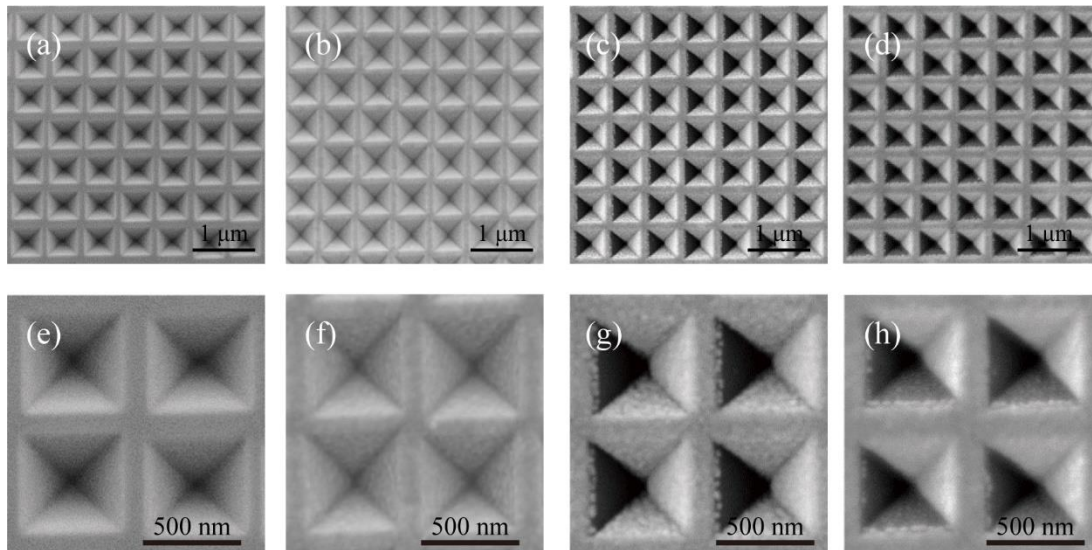

Figure 4.3: Low (top row) and high magnification (bottom row) SEM images of L = 515 nm, LP = 600 nm inverted pyramids on Si substrate without and with gold deposition (50 nm). (a, e) Pristine surfaces. (b, f) Gold deposited on the 4 facets of the pyramids. (c, g) Gold covering only 3 facets of the pyramids. (d, h) Gold covering only 2 facets of the pyramids.

Figure 4.4 shows the measured absorbance of L = 340 nm, LP = 400 nm, L = 450 nm, LP = 500 nm and L = 515 nm, LP = 600 nm inverted-pyramid devices with 4 facets covered with gold (50 nm). For L = 515 nm, LP = 600 nm device, the device shows high absorbance in the NIR range from 1000 to 2000 nm with a typical mode of maximal absorption located at 2000

nm, which is similar to the result obtained in Chapter 3. For L = 450 nm, LP = 500 nm device, a generally slightly decreased absorbance is obtained and the feature with maximal absorption blue-shifts to 1670 nm. For L = 340 nm, LP = 400 nm device, its absorbance further decreases and the feature of maximal absorption further blue-shifts to 1360 nm. The feature of maximal absorption shifts to the red as both the lattice parameter and pyramid size increase, as well as the Rayleigh anomaly (RA) [119], which determines the maximum wavelength at which light can be diffracted parallel to the surface of the regular array, acting as a grating (as discussed in Chapter 3). For L = 450 nm, LP = 500 nm device, the RA is expected to occur at a wavelength of ca. 1650 nm, in good agreement with the results of Figure 4.4a. The near field distribution of the devices at their typical wavelength of maximal absorption is shown in Figure 4.4b-d for the same devices. All these three devices present hot spots with enhanced electric fields. The hot spots are distributed along the Au/Si interfaces close to the apex of the pyramids, but never at the apex position. This is a characteristic of the 4-facet devices and is related to their high symmetry. On the contrary, devices with a partial number of facets covered with gold with oblique gold deposition need to be explored because it is expected that they might display hot spots at the 3D apex of pyramidal structure.
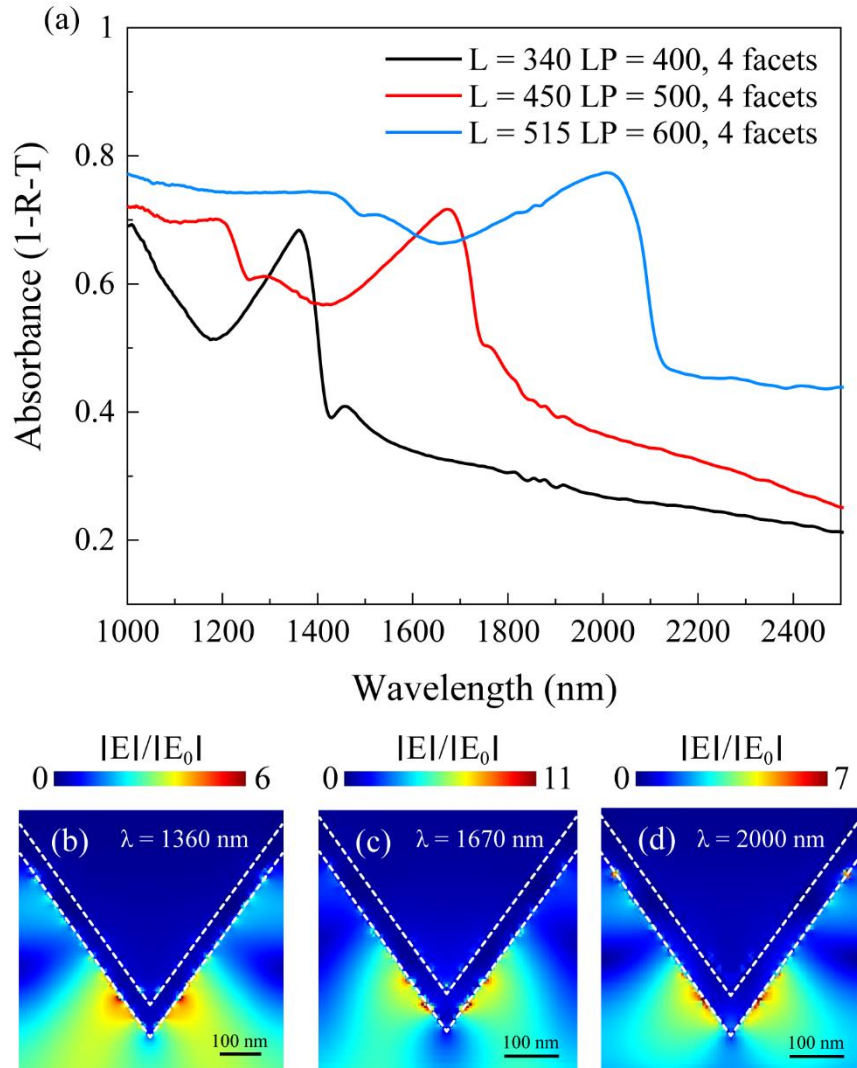
Figure 4.4: Far and near field properties of L = 340 nm, LP = 400 nm; L = 450 nm, LP = 500 nm and L = 515 nm, LP = 600 nm devices with deposited gold (50 nm) covering the 4 facets of pyramid. Measured absorbance (1-R-T) of three devices (a). Simulated near-field electric field distribution of devices with LP of 400, 500 and 600 nm at wavelengths of 1360 nm (b), 1670 nm (c) and 2000 nm (d) respectively.

In order to study the optical properties of the devices with oblique gold deposition, we characterized the reflectance of exactly the same devices with four facets studied before but with only 3 facets evaporated with gold. Figure 4.5a shows the reflectance of L = 340 nm, LP = 400 nm device with 3 and 4 facets covered with gold. For the 3 facets sample with 0° and 90° polarized incident light, both reflectance spectra exhibit a lower value in the wavelength range of 1500 to 1900 nm compared with the 4 facets device. A lower reflectance

indicates a stronger absorption (1-R) in this spectral region. For 0° polarized light irradiation, the absorption feature at around 1800 nm blue-shifts and increases in intensity as compared with the 90° polarization. Therefore, this absorption feature of the 3 facets sample can be tuned by changing the polarization of the incident light. In the wavelength range below 1500 nm, all the samples have a similar feature in the reflectance. For the L = 450 nm, LP = 500 nm device and L = 515 nm, LP = 600 nm device with 3 facets, they also display a similar trend as the L = 340 nm, LP = 400 nm device of having lower reflectance in longer wavelength range than its 4-facets counterpart, whereas no similarity of the reflectance in the shorter wavelength range is found between 3 and 4-facets devices (Figure 4.5b,c). Generally, in the long wavelength region, the 3-facets samples have lower reflectance than the 4-facets ones, a lower reflectance that corresponds to a higher absorbance (1-R). Moreover, the absorption features of the 3-facets samples can be tailored by variation of the polarization.
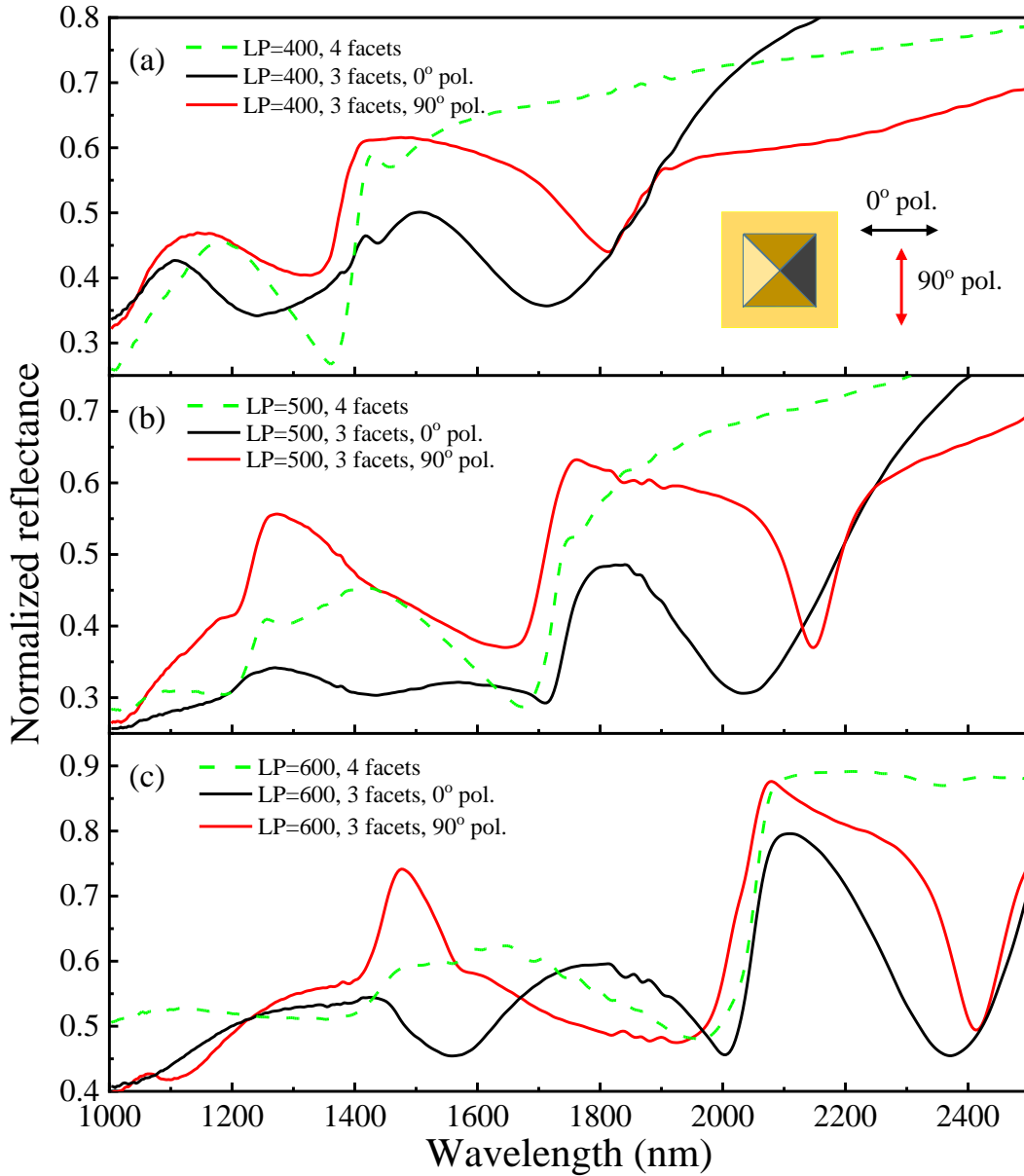
Figure 4.5: Normalized reflectance of devices with 4 or 3-facets covered with gold (50 nm deposition) measured with linearly polarized light. (a) Reflectance of L = 340 nm, LP = 400 nm device with 4 facets (green dash line) and 3 facets for 0° polarization (black solid line) and 90° polarization (red solid line). (b) Reflectance of L = 450 nm, LP = 500 nm device with 4 facets (green dash line) and 3 facets for 0° polarization (black solid line) and 90° polarization (red solid line). (c) Reflectance of L = 515 nm, LP = 600 nm device with 4 facets (green dash line) and 3 facets for 0° polarization (black solid line) and 90° polarization (red solid line).

As we discussed in Figure 4.4, for 4 facets samples with different LP, their specific absorption features vary with the lattice parameter LP of the array, which is connected to the phenomenon of the Rayleigh anomaly determined by LP and the refractive index of silicon. Figure 4.6a shows the reflectance of L = 450, LP = 500 nm device with 3 and 4 facets covered with gold. Both of these two devices have a feature with decreased reflection at ca. 1700 nm, which should be attributed to the RA phenomenon as we have explained that the RA is solely dependent on LP and refractive index of Si in this case. Another device with same LP of 500 nm but smaller pyramid size of L = 320 nm with 4 facets or 3 facets covered with gold shows the same RA feature at ca. 1700 nm (Figure 4.6b). Some variation of the RA feature between devices of 4 and 3 facets covered with gold might be related to the slight deviation of the L of pyramids that results in changes of LP that further influence the RA phenomenon. Moreover, devices of L = 450, LP = 500 nm and L = 240, LP = 500 nm with 3 facets covered by gold show sharp and low reflection features in the longer wavelength region at ca. 2030 nm and ca. 2150 nm, respectively, corresponding to high resonant absorbance considering zero transmittance. The high resonant absorption at longer wavelengths is ascribed to the 3-facets device with 90° polarized light irradiation breaking the symmetry of pyramidal Au/Si
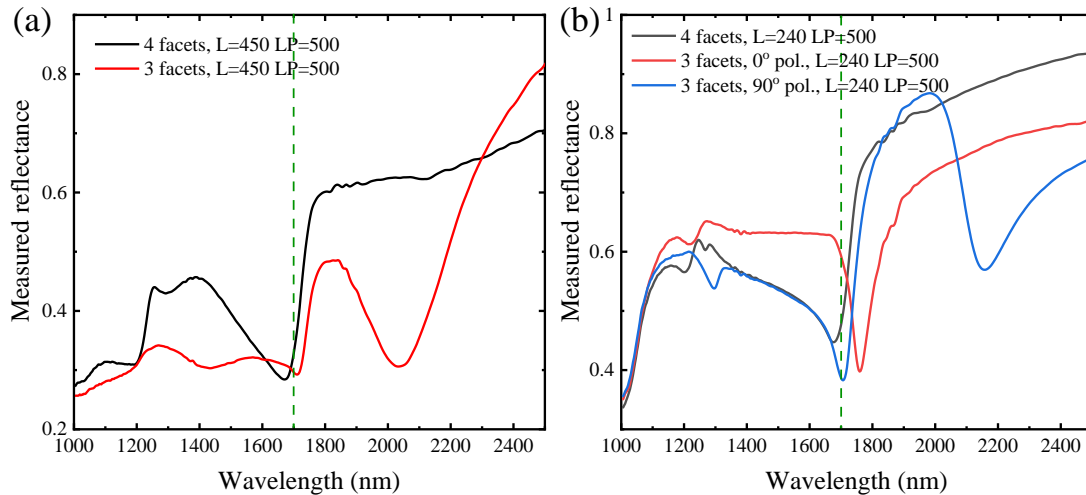

Figure 4.6: Measured reflectance of device covered with gold (50 nm deposition). Reflectance of L = 450 nm, LP = 500 nm device with gold covered on 3 and 4 facets of pyramid. (b) Reflectance of L = 320 nm, LP = 500 nm device with gold located on 3 (with 0° and 90° linearly polarized light irradiation) and 4 facets of pyramids.

structure to some extent, whereas this feature is not observed in symmetrical structures of the 4-facets device or 3-facets device with 0° polarization illumination.

As shown in Figure 4.7, we measured the polarization dependent reflectance and calculated the absorbance considering zero transmittance, A=1-R, of a sample of L = 320 nm, LP = 500 nm respective pyramid size and pitch with 4, 3 and 2 facets covered with gold. The aim of this study is to examine if the optical reflectance of the pyramids when illuminated with linearly polarized light is sensitive to the number of facets covered with gold. As expected, with the variation of the azimuthal angle of the polarization of the incident light, the zero-transmittance absorbance (1-R) of the device with 4 facets covered with gold is indifferent to the polarization due to the perfect square symmetry of the pyramidal array (Figure 4.7a). The azimuthal map exhibits the clear C_1 symmetry of the structure with respect to an axis passing through its apex. The maximum of 1-R is located at ca. 1650 nm, which corresponds to the dip in the reflectance due to the RA phenomenon (Figure 4.7d). Figure 4.7g shows the sketch of the 0° polarization on 4 facets device.

For the 3-facets sample (Figure 4.7b), on the contrary, the 1-R response of the device is very sensitive to the linearly polarized incident light. The azimuthal map shows now a clear C_2 symmetry: The maximum in 1-R associated with the RA alternates its position between ca. 1700 nm and ca. 1800 nm for 90° (270°) and 0° (180°, 360°) linear polarization. Interestingly, in the long wavelength region above the RA, a strong feature in 1-R is apparent at ca. 2200 nm, when irradiating with 90° (270°) polarized light but the feature is totally absent for the quadrature polarization (see Figure 4.7e). We point out that since this spectral feature occurs above the Rayleigh anomaly wavelength of λ_{RA}~1650 nm, it is related to the excitation of "localized" SPPs of the plasmonic structure. As shown in Figure 4.7h, the polarization propitiating the appearance of a plasmonic resonance at longer wavelengths is when the electric field points along the "long" axis of the 3 Au-covered facets of the pyramid.

For the devices with only 2 Au-covered facets, the 1-R maps exhibit again C_2 symmetry, repeating the pattern in the azimuthal angle every 180° but now starting at 45° (Figures 4.7c and 4.7f). Strikingly, for the 2-facets device the 1-R response displays strong resonance

features above the Rayleigh anomaly for both orthogonal linear polarizations but at different wavelengths. In fact, when irradiating with 45° and 225° the resonance peaks at ca. 1900 nm, whereas with 135° and 315° polarized light the strong 1-R feature is located at ca. 2200 nm. Figure 4.7i shows the sketch of the 45° and 135° polarization on 2 facets device. Generally speaking, the results on the polarization dependence indicate that the plasmonic resonances
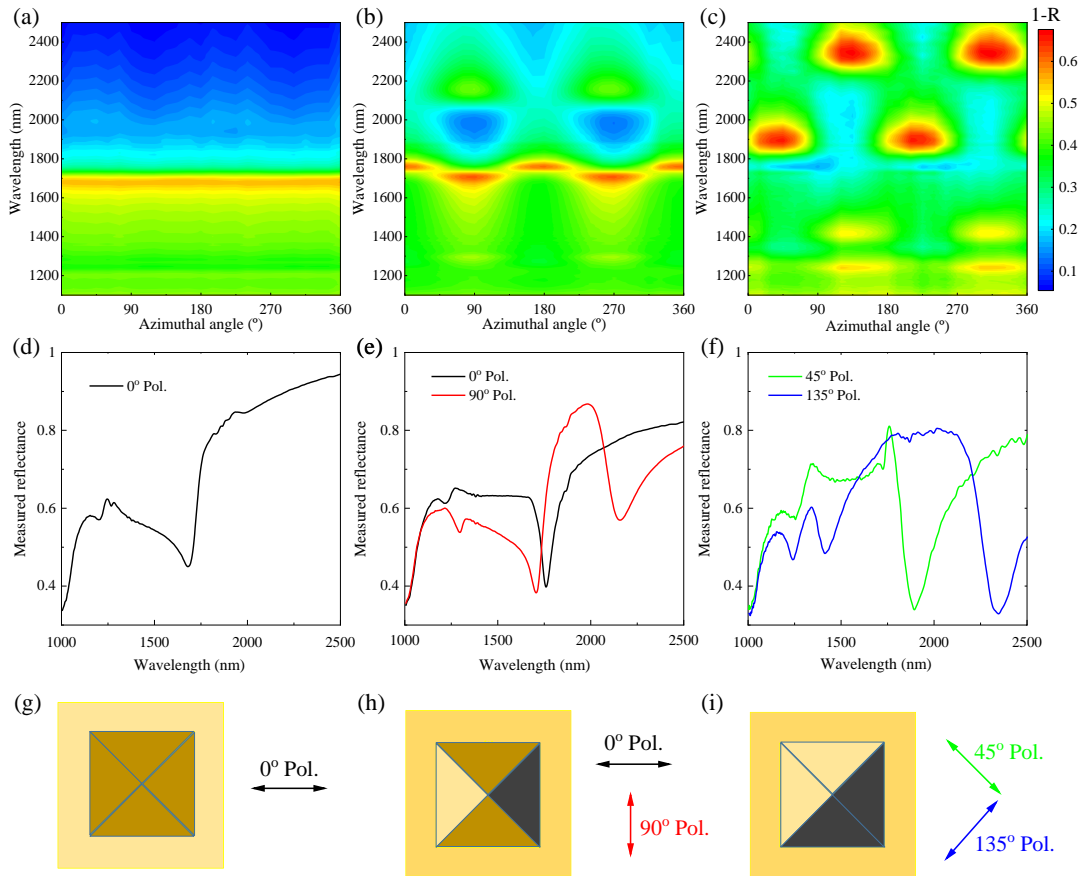

Figure 4.7: Polarization angle versus wavelength maps of the zero-transmittance absorption (1-R) for the L = 320, LP = 500 nm device in the wavelength range from 1000 to 2500 nm and azimuthal angles from 0° to 360° for (a) 4 facets, (b) 3 facets and (c) 2 facets covered with gold (50 nm deposition). (d) Measured reflectance of 4 facets sample under 0° polarized light irradiation. (e) Measured reflectance of the 3 facets device with irradiation of 0° and 90° polarized light. (f) Measured reflectance of 2 facets device with irradiation of 45° and 135° polarized light. (g), (h) and (i) The corresponding sketches of the polarization configurations for the 4, 3 and 2 facets samples, respectively.

can be tailored in their position and intensity not only by varying geometrical parameters but also employing a partial covering of the pyramid facets with the metal. Simultaneously, the near field distribution along the Au/Si interface is also expected to be tuned by the same means.

From previous study on the optical properties of devices with oblique gold deposition, we know that the device optical absorption at zero transmittance (1-R) can be enhanced in some wavelength ranges by tailoring the L and LP of the pyramidal arrays compared with normal gold deposition on device. Simultaneously, by tailoring the angle of linearly polarized incident light, 1-R can also be tuned in location and intensity. The breaking of the symmetry by partial covering of the number of facets of the pyramidal arrays will lead to a re-distribution of the near field, finally giving at the apex position a strongly enhanced electric field. Therefore, FDTD simulations (see details in Chapter 2) were used to study such electric field distribution in the case of the L = 450 nm, LP = 500 nm device with 3 and 4 facets covered with gold (Figure 4.8). The sample with 3 covered facets presents an overall higher E-field enhancement at the pyramid apex in the simulated wavelength range from 1000 to 2500 nm (Figure 4.8a). At 1270 nm and 2420 nm, the E-field enhancement of the 3 facets device is almost 25 times and 13 times larger than its counterpart of 4 facets, respectively. It is obvious that the pyramid apex is a hot spot for the 3 facets device (Figure 4.8b), whereas for the 4-facets sample the hot spots are located along the Au/Si interface but far away from the apex (Figure 4.8c). In the next chapter we will show that intense hot spots at the apex of the pyramid with electric fields pointing perpendicular to the metal surface are the ones permitting emission of hot electrons over the Schottky barrier into Si, which will result in a sizable photocurrent. Therefore, we expect the 3 facets devices to perform best in terms of hot electron emission.

(a)

(b)

(c)
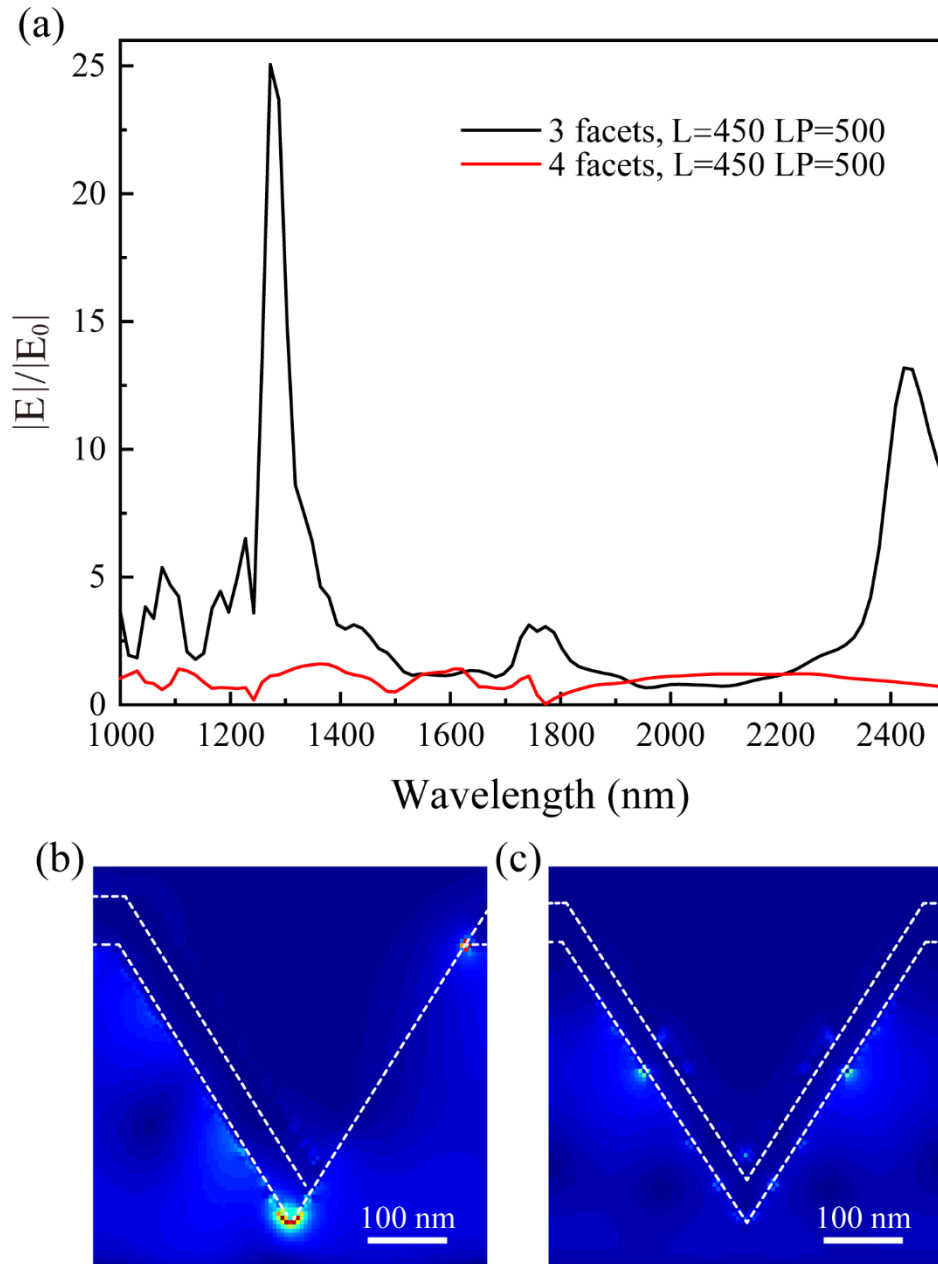
Figure 4.8: Near field properties of L = 450 nm, LP = 500 nm device. (a) Calculated electric field enhancement as a function of wavelength of the 3 and 4 facets device. Calculated electric field distribution of devices with (b) 3 and (c) 4-facets covered with gold (50 nm).

From the point of view of the possibility to attain hot-electron photocurrents via plasmon-resonance absorption of light, the inverted pyramid arrays with only 3 facets covered with gold are the most promising ones. In particular, these samples exhibit strong resonances at

longer wavelengths than the Rayleigh anomaly, which must correspond to localized plasmon modes, whose near field presents an intense hot spot at the pyramid apex. This effect is more pronounced, the smaller the pyramid, as we will show in the following by means of electrodynamic simulations. The FDTD method was used to simulate the far and near field of an inverted pyramid array with L = 240 nm, LP = 500 nm and 3 as well as 4 facets covered with a thinner gold film (30 nm). A comparison of the reflectance in the spectral range from 1000 to 2500 nm for both the 4 and 3 facets devices is shown in Figures 4.9a,b, respectively. As expected, for longer wavelengths than that of the Rayleigh anomaly at ca. 1700 nm, the 3-facets sample exhibits three strong resonances (dips in R), whereas the 4-facets device shows only one. Those features with low reflectance correspond to high absorption features and come from the resonant absorption of the plasmonic structure. The corresponding electric near field was simulated for both devices at these features with low reflectance. For the 4 covered facets pyramids, the hot spots are still distributed along the Au/Si interface but not at the apex of the pyramid (Figure 4.9c). For the 3 facets device, however, two positions with extremely intense electric fields were found at the very apex of the pyramid (red circle) and at the edge of the uncovered facet (blue circle), as shown in Figure 4.9d. These are the hot spots that might provide a 3D Schottky interface, which is ideal to improve the possibility of hot electron injection into the semiconductor [121]. We have further checked the intensity and direction of the E-field at these two hot spots of the 3 facets device. Figure 4.9e shows the E-field enhancement of two hot spots, i.e. the apex (blue line) and the edge (red). The maximum enhancement of the electromagnetic field at the edge hot spot is a factor of 37, whereas for the pyramid apex, the field enhancement reaches an extraordinary value of 112 for the most intense resonance. Another crucial point is that at these hot spots, the electric-field vectors are perpendicular to the metal surface, as shown in Figure 4.9f. This is a prerequisite for an efficient hot-electron emission into the semiconductor.
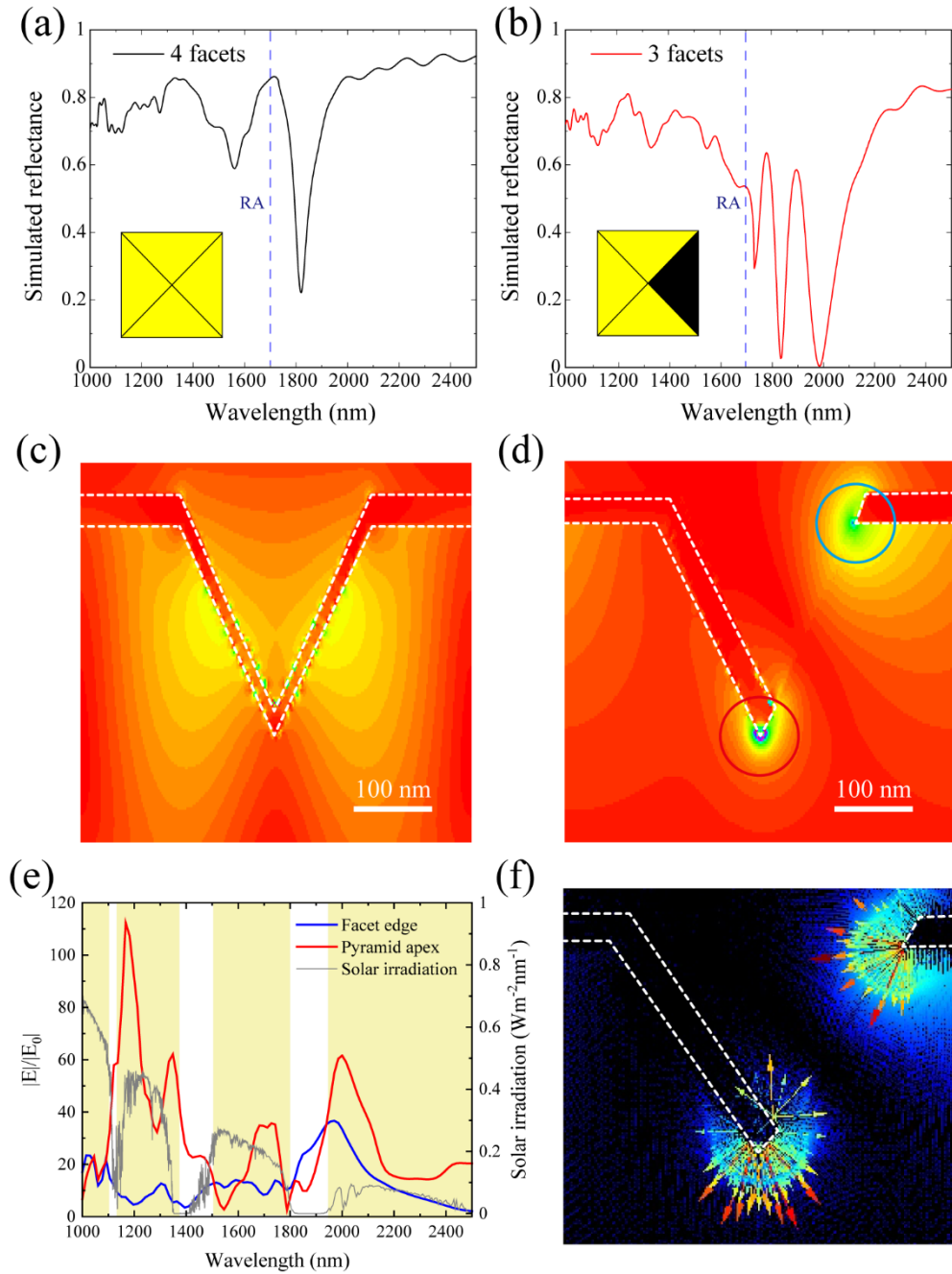
Figure 4.9: Simulated far and near field properties of L = 240 nm, LP = 500 nm device with gold (30 nm) covering 4 and 3 facets of the pyramids. Reflectance of device with (a) 4 facets and (b) 3 facets covered with gold. Contour plot of the electric field distribution (c) at 1820 nm and (d) at 1987 nm for the 4 and 3-facets sample, respectively. (e) Electric field enhancements at the pyramid apex (blue line) and uncovered facet edge (red line) as a function of wavelength. (f) Electric field vectors at both hot spots corresponding to the near field distribution shown in (d).

4.2 Conclusions

In this chapter, we have proposed a strategy for the fabrication of inverted Si pyramids with partial number of gold-covered facets and simulated and characterized their near and far field properties. The device of 3 facets covered with gold displays increased optical zero-transmittance absorption (1-R) above the wavelength region where the RA feature appears, compared to the device of 4 facets covered with gold. The 1-R maps of devices with 2 and 3 covered facets as a function of polarization azimuthal angle in the measured wavelength range both exhibit C_2 symmetry, whereas 4-facets device exhibits a C_1 symmetry. The polarization dependence indicates that the plasmonic resonances can be tailored in their position and intensity not only by varying geometrical parameters but also employing a partial covering of the pyramid facets with the gold. The electric field enhancement of 3-facets device at 1270 nm and 2420 nm is 25 times and 13 times larger than its counterpart device of 4-facets. A striking result is that the 3-facets device has its largest electric field concentrated at the pyramid apex on the Au/Si interface whereas the 4-facets counterpart device shows the electric field distributed along the Au/Si interface but never at the apex. The redistribution of the near field arises from the breaking of the symmetry of the pyramids by partial covering of only 3 facets with gold, giving the apex position a strongly enhanced electric field. The most pronounced effect is observed for the smaller sized pyramid whose electric field is concentrated at both the apex and the edge of the pyramids with high electric field enhancement. The crucial point is that at these hot spots, the electric-field vectors are perpendicular to the metal surface, as this is prerequisite for an efficient hot-electron emission into the semiconductor. Therefore, the designed inverted-Si-pyramids with partial number of gold-covered facets are expected to result in a sizeable photocurrent for optoelectronic applications.

Chapter 5

Photocurrent performance characterization of Au/Si devices

In metallic nanostructures, surface plasmon resonance (SPR) can be used to convert the absorbed photons into electrical energy via generating energetic hot electrons [22],[48],[58]. The collection of the electrical energy is done through contacting metallic nanostructures with semiconductors forming a Schottky diode which can be integrated into optoelectronic devices for several applications such as photodetectors [10],[20],[21],[122],[123], photovoltaic [47],[124],[125], etc. These new designed heterostructures provide a way to realize hot-carrier devices whose performance may boost that of conventional devices.

The performance of those heterostructure devices highly relies on the plasmon-hot electron conversion efficiency at the metal-semiconductor interface. Two of the distinct mechanisms that have been proposed for the study of plasmon-induced photoelectric conversion efficiency of metal/semiconductor devices are hot electron generation and plasmon-induced resonant energy transfer (PIRET). Conventionally, in a hot electron generation and injection process, light is absorbed by the plasmonic nanostructure generating surface plasmons which decay non-radiatively giving hot electrons. These hot electrons with energy usually smaller than the bandgap of the semiconductor but larger than the metal/semiconductor Schottky barrier height are injected from the metal into the semiconductor. In another scenario, PIRET takes place as follows: surface plasmon energy from the plasmonic resonance on the metallic nanostructure becomes transferred non-radiatively to the semiconductor through dipole-dipole interaction, locally generating electron-hole pairs in the semiconductor. Holes in the semiconductor move to the metal interface, acting as one electrode, while the electrons move away from it, towards the other electrode contacted with the semiconductor. The photocurrent is obtained by the collection of those electrons and holes on the electrodes through external circuit.

Despite remarkable progress has been made, the efficiency of devices based on plasmon-to-hot-electron conversion still remains below 1% [121]. It is reported that surface plasmons on

a Schottky diode-terminated tapered tip of nanoscale dimensions allows for a plasmon-to-hot-electron conversion efficiency of ~30% [121]. This enhanced performance of plasmon to hot electron structure consists of a grating and cone fabricated on an octagonal GaAs (as a semiconductor) pyramid covered with gold, the surface plasmon polaritons (SPPs) propagate and are concentrated adiabatically at the apex of the tapered plasmonic waveguides, which can guide and localize optical energy with acceptable losses. Therefore, by appropriately tuned structure geometry, it is possible to efficiently promote specific SPP damping channels [126]–[130], moving from radiative losses [131],[132] to the generation of hot electrons as a primary decay channel. For our designed devices of inverted Si pyramid arrays with oblique gold deposition which perform enhanced resonant absorption and intense hot spots at the apex of the pyramids, it could be expected to achieve a high photocurrent responsivity performance.

In this chapter, we characterized the electrical properties of the as-fabricated Au/Si devices textured with inverted pyramids and analyzed the involved mechanisms for the enhanced photocurrent generation in the measured spectral region. The oblique gold deposition results in the broken-symmetry of Au/Si pyramids, and an enhanced resonant absorption feature is observed in the longer wavelength region. The electric field also re-distributes to the apex of pyramids with electric-field vectors perpendicular to the metal surface. Those properties are critical for the plasmon to hot-electron conversion. Both the hot electron generation, injection and PIRET mechanisms work simultaneously below and above the Si bandgap to achieve a desired photocurrent responsivity in the measured spectral range.

5.1 Results and discussion

The sketch of all the electrical measurements of devices is shown in Figure 5.1. Light is illuminated from back-side of the device. On the back-side of the device, there are indium contacts soldered on the Si substrate as the rear electrode forming an ohmic contact with the Si. On the front-side, the gold film not only acts as plasmonic absorber, but also as front electrode. The front-side gold film and back-side indium contacts form the external circuit for the collection of photocurrent.
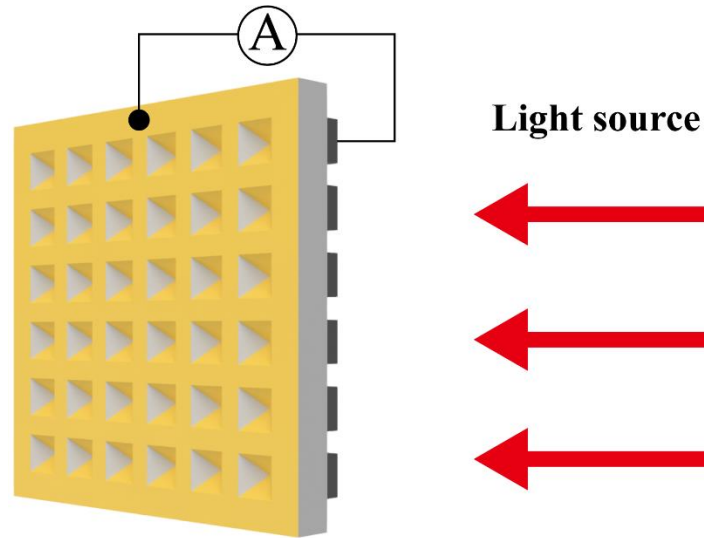
Figure 5.1: Sketch of the electric characterization of devices. Light is illuminating from the back-side of the device. The external circuit is connected by the front-side Au film electrode and the back-side indium contact electrode.

To verify whether the Schottky junction was properly formed at the Au/Si interface through the proposed fabrication process, current-voltage (I-V) characteristic curves of the heterojunction devices were measured in dark and under illumination with a solar simulator (AM1.5G) from the back-side of the device. The resulting I-V curves of a 3-facets device with L = 515 nm and LP = 600 nm exhibiting rectifying characteristic are shown in Figure 5.2. This demonstrates that a Schottky barrier was formed at the Au/Si interface. A very high photocurrent of 3.8 mA was obtained under illumination compared with a low dark current of 0.03 mA at -1 V of reverse bias. Under solar irradiation, the open circuit voltage (Voc) of the device reaches 0.23 V, whereas the Voc under dark condition is 0 V. We will show that in the NIR spectral range there is a photocurrent which can be ascribed to hot electrons generated from surface plasmons decay, then injected into the semiconductor over the Au/Si Schottky barrier.
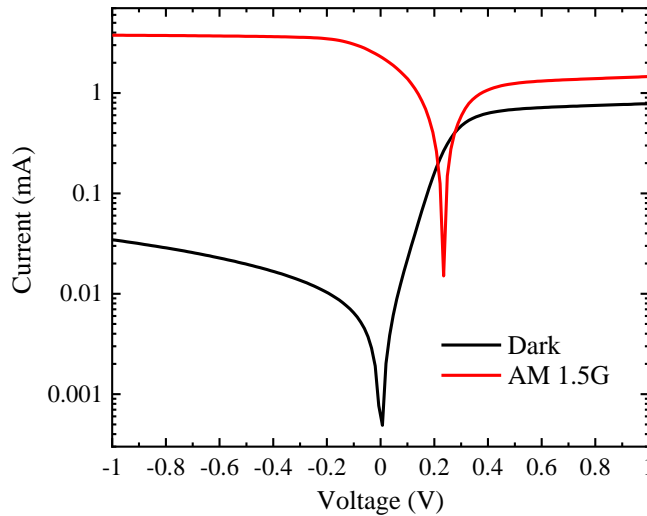
Figure 5.2: Current-voltage (I-V) characterization of L = 515 nm, LP = 600 nm device with 3 facets of the pyramids covered with gold (50 nm deposition).

The measured responsivity spectra of the device in and out of the patterned region are plotted in Figure 5.3. The photocurrent measurements were performed at zero external bias. The measurement on the flat surface of the device hardly shows any photo-response beyond a wavelength of 1200 nm, which approximately corresponds to the Si band edge. The incorporation of structured pyramidal arrays to the system allows for the absorption of sub-bandgap photons and the generation of hot electrons. As shown in Figure 5.3a, compared with the reference curve obtained on the flat surface of Si substrate covered with gold, a significant photo-responsivity enhancement is observed on the gold covered inverted silicon pyramidal arrays. This Au/Si Schottky device has a broad photo-responsivity spectrum across a wavelength range of 1200–1700 nm. The inset shows the photo-response in the whole measured wavelength range from 1000 to 1700 nm. In the region above the bandgap of silicon, there are features with very high photo-response both found in and out the pattern region, which can be attributed to the response of silicon via PIRET. Figure 5.3b shows the current enhancement of the device in the measured wavelength range, which is the ratio of currents on the pattern to that on the flat surface, representing the ability of photocurrent generation on the textured surface of the device. From the result, the maximum current enhancement of 27 is observed at 1350 nm that is beyond the Si bandgap edge and an overall value lager than 10 in the entire measured wavelength range. It indicates that the photocurrent generation of the device mainly arises from the textured pyramid arrays on the device.
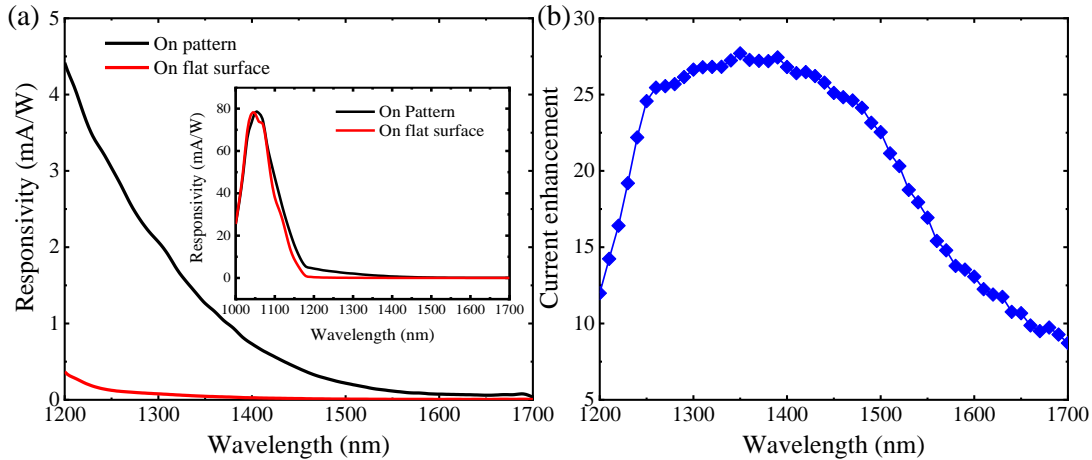
Figure 5.3: (a) Responsivity in the pattern of L = 515 nm, LP = 600 nm device with 3 facets of pyramids covered with 50 nm Au and out of the pattern with flat area covered with 50 nm Au in a wavelength range of 1200-1700 nm. Inset: Responsivity of the device in the whole measured wavelength ranging from 1000 to 1700 nm. (b) Current enhancement factor in the pattern in relation to out of the pattern reference (flat surface).

To verify the homogeneity of the generated photocurrents, we have measured the responsivity on a large area of the textured surface of a L = 515 nm, LP = 600 nm device with 3 facets covered with 50 nm of Au. We performed the responsivity mapping of the device at wavelengths below and above that of the Si bandgap edge, namely at 1060 and 1300 nm, respectively. Figure 5.4a shows the back-side of the device, the cyan rectangle is the scanned area. The electrical measurements were taken with back-side illumination. Figure 5.4b shows the front-side of the device, the cyan rectangle is the scanned area and within the red dotted rectangle is the patterned region. Then, the responsivity mapping of the device in the cyan-marked area was collected. In Figure 5.4c, the blue area with quite high intensity of responsivity is the region corresponding to the whole scanned Si substrate, which is covered with gold. It is clear that this gold covered region (except for the yellow circular and triangular areas which are covered with a contact or without gold, respectively) with and without pattern shows the same equivalent responsivity for photon energies above the Si bandgap, where the responsivity mainly comes from the Si (PIRET). For longer wavelengths than that of the Si bandgap at 1150 nm, in this case for 1300 nm light irradiation, there is a clear difference in responsivity between the patterned and the flat area (Figures 5.4d and

5.4e). In fact, only the patterned region has a photo-response at this wavelength. In the patterned area, the photo-response is homogenous with a maximum responsivity of 2.1 mA/W. This high photo-response obtained in the whole pattern of the pyramidal array in the transparency region of Si can only stem from hot-electron generation by internal photoemission processes over the Schottky barrier at the Au/Si interface.
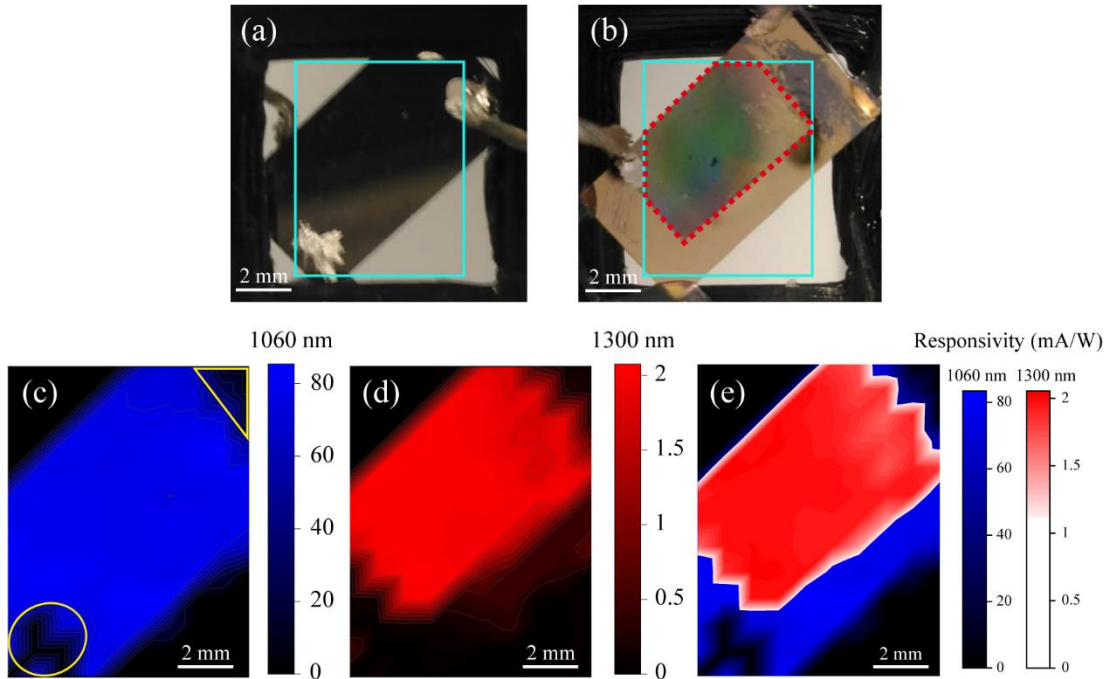

Figure 5.4: Responsivity of the L = 515 nm, LP = 600 nm device with 3 pyramid facets covered with gold (50 nm). Optical images of (a) the device back-side and (b) front-side with the gold covered pattern. Responsivity map in mA/W of device when illuminating at 1060 nm (c) and 1300 nm (d), respectively. (e) Responsivity overlay of the maps in (c) and (d). There is no gold in the top yellow triangular region and there is an indium contact in the bottom yellow circle.

We have obtained high photo-response on the L = 515 nm, LP = 600 nm device, but the responsivity is featureless (just monotonically decreasing function for longer wavelengths). In order to be able to assign this response to hot electrons with full confidence, we explore the possibility that devices with different L and LP would exhibit features in the photo-response in the wavelength region below Si bandgap energy. Results of the electrical photo-response for devices with 3 facets covered with 50 nm gold but different geometrical

parameters are shown in Figure 5.5. For the L = 210 nm, LP = 400 nm device, the responsivity is the lowest of all the samples. In the region above 1200 nm, it has an obvious photo-response feature at around 1300 nm with an intensity reaching 0.6 mA/W. For the L = 320 nm, LP = 500 nm device, the response exhibits a peak-like feature also near 1300 nm with a high intensity of 2.9 mA/W. The L = 385 nm, LP = 600 nm device, however, displays a double peak response with maxima at ca. 1300 nm and 1420 nm and a high intensity of ca. 3.4 mA/W and 2.6 mA/W, respectively. All these devices show remarkable responsivity in the wavelength range of transparency of Si, obviously, can only be attributed to the plasmon-induced hot electron generation by the internal photoemission from gold to Si.

Figure 5.5: Parameter dependent responsivity of L = 210 nm, LP = 400 nm; L = 320 nm, LP = 500 nm and L = 385 nm, LP = 600 nm devices with 3 facets covered with 50 nm gold.

Furthermore, we also studied the photo-response of pyramid arrays with all the facets covered with gold. As shown in Figure 5.6, all the devices with 4 facets covered with gold exhibit different photo-response features as the geometrical parameters L and LP change. The maximal responsivity among these 3 samples is less than 0.7 mA/W obtained at ca. 1400 nm, which is 5 times smaller than the highest responsivity of 3.4 mA/W at 1300 nm obtained with the 3-facets device, shown in Figure 5.5. The high responsivity achieved on the devices with 3 facets covered with gold can be attributed to the fact that oblique gold deposition breaks

the symmetry of the Au/Si pyramid structure, leading to higher intensity enhancements and that the E-field redistributes at the apexes of the pyramids. Under these conditions, hot electrons have a larger probability to go over the Schottky barrier at the Au/Si interface, being injected into the semiconductor and collected as a photocurrent. In contrast, for the 4-facets devices, the pyramid apex is never a hot spot, as forbidden by symmetry.

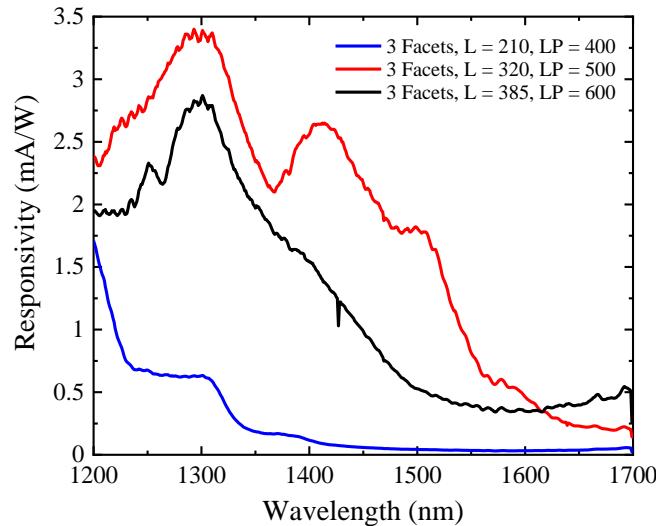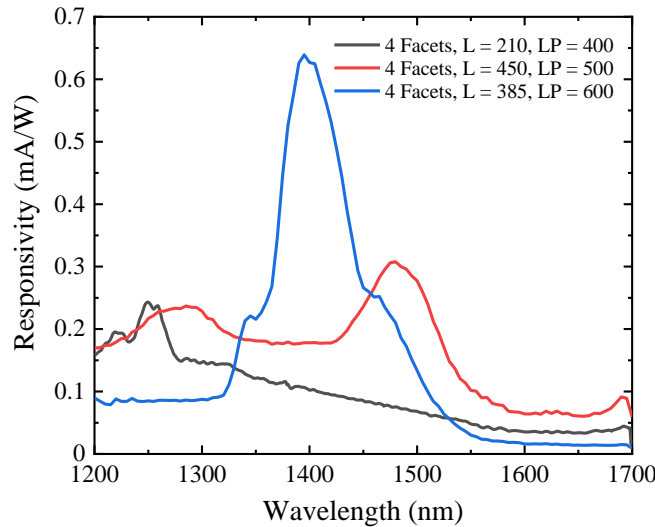**Figure 5.6:** Lattice parameter and pyramid size dependent responsivity of L = 210 nm, LP = 400 nm; L = 450 nm, LP = 500 nm and L = 385 nm, LP = 600 nm devices with 4 facets covered with 50 nm gold.

Moreover, in order to verify the photo-response is not only detectable on a single point but on a large area in the pattern of device, we performed a photocurrent mapping using a small-size pyramid array in the wavelength range of transparency of Si. Specifically, we performed responsivity mapping on the L = 210 nm, LP = 400 nm device with 3 facets covered with 50 nm gold. Figure 5.7a displays the optical images of the device (front side) with the pattern inside the white dash square, which indicates the scanned area. The mapping was carried out from the back-side of the device. When illuminating at 1000 nm and 1100 nm, i.e. above the Si band gap, all the scanned area including the center pattern and the flat gold-covered surface at the border shows a response with maximum intensity up to a value of 66 mA/W at the patterned region (Figures 5.7b and 5.7c). The area where the responsivity goes to zero (blue color) corresponds to the place without gold coverage (especially the bottom-right area in the

scanned region of Figure 5.7a). This signal, which corresponds mainly to photocurrents generated by the PIRET effect in the Si, is strongly enhanced by the presence of the pyramidal pattern. When illuminating at 1300 nm, that means below the gap energy of Si, the responsivity signal is detectable exclusively in the patterned region (Figure 5.7d), indicating once more that in the transparency region of Si only plasmon-induced hot electrons are able to generate a photocurrent. Generally, by tailoring L and LP of the gold covered 3-facet devices one can achieve remarkable photocurrent generation in the NIR spectral region.
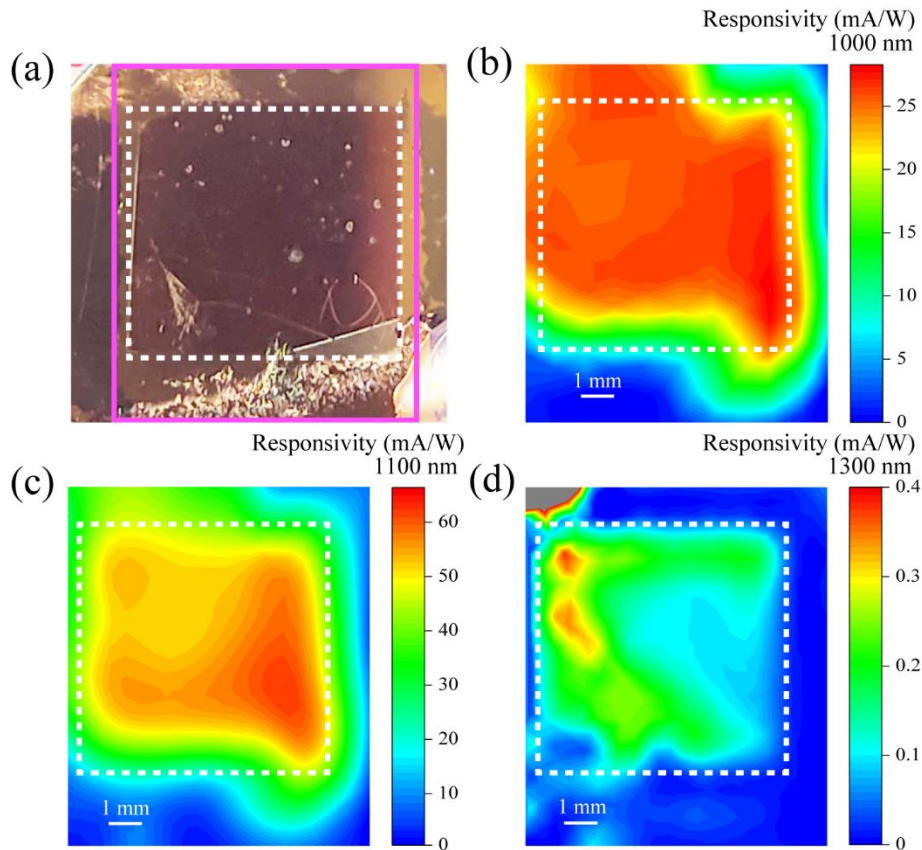
Figure 5.7: Responsivity of the L = 210 nm, LP = 400 nm device with 3 facets covered with gold (50 nm). Optical images of the device front-side, where the pattern is clearly observed. Responsivity map of device when light is illuminated from back-side of substrate at 1000 nm (b), 1100 nm (c) and 1300 nm (d) respectively. The solid pink rectangle is the scanned area; white dash square is the pattern area. The color scales are mA/W.

The polarization dependence of the L = 320 nm, LP = 500 nm device with 3 facets of pyramid covered with 50 nm gold is studied to demonstrate that the photocurrents have the same polarization dependence as the plasmon resonance features of the pyramid arrays, as we have shown in Figure 4.7 of the previous chapter. Figure 5.8a illustrates the sketch of measuring with polarized incident light. As shown in Figure 5.8b, when the linear polarization of the incident light is rotated in the plane of the sample surface, the photocurrents in the spectral region of hot-electron generation also vary in intensity in a periodic way, having special features of high photocurrent at ca. 1300 and 1470 nm. The polarization dependent photocurrent of the device at the two typical wavelengths of 1300 and 1470 nm is plotted in Figure 5.8c. Under 1300 nm light irradiation, the maximal photocurrent reaches up to 1.9 μA.
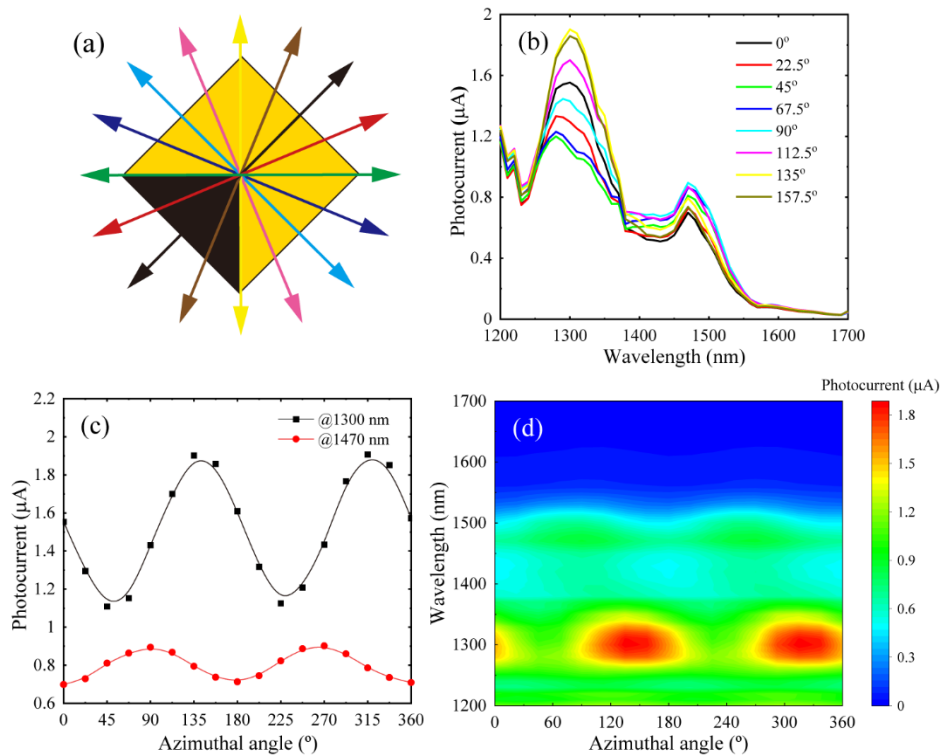
Figure 5.8: Electrical properties of L = 320 nm, LP = 500 nm device with 3 facets covered with 50 nm gold. (a) Sketch of the polarized incident light on the device. (b) Polarization angle dependent photocurrent in the wavelength range from 1200 to 1700 nm. (c) Polarization angle dependent photocurrent at a wavelength of 1300 and 1470 nm. (d) Photocurrent contour graph of device as the variation of polarization angle in the wavelength of 1200-1700 nm.

When irradiating with light in longer wavelength at 1470 nm, the maximal photocurrent decreases to 0.9 µA. With variation of the polarization azimuthal angle, the photocurrent of the device also oscillates exactly in the same way as the absorbance (see Figure 5.8d and Figure 4.7 of the previous chapter for comparison).

5.2 Conclusions

In this chapter, we have characterized the photoelectrical properties of Au/Si inverted-pyramid devices with different number of facets covered with gold and demonstrated the plasmon-resonance aided generation of substantial photocurrents for illumination with NIR light. For photons with energies close but above the fundamental band gap of Si, i.e. for wavelengths shorter than 1200 nm, we have achieved remarkably high responsivities in the range of 0.1 A/W, which are produced through the so-called PIRET mechanism. In this particular case, electron-hole pairs are generated in the Si very close to the metal/semiconductor interface via an energy transfer process from plasmon resonances excited with the incident photons rather than by conventional photovoltaic effect. More importantly, below the Si bandgap, that is in its transparency range, high responsivities up to 3.5 mA/W were also attained, which are ascribed to the plasmon-induced generation of hot electrons by internal photoemission from the gold into the Si. The hot electron photocurrents present peak-like features in close coincidence with the plasmon resonances observed in the optical properties of the pyramidal arrays. Also in agreement with the better near-field performance (presence of intense hot spots) of 3-facet devices, the magnitude of the hot-electron photocurrents is up to five times larger for these devices as compared with the fully covered pyramids (4-facets). In consequence, the photo-response of the devices can be tailored by design, adjusting the geometrical parameters of the pyramid arrays or the number of gold covered facets. Moreover, a NIR photo-response is exclusively obtained inside the region with the pattern of inverted pyramids, not in the flat gold regions, being also fairly homogeneous across the whole pattern. Finally and as compelling evidence that the photocurrents measured in the NIR spectral region are indisputably due to hot-electron generation, we studied the dependence of the responsivity on the polarization direction of the incident light for the case of a 3-facets device. Strikingly, the photocurrent maps as a function

of polarization azimuthal angle in the wavelength range of 1200-1700 nm exhibit exactly the same C_2 symmetry as the absorbance maps, displayed in the previous chapter.

Chapter 6

Inverted-pyramid array-based metal/organic-semiconductor architectures

Photocurrent generation has been already demonstrated in classic Au/Si Schottky devices based on nanoscale inverted pyramid arrays. The obtained photocurrent is due to the excitation of surface plasmons on the gold nanostructure by non-radiative decays through band transitions and transfers of the energy to the "hot electrons" in the conduction band of the metal. Due to the fact that a Schottky junction exists between gold and Si, hot electrons with enough energy (but smaller than the Si bandgap) can cross the Schottky barrier and be injected into the semiconductor. This process is known as hot electron injection process. Holes left behind in the metal and electrons in the semiconductor are collected by an external circuit. In order to verify if the hot electron injection concept is transferable to other metal/semiconductor structures for photocurrent generation, a flexible and soft organic semiconductor is used in this work with gold material to assemble a device that might be able to yield a hot-electron photocurrent.

The n-type organic polymer N2200 is used in this work as semiconductor material. We selected this material for the following reasons: first, N2200 is an n-type organic semiconductor that is widely used in organic solar cells, being air stable, low cost and having high electron mobility [133]–[135]. Second, N2200 is a narrow bandgap (1.47 eV) semiconductor with an absorption edge in the NIR region (844 nm) [135]. Third, N2200 film is elastic, which renders the possibility of large-scale fabrication of the device in a simple process of nano-imprint compared with inorganic Si based device whose processing highly relays on more costly lithography techniques.

Having the concept in mind, in this work, we fabricated the inverted-pyramid array-based metal/organic-semiconductor architectures, characterized their near/far field properties and

the electrical performance. The numerical simulations also have been carried out for the verification of their optical properties.

6.1 Results and discussion

6.1.1 Device Fabrication

Poly{[N,N0-bis(2-octyldodecyl)-naphthalene-1,4,5,8-bis(dicarboximide)-2,6-diyl]-alt-5,5'-(2,20-bithiophene)} (known as Polyera ActivInk N2200, also named as P(NDI2OD-T2)) is an n-type organic semiconductor material, whose chemical structure is shown in Figure 6.1a. For assembling the inverted pyramids-based Au/N2200 structure, the N2200 polymer is dispersed in chlorobenzene, spin-coated into thin film for subsequent nano-texturization. Figure 6.1b (black line) shows the measured absorbance of a 400 nm-thick N2200 film. It reveals that the N2200 film has relative high absorption in the visible range with maximal absorbance located at 700 nm. Below the N2200 bandgap, the absorption goes to zero. Comparing with the maximum absorbance located at 700 nm, the photoluminescence (PL) of N2200 thin film redshifts with maximum at 860 nm [133], as shown in Figure 6.1b (red line).
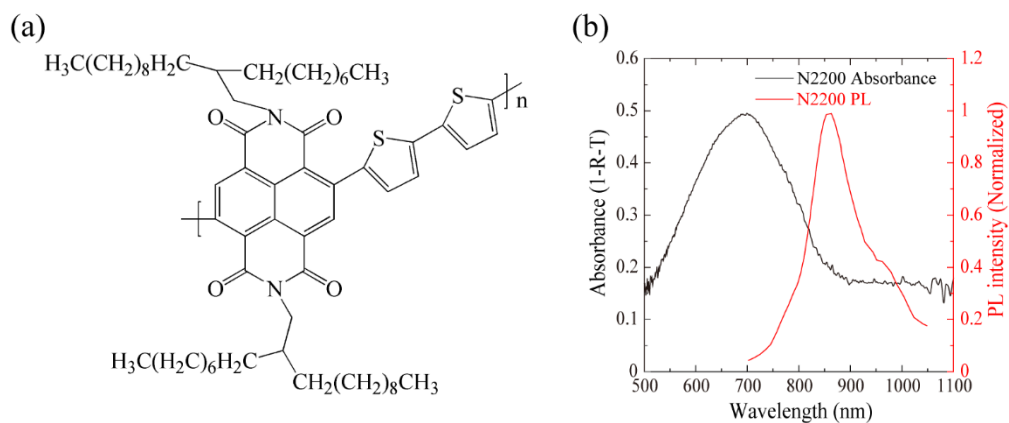

Figure 6.1: (a) Molecular structure of poly{[N, N′-bis(2-octyldodecyl)-naphthalene-1,4,5,8-bis(dicarboximide)-2,6-diyl]-alt-5,5′-(2,2′-bithiophene)} (N2200) polymer. (b) Measured absorbance (1-R-T) of the 400 nm-thick N2200 film (black line); photoluminescence spectrum of N2200 film (red line) [133].

The general sketch of the Au/organic-semiconductor device is shown in Figure 6.2a. This structure is assembled by a soft NIL technique, a layer-to-layer structure which from bottom to top is formed by ITO (Indium-doped tin oxide) on glass substrate, N2200 thin layer, MoO_3 thin layer and gold film. The inverted pyramid arrays are imprinted on those layers. Figure 6.2b shows the corresponding cross-section sketch of the structure depicted in Figure 6.2a. The metal/semiconductor structure is specifically designed for photocurrent generation when the device is illuminated from the glass side. Figure 6.2c gives the band diagram of materials used in the device. The MoO_3 thin film inserted in the devices does not act as a barrier but as a hole transport layer (HTL) with high hole mobility, high transmittance and good stability. Moreover, it is also acting as a layer that can effectively avoid short-circuits between the gold film and ITO.
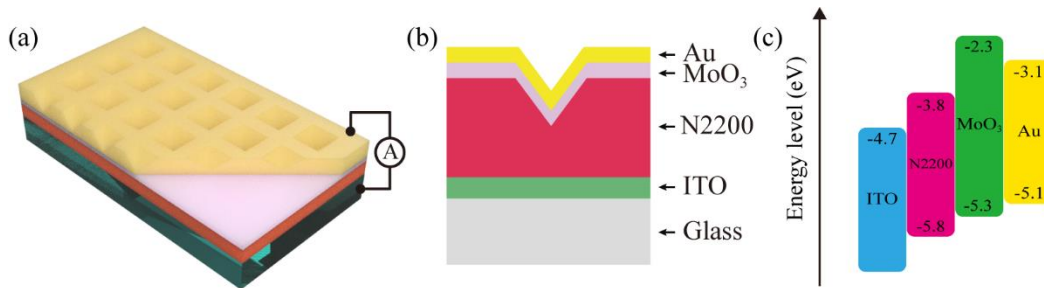
Figure 6.2: (a) 3D sketch of the fabricated Au/N2200 inverted pyramid arrays device for photocurrent generation. (b) Corresponding cross-section of device shown in (a). (c) Band alignment diagram of the materials used in the device.

Due to the low refractive index and high transmittance of MoO_3 film, we expect that the MoO_3 thin film in this structure would not have much effect on its optical absorption. To confirm our point, we performed FDTD simulations of the absorption of the device with and without MoO_3 thin layer. The parameters of the inverted pyramid arrays on N2200 are L = 470 nm and LP = 590 nm as the PDMS stamp used for imprinting the pattern on N2200 polymer is made from a Si master with the same inverted pyramid parameters (L = 470 nm and LP = 590 nm). As shown in Figure 6.3 for light incident from ITO glass, with or without MoO_3 thin layer inserted, the absorption is almost the same, showing only slight variations in magnitude. Therefore, we think that MoO_3 thin film does not have side effects on the light

trapping properties. The discussed devices hereafter were fabricated with a 5 nm MoO_3 thin film inserted between the polymer and gold layers.

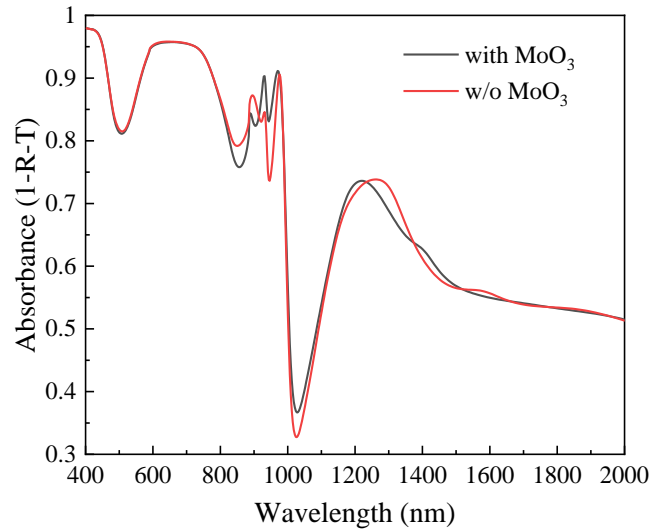**Figure 6.3:** Simulated absorbance (1-R-T) of inverted pyramids (L = 470 nm, LP = 590 nm) based Au/N2200 structure with and without 5 nm-thick MoO_3 film inserted. Light is incident from ITO glass side. Au film: 30 nm. N2200 film: 400 nm.

The fabrication process of the optoelectronic device can be separated into two main parts: preparation of the metal and oxide layer covered hybrid PDMS stamp with pre-designed inverted-pyramid arrays and transfer of the films with pattern onto the semiconductor. For the preparation of the imprinting stamp (Figure 6.4 top row): first, inverted pyramid arrays are patterned on the 1.5 cm x 1.5 cm Si wafer piece with a 1 cm^2 size area of the pattern as explained in Chapter 2. Then, a negative hard PDMS stamp with soft PDMS backbone replicating the inverted pyramids pattern from the as-prepared Si wafer (see details in Chapter 2) was used to produce a printing stamp with positive features. Next, it follows thermal deposition of 30 nm-thick gold film on the stamp with positive features at a deposition rate of 6×10^{-2} nm s^{-1} under vacuum pressure below 1×10^{-6} mbar. Before this step, an anti-sticking layer of silane was evaporated on the PDMS stamp for an easier transfer of the subsequently deposited layers. Finally, we proceed with the thermal deposition of 5 nm-thick MoO_3 film on the gold film at a deposition rate of 5×10^{-2} nm s^{-1} under vacuum pressure below 1×10^{-6} mbar. For the transfer of the as-deposited Au/MoO_3 films onto the organic

semiconductor (Figure 6.4 bottom row) the sequence is as follows: first, 8 mg/ml N2200 polymer solution in chlorobenzene is prepared, then the N2200 solution is spin-coated on a clean ITO glass at 600 rpm for 15 s. When the spin-coating process stops, the sample is removed from spin-coater quickly (before the solvent evaporates) and imprinted with the as-prepared PDMS stamp with MoO_3 and gold on semi-wet N2200 film. The stamp is left undisturbed until the solvent evaporates to finally peel off the PDMS stamp gently from the N2200 film. In this way (called wet nano-embossing), we obtain in a single step the desired MoO_3 and gold covered inverted pyramid array on N2200 film. The photocurrent collection is achieved by the connection of gold film electrode and conductive ITO electrode. Following this strategy, we fabricated a series of devices operating in the same spectral range with different structural parameters such as the pyramid side length (L) and lattice parameter (LP). A summary of all the geometrical parameters of the fabricated structures is presented in Table 6.1.
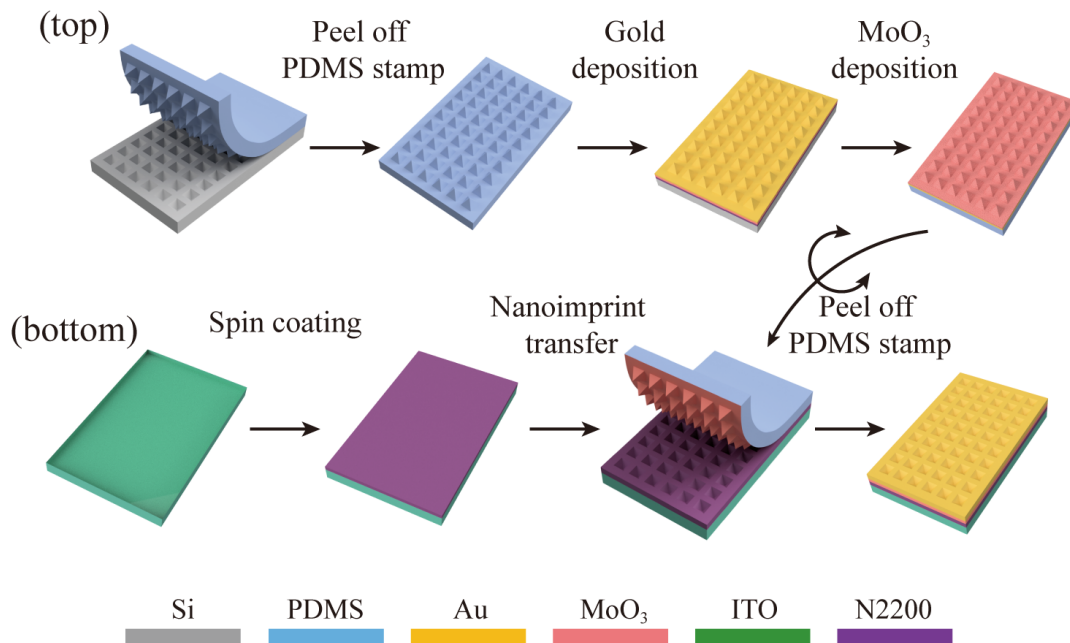

Figure 6.4: Sketch of the organic semiconductor Au/N2200 inverted pyramids device fabrication processes. Processing steps of the hybrid PDMS stamp to be imprinted (top). Processing steps of imprinting and transfer of gold and MoO_3 films (bottom).

Table 6.1: Geometrical parameter sizes of the fabricated structures: pyramid side length (L), lattice parameter (LP), pyramid height (h), gold film thickness (t_1), MoO_3 film thickness (t_2), and N2200 polymer thickness (t_3).

L (nm)	LP (nm)	h (nm)	t_1 (nm)	t_2 (nm)	t_3 (nm)
280	400	198	30	5	400
340	500	240	30	5	400
480	600	339	30	5	400

The photography of hybrid soft/hard PDMS stamp with positive feature of LP = 600 nm upright pyramid arrays covered with MoO_3 and gold films is shown in Figure 6.5a. The intense color observed with naked eyes is from the diffraction of the periodic nanostructure. Different periodicities will show different colors associated with different diffraction order. The corresponding large magnification scanning electron micrograph (SEM) image is shown in Figure 6.5b, where the patterns on PDMS stamp with bright areas corresponding to the upright pyramids and the dark regions between each unit is the flat gold film. The difference in brightness between pyramids with different pitches is related with height, usually higher features are brighter compared with lower ones. An example of a large area of high quality periodic upright pyramid arrays on PDMS stamp with regular shape is shown in Figure 6.5c.
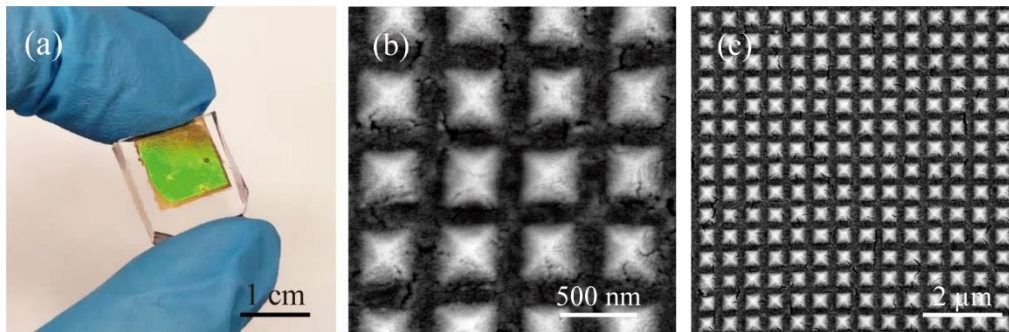

Figure 6.5: Morphology of the upright pyramid arrays covered with MoO_3 (t_2 = 5 nm) and gold (t_1 = 30 nm) films on PDMS stamp. (a) Optical image of the hybrid PDMS stamp covered with MoO_3 and gold film. High (b) and low (c) resolution SEM image of the upright pyramid arrays on PDMS stamp.

After fabricating the MoO_3 and gold films covered hybrid PDMS stamps, these films with different features (L, LP) were transferred onto the N2200 polymer that is pre-spin-coated on ITO glass. Figure 6.6a shows the final device with transferred LP = 600 nm inverted pyramid arrays covered with 5 nm MoO_3 and 30 nm gold films; the center square area with red color is the patterned region, whereas outside the patterned region the blue color is the flat N2200 film. SEM images of the fabricated 3D plasmonic Au/N2200 device with inverted pyramid arrays of LP = 400 nm, LP = 500 nm and LP = 600 nm are shown in Figs. 6b to 6d, respectively. The imprinted pattern shows regular inverse features with highly regular periodicity. It cannot be avoided that there are cracks on gold films, because the flexibility of hybrid PDMS stamp allows it to bend during the film transfer process.
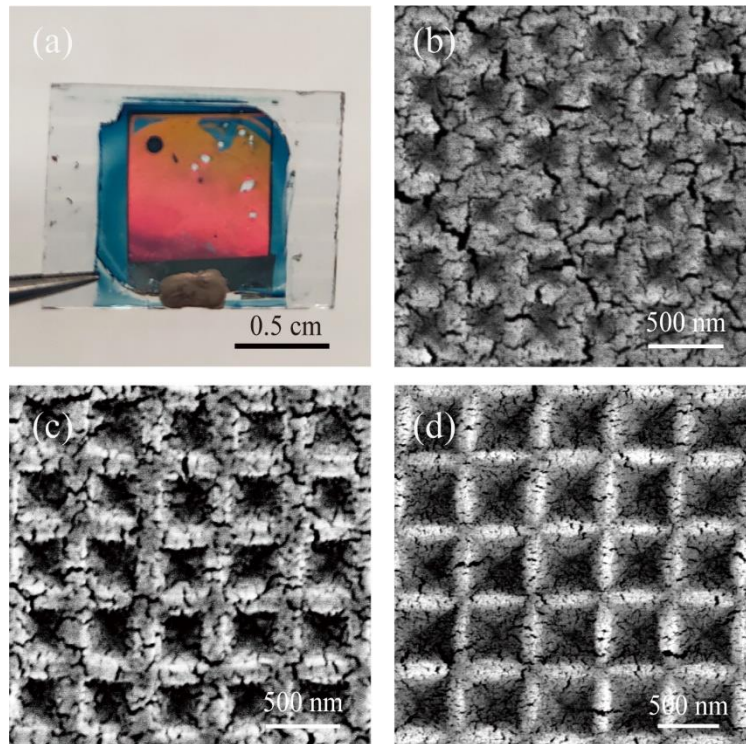

Figure 6.6: Morphology of the gold-N2200 structure with patterned inverted pyramid arrays. (a) Optical image of inverted pyramid arrays on N2200 film (t_3 = 400 nm) covered with MoO_3 (t_2 = 5 nm) and gold film (t_1 = 30 nm). SEM images of the upright pyramid arrays with LP of 400 nm (a), 500 nm (b) and 600 nm (c) on N2200 polymer (t_3 = 400 nm).

6.1.2 Proof of concept device for photocurrent generation

After the fabrication processes, we first investigate the influence of the geometrical parameters of optoelectronic devices on their optical properties. The samples were characterized in reflection (R) and transmission (T) under normal incidence using a Fourier transform infrared spectrophotometer (FTIR) coupled to an optical microscope (see the experimental section in Chapter 2). The total absorbance (A) is computed as *A = 1-R-T*. Due to layer-by-layer structure of the device and the transparent nature of the ITO glass and thin MoO_3, the optical performance is different when irradiating it from bottom (ITO glass) or from top (gold film). When illuminated from bottom, since ITO glass and MoO_3 thin films are nearly transparent, the light passing through the substrate has quite low optical loss before reaching the N2200 film. The measured absorption spectrum of N2200 film (see Figure 6.1b) also indicates that above the band-edge wavelength of the N2200 film the absorbance is zero, therefore, the light can effectively reach and be absorbed by the plasmonic gold nanostructure to excite surface plasmons. The spectral response can be tailored by changing the LP of the periodic pyramid arrays, which is appealing for solar energy harvesting [136],[137] and infrared detection [10],[21]. The sketch of measured optical absorbance of the devices with light irradiated from the ITO glass is shown in Figure 6.7a. In Figure 6.7c, it is clearly shown that the absorbance of the patterned devices is larger than 88% in the whole measured wavelength ranging from 700 to 1100 nm, whereas the absorbance of the unpatterned flat device is substantially lower. Especially in the wavelength range above the N2200 film band edge, there is an extraordinary absorbance enhancement by around 30% of patterned devices with respect to the device with flat surface. The increased absorption on the patterned device arises from the excitation of surface plasmon polaritons of the pyramid arrays on Au/N2200 device. In the wavelength region below the N2200 band-edge, these three devices show a similar absorbance. However, in the NIR wavelength region above 844 nm, the LP = 400 nm device shows a broad and nearly flat absorbance of 88%, the LP = 500 nm device shows a gradually increasing absorption from 900 nm to 1100 nm and the LP = 600 nm device possesses a distinct resonance absorption with maximum value of 95% at 955 nm. Figure 6.7b shows the sketch of device irradiated from the gold film side. As shown in Figure 6.7d, the absorbance of devices with different LPs show low absorption, less than 50%. Typically,

for LP = 400 nm devices, the absorption amounts to 33-22%, which is much lower than LP = 500 and 600 nm devices. The low absorbance performance of the LP = 400 nm device is likely due to it having smaller pyramids on the surface than the other two device types, resulting on a "smoother" surface with effectively higher reflection than the devices patterned with larger sized pyramids.
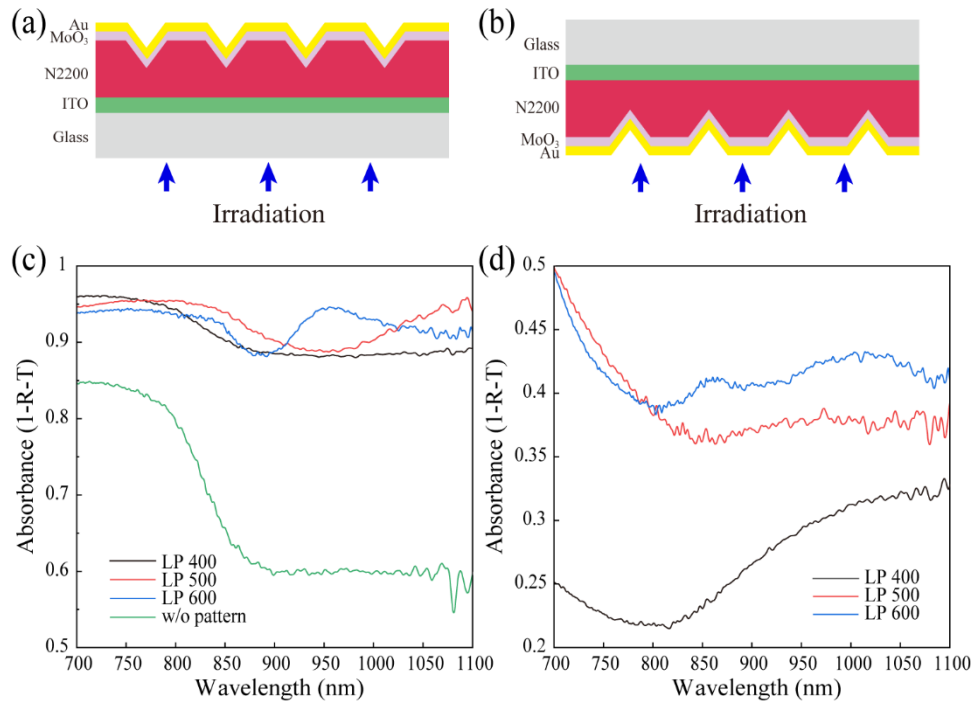
Figure 6.7: Measured absorbance of the gold covered inverted pyramid arrays on N2200 film. Sketch of the illumination from the backside (ITO glass) (a) and front side (gold film) (b) of the device. (c) Absorbance from the backside of the device with pyramid arrays of LP = 400, 500, 600 nm and without (w/o) pattern (bottom). (d) Absorbance from the front side of structure with pyramid arrays of LP = 400, 500, 600 nm (bottom). (Au: 30 nm; MoO$_3$: 5 nm; N2200: 400 nm).

nm device, there is a strong absorption feature similar to LP = 400 nm device but red-shifted to 1050 nm and a tiny absorption at around 844 nm. As for the LP = 600 nm device, a similar strong and broad absorption is further red-shifted to 1250 nm other strong and sharp absorption features appear at shorter wavelengths in the range between 860-1040 nm. The red-shift of the broad absorption feature in these three simulations arises from the optical

phenomenon known as Rayleigh anomaly (RA), which we have discussed in Chapter 3, and that is associated with light diffracted parallel to the surface of the regular array, acting as a grating. The lowest order RA occurs at a wavelength given by:

$$\lambda_{RA} = n_{mix} \cdot LP$$

Here, $n_{mix} = 2.1$ is the estimated refractive index of N2200 and MoO_3 film in the NIR region and LP is the lattice parameter of the arrays. For the device with LP = 500 nm, the Rayleigh anomaly is expected to occur around 1050 nm, in good agreement with the calculation result. For the LP = 600 and 400 nm devices, using the estimated refractive index n_{mix}, the Rayleigh anomaly features of these two devices should appear at 1260 and 840 nm respectively, and the simulation results show that there are corresponding features at 1250 and 870 nm, which fit well between the predicted and simulated results; the small difference arises most likely from uncertainties in the refractive index n_{mix} of the mix. The other absorption features in the LP = 600 nm device in the 860-1040 nm range might be related with the size of pyramids. All these three devices share the same absorption below 844 nm. This uniform high absorption in the shorter wavelength region is mainly due to the strong absorption of the
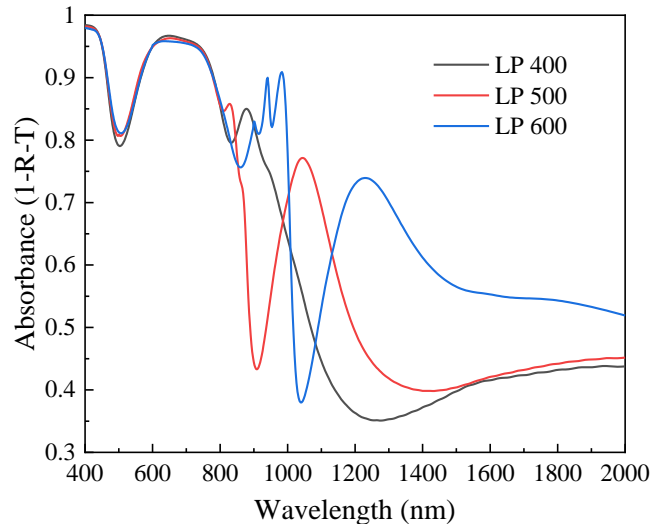

Figure 6.8: Simulated device absorbance from 400 to 2000 nm of devices LP = 400, 500, 600 nm (Au: 30 nm; MoO_3: 5 nm; N2200: 400 nm).

N2200 film (see Figure 6.1b), as we have shown before that the MoO_3 thin film does not have much effect on the optical absorption of the device.

Moreover, we performed the FDTD absorption simulation on the device with and without texturization to verify if the simulation reproduces the same result, namely, that patterning with inverted pyramid arrays leads to absorption increase. As shown in Figure 6.9a, the flat N2200 film covered with 30 nm-thick gold shows a higher absorbance than the device only covered with flat N2200 film (no gold), but both display a similar feature of relative high absorbance below the band edge wavelength but low absorbance (below 10%) at longer wavelengths. After nanotexturization with LP = 600 nm arrays, strong absorbance appears in the region above N2200 band edge wavelength of 844 nm. Therefore, it can be concluded that the patterned plasmonic nanostructure can harvest NIR light in bottom irradiation configuration. The same phenomenon is also found experimentally, as displayed in Figure 6.9b, where we compare a device with flat gold and MoO_3 films on top of N2200 film and a device patterned with a LP = 600 nm inverted pyramid array. Both show a similar high absorbance below the band edge wavelength, whereas the patterned device exhibits an obvious absorption increment in the region above 844 nm. The very good agreement between simulation and experiment is indicative of the high quality of our fabricated structures and the reproducibility of the result, despite the unavoidable development of cracks in the films during the transfer process.
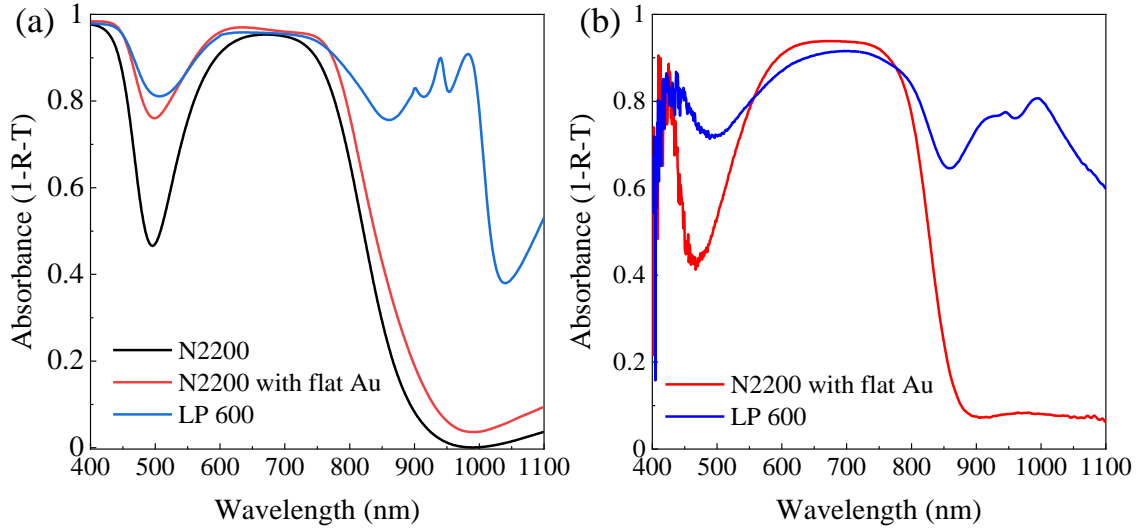
Figure 6.9: Device absorbance. Simulated (a) and measured (b) absorbance of devices with and without LP = 600 nm pattern (Au: 30 nm; MoO$_3$: 5 nm; N2200: 400 nm).

In addition, near-field analysis was carried out to study the electric-field distribution of the designed device at their typical wavelengths in the simulation results. Figure 6.10 shows the results of FDTD simulations as far as the near field is concerned, carried out for the LP = 600 nm device, for which the far-field response was calculated previously (see Figure 6.8). Figure 6.10a is the sketch of the structure and polarization configuration. Two typical wavelengths of 900 and 1250 nm are selected, where the calculated reflectance reaches a maximum. As illustrated by the contour plots of Figure 6.10b,c, for the device of LP = 600 nm, the enhancement of the intensity of the electric-field component ($|E|^2/|E_0|^2$) for P-polarized light at the two selected wavelengths exhibits maxima mainly at the facets along the Au/N2200 interface. The E-field intensity enhancement at two selected wavelengths is around 5 to 6. These hot spots at the Au/N2200 interface are instrumental for obtaining high hot-electron photocurrents in metallic nanostructures [104],[105]. The intense E-field below the apex of the 4-facets pyramid towards the N2200/ITO interface is mainly due to the interaction of conductive ITO glass and N200 polymer. If a thick N2200 film is used, this E-field at the interface will be far away from the pyramid tip and decrease in intensity. This result is caused by the similar phenomenon obtained on 4-facets Au/Si pyramids device. In the same way, in the symmetrical Au/semiconductor polymer pyramids structure, the electric fields generated by the same but opposite dipoles exactly cancel each other at the pyramid tip. Therefore, the

near E-field of this kind of structure is mainly distributed at the Au/semiconductor interfaces but not pyramid apex positions.
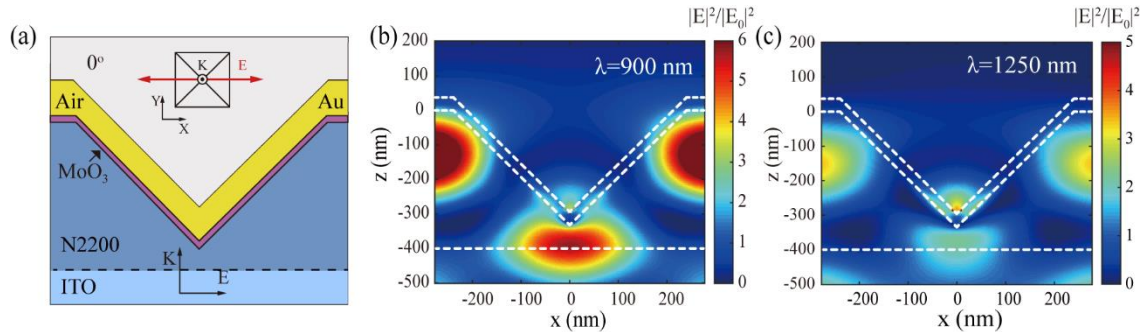

Figure 6.10: Near field analysis. (a) Sketch of the geometry and polarization configuration for a planar monitor corresponding to a cross section through the middle of the pyramid along two facets (0°-monitor). K is the wave vector of the light and E the electric field component. (b). Electric-field distribution of the LP = 600 nm device for P-polarized light in the 0°-monitor plane for the resonance at 900 nm (a) and 1250 nm (b), respectively.

As we have shown, the fabricated devices show enhanced light absorption and electric field enhancements at the metal/semiconductor interface for wavelengths longer than that of the band edge. These are ideal conditions for hot-electron photocurrent generation in the working spectral region. Therefore, we are now set to study the optoelectronic performance of the devices, which includes measuring current-voltage (I-V) curve, photocurrent and responsivity. Figure 6.11 shows the current obtained on LP = 600 nm device with and without light illumination at 1300 nm measured in the voltage range from -300 to 300 µA. The inset displays a much smaller voltage range to emphasize the effect of the illumination with NIR light, what causes a rigid shift of the whole photocurrent curve by about 70 to 95 nA. Such a behavior indicates that the increased current under light irradiation arises from the photoelectric response of the device. The photocurrent collected at 1300 nm, a wavelength which is far away from the bandgap or the emission [133] of the N2200 polymer, can only come from hot electrons generated in the plasmonic gold nanostructure and injected into the N2200 film by an internal photoemission process. The slope of the I-V curve represents the resistance of the fabricated metal/organic-semiconductor device, which gives a constant

value of 142 Ω. Since the slope does not change upon illumination, this is evidence that the increment of the photocurrent is not related to any variation of the sample resistance due to temperature effects, for example.
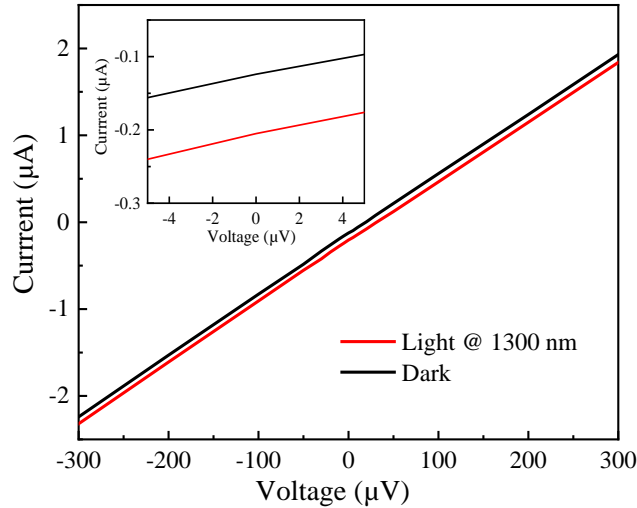
Figure 6.11: I-V response of LP = 600 nm device without and with light illumination at 1300 nm. Inset: Enlarged I-V curve in -5 V to 5 V.

The regions measured on the device include areas with regular pattern and areas near defects of the pattern. Figure 6.12a shows the SEM image of LP = 500 nm device, showing areas with patterned arrays and also defects in the pattern. Figure 6.12b shows the measured photocurrents of the LP = 500 nm device for different illumination spots. On the pattern region (red line) with regular inverted pyramids, the photocurrent shows a first increase and then decrease trend with maximum photocurrent of 0.24 µA at 700 nm. Near the defect on the patterned area (black line), the photocurrent follows the same trend as before but with a higher maximum photocurrent of 0.52 µA at the same wavelength of 700 nm, which is two times larger than on regular pattern region. In contrast, on the planar surface of the device (blue line) the photocurrent response is negligible in the same working spectral range. The responsivity (*R*) was also studied and is given by:

$$R = I_0/P_{in}$$

Here, I_0 is the photocurrent and P_{in} is the light input power. For the LP = 500 nm device, the responsivity near the defect area is still two times larger than on the regular pattern area, whereas the responsivity on the flat surface is again negligible, which means that without pattern, the device is not sensitive to the light (Figure 6.12c). Figure 6.12d shows the SEM image of LP = 600 nm device, emphasizing the defect area and arrays of pattern around it. The photocurrent of the LP = 600 nm device was also investigated, as shown in Figure 6.12e. The maximum photocurrent approaches 2 μA at 700 nm, as obtained near the defect area (black line) and on the regular pattern the maximum photocurrent was 8 times lower (red line). Once more, the photocurrent of the flat region (blue line) is still insignificant. The mechanism leading to the difference in photocurrent between the case near the defect region and on the regular pattern but away from the defect is still elusive to us, although we think that it is somehow related to a kind of "edge" effect. This idea certainly needs further investigation. The responsivities of the LP = 600 nm are shown in Figure 6.12f. On the regular pattern but away from the defect, the responsivity shows a broad response between 0.1 to 0.3 mA/W, whereas the signal is almost absent on flat device. On the contrary, in a region close to the defect, the responsivity exhibits a well-defined and narrow peak in the 650-900 nm spectral region with maximal response of ca. 1 mA/W. In the long wavelength range, the responsivity is low (0.82 mA/W) but shows a steady increase towards a wavelength of 1033 nm.
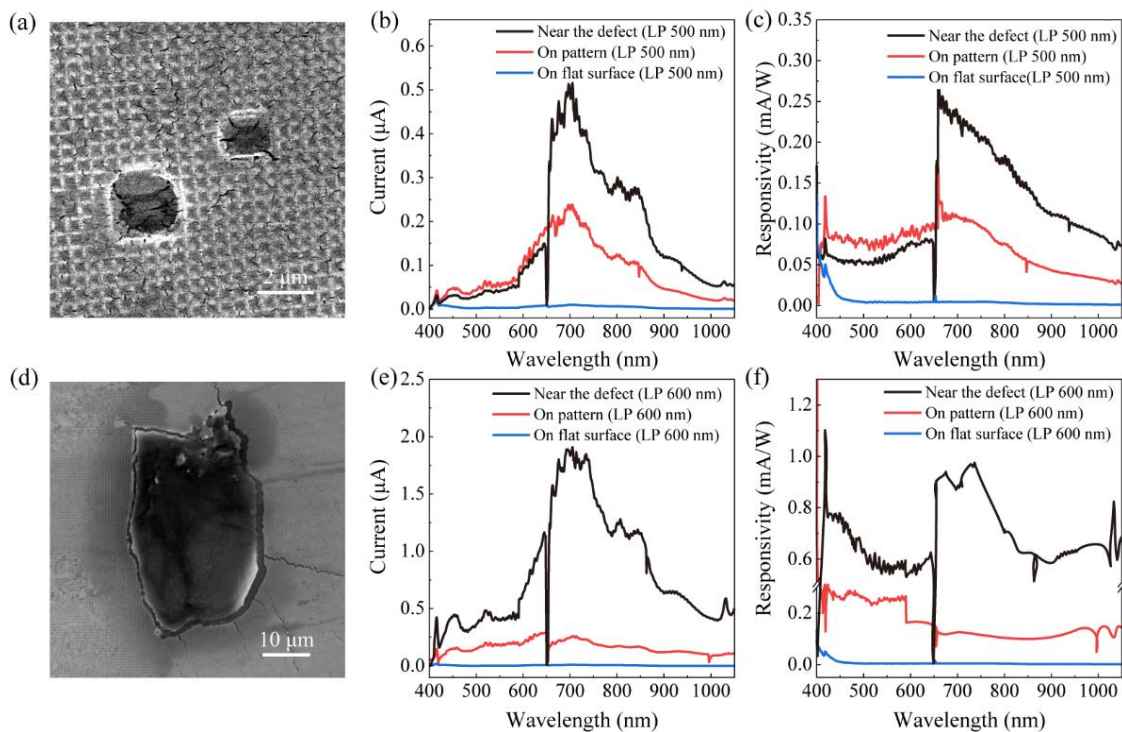
Figure 6.12: Device photoelectric performance (Irradiating from ITO glass side). (a) Defects on the LP = 500 nm device. Photocurrent (b) and responsivity (c) as a function of wavelength of the LP = 500 nm device. (d) Defect on the LP = 600 nm device. Photocurrent (e) and responsivity (f) as a function of wavelength of the LP = 600 nm device.

In order to clarify the mechanism of generated photocurrent, we compared the responsivity and the measured absorbance of LP = 600 nm device in the spectral range of 400 to 1100 nm (Figure 6.13). For photocurrent generation two mechanisms are considered for the light utilization from visible to NIR wavelength range: plasmon-induced resonance energy transfer (PIRET) and hot electron (HE) injection. Resonance energy transfer (RET, also known as Förster resonance energy transfer (FRET), or fluorescence resonance energy transfer) is an optical process, in which the excess energy of an excited molecule, usually called the donor, is transferred to an acceptor molecule [138], as shown in Figure 6.13a. In RET, upon the relaxation of an electron to a lower energy electronic state of the donor, the excess energy is transferred to the acceptor via an emitted *virtual* photon, bringing the acceptor into an excited state. This transfer is mediated by dipole-dipole couplings between the molecules. In fact, photons play two distinct roles toward the process: one as the mediator of donor-acceptor

transfer, and the other as an external energy source that promotes donor valence electrons into an electronic excited state, via an absorption process prior to RET. As shown in Figure 6.13b for the LP = 600 nm device, the responsivity has a maximum at 735 nm, coinciding with the location of maximal absorption which is mainly attributed to the absorption of N2200 (see also Figure 6.9). The high optoelectronic performance arises from the light impinging on metallic film being absorbed by the plasmonic resonance and the surface plasmon energy being directly transferred non-radiatively to the semiconductor N2200 through dipole-dipole interaction, locally generating electron-hole pairs in the semiconductor. Holes in the semiconductor move to the anode electrode (gold electrode) and are collected by the external circuit while the electrons are collected after moving to the cathode (ITO glass), this process follows the PIRET mechanism. In the longer measured wavelength range above 844 nm (Figure 6.13b right), the LP = 600 nm device still has a prominent responsivity for a relatively low absorption which is mainly attributed to plasmon resonances of the metallic gold film. In this wavelength region, surface plasmons are excited after the light impinges on the gold film. Such surface plasmon absorption in the gold film leads to the creation of hot electrons with sufficient energy to overcome the Schottky barrier of Au/N2200, being injected into N2200 and leaving holes behind in the gold, a process usually known as hot electron injection mechanism. These internally emitted hot electrons are finally collected by the ITO electrode, while the holes that are left in the gold film are collected via external circuit (gold acts as anode electrode). In the measured wavelength range from visible to NIR, PIRET process is more effective in the visible region to 844 nm; in the NIR region from 844 to 1100 nm, hot electron injection process is responsible for the photocurrent generation. Generally, both HE and PIRET mechanisms work simultaneously in our device for the photocurrent generation.
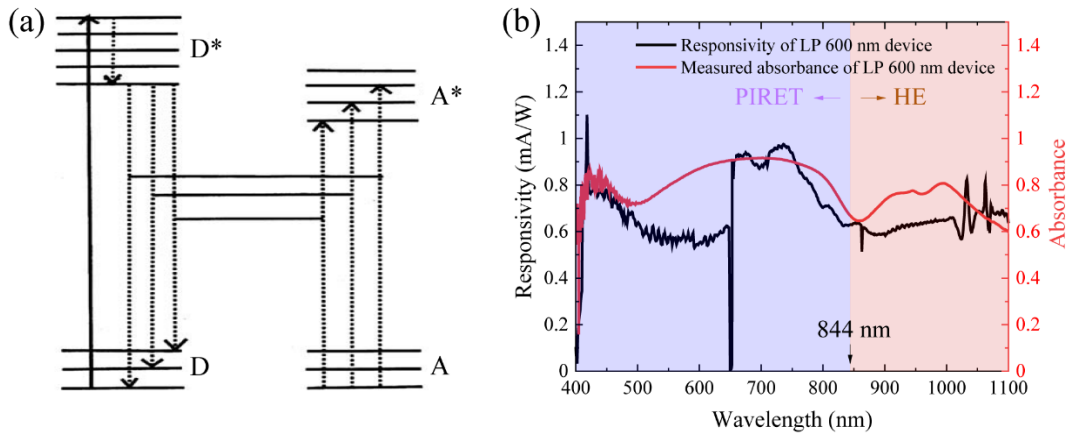
Figure 6.13: Mechanism of the photoelectric device (a) Schematic diagram of resonance energy transfer (RET). (b) Related mechanisms (PIRET and HE) for photocurrent in the working wavelength range (400-1100 nm).

We will now compare the performance of our fabricated Au/N2200 pyramids device and the as-prepared 4-facets and 3-facets Au/Si pyramid devices in this thesis with similar photocurrent generators available in the literature, which are all based on Au/Si plasmonic structures. In table 6.2 we list the peak responsivities of all devices, the wavelength at which the response is obtained and if a bias was applied or not. All these Au/Si devices give a responsivity in NIR region that changes by several orders of magnitude from a low response of 4.30 nA/W with applied external bias at 1550 nm to a high response of 8.17 mA/W without any bias applied [10],[20],[114],[122],[139]–[141]. For our fabricated 4-facets and 3-facets Au/Si pyramids devices, without any external bias, the maximal responsivity reaches to 0.63 and 3.40 mA/W respectively. For the Au/N2200 pyramids device that using a soft organic semiconductor, without bias applied, the responsivity approaches 1 mA/W at 735 nm, and a lower responsivity of 0.82 mA/W is attained at longer wavelength to 1033 nm. In general, we can affirm that the performance of our device is comparable to that of the best Au/Si counterparts.

Table 6.2: Table of the maximal responsivity of the as-reported Au/Si-based devices and the Au/semiconductor pyramids devices in this thesis.

Device structure	Peak responsivity	Applied bias (V)
Au antennas/Si	9.50 nA/W@1250 nm	0
Au grating/Si substrate	0.60 mA/W@1480 nm	0
Au/Si metamaterial	3.37 mA/W@1250 nm	0
Au/Si trench	0.15 mA/W@1550 nm	0
Au/Si nanoholes	4.30 mA/W@1500 nm	-5
Au NP/Si pyramids	8.17 mA/W@1200 nm	0
Au NP/Si substrate	1.05 mA/W@1500 nm	-5
This work		
4-facets Au/Si pyramids	0.63 mA/W@1400 nm	0
3-facets Au/Si pyramids	3.40 mA/W@1300 nm	0
Au/N2200 pyramids	0.82 mA/W@1033 nm	0

6.2 Conclusions

In this chapter, we proposed an alternative strategy using metal/organic-semiconductor architecture with imprinted pattern on top to produce photocurrents and compared it to previously used metal/Si structures. The new strategy employs soft NIL technique with potential for large-scale fabrication of hot electron devices comparing with traditional metal/Si scenario, which uses expensive and time-consuming lithography technology. Arrays with inverted pyramids of hundreds of nanometers in size are imprinted on a polymer layer to achieve an enhanced absorbance and photocurrent. The effect of two illumination modes (from ITO glass and gold film) on light absorption and photoelectric conversion capability was investigated. When illuminating from ITO glass, NIR light (below N2200 bandgap) can be effectively confined into the textured devices. The absorbance and photocurrent can be tuned by tailoring the L and LP of the pyramid arrays. The LP = 600 nm device achieved a maximum value of 90% of absorbance in the measured wavelength range from above 844 nm compared with almost no absorbance obtained from device with flat surface. On the pattern region, it shows an obvious photoelectric response compared with flat region out of

the pattern area. The maximum photocurrent close to 2 μA was obtained on LP = 600 device at 700 nm on the pattern area but near a defect in the pattern. This photoelectric response near the defect is 8 times larger than on the regular pattern. The reason for this enhancement is still elusive to us but we believe is related to a kind of edge effect. Correspondingly, the maximum responsivity is obtained on the LP = 600 nm device approaches 1 mA/W at 735 nm and a lower responsivity of 0.82 mA/W was obtained at longer wavelengths (1033 nm), so the responsivity performance of our fabricated device is comparable to that of the Au/Si counterparts. Both HE and PIRET processes work simultaneously in the device for the photocurrent generation in the spectral range from visible to near-infrared wavelengths. Our designed and fabricated device has potential for large-scale production based on a simple NIL technique with competitive photoelectric conversion ability among Au/Si based Schottky diode devices.

Chapter 7

General conclusion and outlook

In this thesis, I have fabricated the silicon pyramids with 4-facets covered with gold and studied their far field optical and near field distribution properties. The 4-facets devices exhibit substantial light absorption in the region below the gap of Si. Intense hot spots distribute throughout the Au/Si interface, characterized by strong enhancements of the electric field. The existence of these hot spots is a prerequisite for enhanced photocurrents. In addition, 3-facets and 2-facets Au covered silicon-pyramids are fabricated by oblique-angle evaporation. Due to the low symmetry, intense hot spots are located at apex of the 3-facets devices. Simulations on smaller pyramids (200-300 nm) show hot spots are characterized by electric-field vectors perpendicular to the metal surface, which is a prerequisite for efficient hot-electron emission. The photoelectrical characterization shows the photocurrents obtained with 3-facets Au/Si devices are on the average five times larger than for the 4-faces counterparts. The remarkable responsivities observed in the spectral range from the visible to the NIR can be explained by the mechanisms of plasmon-induced resonance energy transfer (PIRET) and hot-electron generation, respectively. The photocurrent maps as a function of polarization azimuthal angle in the measured spectral range below Si bandgap exhibit exactly the C_2 symmetry as the absorbance maps. This is compelling evidence of hot-electron photocurrent generation due to NIR light absorption by plasmon resonances in the inverted pyramid plasmonic nanostructures. Au/organic-semiconductor (N2200) based inverted-pyramid devices are fabricated using the "wet embossing" method. Strong light absorption from resonant excitation of surface plasmon and hot spots on the Au/N2200 interface is also observed in the spectral range from visible to NIR. The photoelectrical response of devices is similar to that of the Au/Si counterparts one more the results from PIRET and hot-electron generation mechanisms working synergistically.

The remarkable photocurrent/responsivity obtained from the Au/semiconductors-based inverted-pyramid devices in the spectral region from above but close to the semiconductor

bandgap down to the NIR and the scalable nanostructuration methodologies (NIL) renders the promising application of our structures and fabrication methods in a variety of application areas such as infrared photodetection, photocatalysis, or cell photo-stimulation in the biological IR window, to name a few examples.

References

[1]   Kauranen, M.; Zayats, A. V. Nonlinear Plasmonics. *Nature Photonics* **2012**, *6*, 737.

[2]   Linic, S.; Christopher, P.; Ingram, D. B. Plasmonic-Metal Nanostructures for Efficient Conversion of Solar to Chemical Energy. *Nature Materials* **2011**, *10*, 911.

[3]   Zhang, X.; Chen, Y. L.; Liu, R. S.; Tsai, D. P. Plasmonic Photocatalysis. *Reports on Progress in Physics* **2013**, *76*, 046401.

[4]   Liu, Q.; Romero-Gomez, P.; Mantilla-Perez, P.; Colodrero, S.; Toudert, J.; Martorell, J. A Two-Resonance Tapping Cavity for an Optimal Light Trapping in Thin-Film Solar Cells. *Advanced Energy Materials* **2017**, *7*, 1700356.

[5]   Xu, Y.; Bai, P.; Zhou, X.; Akimov, Y.; Png, C. E.; Ang, L. K.; Knoll, W.; Wu, L. Optical Refractive Index Sensors with Plasmonic and Photonic Structures: Promising and Inconvenient Truth. *Advanced Optical Materials* **2019**, *7*, 31.

[6]   Adato, R.; Guo, J. Modification of Dispersion, Localization, and Attenuation of Thin Metal Stripe Symmetric Surface Plasmon-Polariton Modes by Thin Dielectric Layers. *Journal of Applied Physics* **2009**, *105*, 034306.

[7]   Edward D. Palik. *Handbook of Optical Constants of Solids*; Academic Press, **1998**.

[8]   Andreani, L. C.; Bozzola, A.; Kowalczewski, P.; Liscidini, M.; Redorici, L.; Claudio, L.; Bozzola, A.; Kowalczewski, P.; Liscidini, M.; Andreani, L. C.; Bozzola, A.; Kowalczewski, P.; Liscidini, M.; Redorici, L. Silicon Solar Cells : Toward the Efficiency Limits. *Advances in Physics: X* **2019**, *4*, 1548305.

[9]   Tang, L.; Kocabas, S. E.; Latif, S.; Okyay, A. K.; Ly-Gagnon, D. S.; Saraswat, K. C.; Miller, D. A. B. Nanometre-Scale Germanium Photodetector Enhanced by a near-Infrared Dipole Antenna. *Nature Photonics* **2008**, *2*, 226.

[10]   Sobhani, A.; Knight, M. W.; Wang, Y.; Zheng, B.; King, N. S.; Brown, L. V.; Fang, Z.; Nordlander, P.; Halas, N. J. Narrowband Photodetection in the Near-Infrared with a Plasmon-Induced Hot Electron Device. *Nature Communications* **2013**, *4*, 1643.

[11]   Staude, I.; Schilling, J. Metamaterial-Inspired Silicon Nanophotonics. *Nature Photonics* **2017**, *11*, 274.

[12]   Míguez, B. H.; Chomski, E.; García-santamaría, F.; Ibisate, M.; John, S.; López, C.;

References

Meseguer, F.; Mondia, J. P.; Ozin, G. a; Toader, O.; Driel, H. M. Van. Photonic Bandgap Engineering in Germanium. *Advanced Materials* **2001**, *13*, 1634.

[13] Butun, S.; Tongay, S.; Aydin, K. Enhanced Light Emission from Large-Area Monolayer MoS_2 Using Plasmonic Nanodisc Arrays. *Nano Letters* **2015**, *15*, 2700.

[14] Barnes, W. L.; Dereux, A.; Ebbesen, T. W. Surface Plasmon Subwavelength Optics. *Nature* **2003**, *424*, 824.

[15] Schuller, J. A.; Barnard, E. S.; Cai, W.; Jun, Y. C.; White, J. S.; Brongersma, M. L. Plasmonics for Extreme Light Concentration and Manipulation. *Nature Materials* **2010**, *9*, 193.

[16] Shalaev, V. M. Optical Negative-Index Metamaterials. *Nature Photonics* **2007**, *1*, 41.

[17] Yao, K.; Liu, Y. Plasmonic Metamaterials. *Nanotechnology Reviews* **2014**, *3*, 177.

[18] Alù, A.; Engheta, N. Cloaking a Receiving Antenna or a Sensor with Plasmonic Metamaterials. *Metamaterials* **2010**, *4*, 153.

[19] Park, I. Y.; Kim, S.; Choi, J.; Lee, D. H.; Kim, Y. J.; Kling, M. F.; Stockman, M. I.; Kim, S. W. Plasmonic Generation of Ultrashort Extreme-Ultraviolet Light Pulses. *Nature Photonics* **2011**, *5*, 677.

[20] Li, W.; Valentine, J. Metamaterial Perfect Absorber Based Hot Electron Photodetection. *Nano Letters* **2014**, *14*, 3510.

[21] Chalabi, H.; Schoen, D.; Brongersma, M. L. Hot-Electron Photodetection with a Plasmonic Nanostripe Antenna. *Nano Letters* **2014**, *14*, 1374.

[22] Atwater, H. A.; Polman, A. Plasmonics for Improved Photovoltaic Devices. *Nature Materials* **2010**, *9*, 205.

[23] Pillai, S.; Green, M. A. Plasmonics for Photovoltaic Applications. *Solar Energy Materials and Solar Cells* **2010**, *94*, 1481.

[24] Elghanian, R.; Storhoff, J. J.; Mucic, R. C.; Letsinger, R. L.; Mirkin, C. A. Selective Colorimetric Detection of Polynucleotides Based on the Distance-Dependent Optical Properties of Gold Nanoparticles. *Science* **1997**, *277*, 1078.

[25] Jeffrey N. Anker, W. Paige Hall, Olga Lyandres, Nilam C. Shah, J. Z. & R. P. V. D. Biosensing with Plasmonic Nanosensors. *Nature Materials* **2008**, *7*, 442.

[26] Larsson, E. M.; Alegret, J.; Kăll, M.; Sutherland, D. S. Sensing Characteristics of NIR Localized Surface Plasmon Resonances in Gold Nanorings for Application as

Ultrasensitive Biosensors. *Nano Letters* **2007**, *7*, 1256.

[27] Doria, G.; Conde, J.; Veigas, B.; Giestas, L.; Almeida, C.; Assunção, M.; Rosa, J.; Baptista, P. V. Noble Metal Nanoparticles for Biosensing Applications. *Sensors* **2012**, *12*, 1657.

[28] Cao, J.; Sun, T.; Grattan, K. T. V. Gold Nanorod-Based Localized Surface Plasmon Resonance Biosensors: A Review. *Sensors and Actuators, B: Chemical* **2014**, *195*, 332.

[29] Hu, J.; Pérez, L. A.; Garcia-Pomar, J. L.; Mihi, A.; Garriga, M.; Alonso, M. I.; Goñi, A. R. Efficient Infrared Sunlight Absorbers Based on Gold-Covered, Inverted Silicon Pyramid Arrays. *Materials Advances* **2022**, *3*, 2364.

[30] Tan, T.; Tian, C.; Ren, Z.; Yang, J.; Chen, Y.; Sun, L.; Li, Z.; Wu, A.; Yin, J.; Fu, H. LSPR-Dependent SERS Performance of Silver Nanoplates with Highly Stable and Broad Tunable LSPRs Prepared through an Improved Seed-Mediated Strategy. *Physical Chemistry Chemical Physics* **2013**, *15*, 21034.

[31] Chaparro Chaparro, F.; Quintero Reyes, R. The Lycurgus Cup - A Roman Nanotechnology. *Gold Bulletin* **2007**, *40*, 270.

[32] Maier, S. A. *Plasmonics: Fundamentals and Applications*; **2007**.

[33] Lu, F. F.; Li, T.; Xu, J.; Xie, Z. D.; Li, L.; Zhu, S. N.; Zhu, Y. Y. Surface Plasmon Polariton Enhanced by Optical Parametric Amplification in Nonlinear Hybrid Waveguide. *Optics Express* **2011**, *19*, 2858.

[34] Patskovsky, S.; Kabashin, A. V.; Meunier, M.; Luong, J. H. T. Silicon-Based Surface Plasmon Resonance Sensing with Two Surface Plasmon Polariton Modes. *Applied Optics* **2003**, *42*, 6905.

[35] Fang, N.; Lee, H.; Sun, C.; Zhang, X. Sub-Diffraction-Limited Optical Imaging with a Silver Superlens. *Science* **2005**, *208*, 534.

[36] Ono, A.; Kato, J. I.; Kawata, S. Subwavelength Optical Imaging through a Metallic Nanorod Array. *Physical Review Letters* **2005**, *95*, 267407.

[37] Nikolajsen, T.; Leosson, K.; Salakhutdinov, I.; Bozhevolnyi, S. I. Polymer-Based Surface-Plasmon-Polariton Stripe Waveguides at Telecommunication Wavelengths. *Applied Physics Letters* **2003**, *82*, 668.

[38] Unutmaz, M. A.; Unlu, M. Terahertz Spoof Surface Plasmon Polariton Waveguides:

References

A Comprehensive Model with Experimental Verification. *Scientific Reports* **2019**, *9*, 7616.

[39] Gagan Kumar & Prashant K. Sarswat. *Interaction of Surface Plasmon Polaritons with Nanomaterials*; Springer, **2016**.

[40] Kneipp, K.; Moskovits, M.; Kneipp, H. *Surface-Enhanced Raman Scattering*; Springer, **2006**.

[41] Halas, N. J. Connecting the Dots: Reinventing Optics for Nanoscale Dimensions. *Proceedings of the National Academy of Sciences of the United States of America* **2009**, *106*, 3643.

[42] Arakawa, E. T.; Williams, M. W.; Hamm, R. N.; Ritchie, R. H. Effect of Damping on Surface Plasmon Dispersion. *Physical Review Letters* **1973**, *31*, 1127.

[43] Alexander, R. W.; Kovener, G. S.; Bell, R. J. Dispersion Curves for Surface Electromagnetic Waves with Damping. *Physical Review Letters* **1974**, *32*, 154.

[44] Kretschmann, E.; Raether, H. Radiative Decay of Non Radiative Surface Plasmons Excited by Light. *Zeitschrift fur Naturforschung* **1968**, *23*, 2135.

[45] Zhang, J.; Zhang, L.; Xu, W. Surface Plasmon Polaritons: Physics and Applications. *Journal of Physics D: Applied Physics* **2012**, *45*, 113001.

[46] Schuck, P. J. Nanoimaging: Hot Electrons Go through the Barrier. *Nature Nanotechnology* **2013**, *8*, 799.

[47] Clavero, C. Plasmon-Induced Hot-Electron Generation at Nanoparticle/Metal-Oxide Interfaces for Photovoltaic and Photocatalytic Devices. *Nature Photonics* **2014**, *8*, 95.

[48] Brongersma, M. L.; Halas, N. J.; Nordlander, P. Plasmon-Induced Hot Carrier Science and Technology. *Nature Nanotechnology* **2015**, *10*, 25.

[49] Hogan, N. J.; Urban, A. S.; Ayala-Orozco, C.; Pimpinelli, A.; Nordlander, P.; Halas, N. J. Nanoparticles Heat through Light Localization. *Nano Letters* **2014**, *14*, 4640.

[50] Zheng, B. Y.; Zhao, H.; Manjavacas, A.; McClain, M.; Nordlander, P.; Halas, N. J. Distinguishing between Plasmon-Induced and Photoexcited Carriers in a Device Geometry. *Nature Communications* **2015**, *6*, 7797.

[51] Wu, K.; Rodríguez-Córdoba, W. E.; Yang, Y.; Lian, T. Plasmon-Induced Hot Electron Transfer from the Au Tip to CdS Rod in CdS-Au Nanoheterostructures. *Nano Letters* **2013**, *13*, 5255.

References

[52] Link, S.; El-Sayed, M. A. Spectral Properties and Relaxation Dynamics of Surface Plasmon Electronic Oscillations in Gold and Silver Nanodots and Nanorods. *Journal of Physical Chemistry B* **1999**, *103*, 8410.

[53] Hartland, G. V. Optical Studies of Dynamics in Noble Metal Nanostructures. *Chemical Reviews* **2011**, *111*, 3858.

[54] Leenheer, A. J.; Narang, P.; Lewis, N. S.; Atwater, H. A. Solar Energy Conversion via Hot Electron Internal Photoemission in Metallic Nanostructures: Efficiency Estimates. *Journal of Applied Physics* **2014**, *115*, 134301.

[55] Wu, K.; Chen, J.; McBride, J. R.; Lian, T. Efficient Hot-Electron Transfer by a Plasmon-Induced Interfacial Charge-Transfer Transition. *Science* **2015**, *349*, 632.

[56] Huang, X.; Li, H.; Zhang, C.; Tan, S.; Chen, Z.; Chen, L.; Lu, Z.; Wang, X.; Xiao, M. Efficient Plasmon-Hot Electron Conversion in Ag–$CsPbBr_3$ Hybrid Nanocrystals. *Nature Communications* **2019**, *10*, 1163.

[57] Li, J.; Cushing, S. K.; Meng, F.; Senty, T. R.; Bristow, A. D.; Wu, N. Plasmon-Induced Resonance Energy Transfer for Solar Energy Conversion. *Nature Photonics* **2015**, *9*, 601.

[58] Tan, S.; Argondizzo, A.; Ren, J.; Liu, L.; Zhao, J.; Petek, H. Plasmonic Coupling at a Metal/Semiconductor Interface. *Nature Photonics* **2017**, *11*, 806.

[59] Gong, T.; Munday, J. N. Angle-Independent Hot Carrier Generation and Collection Using Transparent Conducting Oxides. *Nano Letters* **2015**, *15*, 147.

[60] Zhang, C.; Wu, K.; Zhan, Y.; Giannini, V.; Li, X. Planar Microcavity-Integrated Hot-Electron Photodetector. *Nanoscale* **2016**, *8*, 10323.

[61] Fowler, R. H. The Analysis of Photoelectric Sensitivity Curves for Clean Metals at Various Temperatures. *Physical Review* **1931**, *38*, 45.

[62] Zhao, G.; Kozuka, H.; Yoko, T. Sol-Gel Preparation and Photoelectrochemical Properties of TiO_2 Films Containing Au and Ag Metal Particles. *Thin Solid Films* **1996**, *277*, 147.

[63] Tian, Y.; Tatsuma, T. Mechanisms and Applications of Plasmon-Induced Charge Separation at TiO_2 Films Loaded with Gold Nanoparticles. *Journal of the American Chemical Society* **2005**, *127*, 7632.

[64] Kochuveedu, S. T.; Kim, D. P.; Kim, D. H. Surface-Plasmon-Induced Visible Light

Photocatalytic Activity of TiO$_2$ Nanospheres Decorated by Au Nanoparticles with Controlled Configuration. *Journal of Physical Chemistry C* **2012**, *116*, 2500.

[65] Chen, Z. H.; Tang, Y. B.; Liu, C. P.; Leung, Y. H.; Yuan, G. D.; Chen, L. M.; Wang, Y. Q.; Bello, I.; Zapien, J. A.; Zhang, W. J.; Lee, C. S.; Lee, S. T. Vertically Aligned ZnO Nanorod Arrays Sentisized with Gold Nanoparticles for Schottky Barrier Photovoltaic Cells. *Journal of Physical Chemistry C* **2009**, *113*, 13433.

[66] García De Arquer, F. P.; Mihi, A.; Konstantatos, G. Large-Area Plasmonic-Crystal-Hot-Electron-Based Photodetectors. *ACS Photonics* **2015**, *2*, 950.

[67] Feng, B.; Zhu, J.; Lu, B.; Liu, F.; Zhou, L.; Chen, Y. Achieving Infrared Detection by All-Si Plasmonic Hot-Electron Detectors with High Detectivity. *ACS Nano* **2019**, *13*, 8433.

[68] Capper, P.; Irvine, S.; Joyce, T. *Epitaxial Crystal Growth: Methods and Materials*; Springer, **2017**.

[69] Vaccaro, P. O.; Alonso, M. I.; Garriga, M.; Gutiérrez, J.; Peró, D.; Wagner, M. R.; Reparaz, J. S.; Sotomayor Torres, C. M.; Vidal, X.; Carter, E. A.; Lay, P. A.; Yoshimoto, M.; Goñi, A. R. Localized Thinning for Strain Concentration in Suspended Germanium Membranes and Optical Method for Precise Thickness Measurement. *AIP Advances* **2018**, *8*, 115131.

[70] Luo, Y. H.; Wan, J.; Forrest, R. L.; Liu, J. L.; Jin, G.; Goorsky, M. S.; Wang, K. L. Compliant Effect of Low-Temperature Si Buffer for SiGe Growth. *Applied Physics Letters* **2001**, *78*, 454.

[71] Kasper, E.; Lyutovich, K.; Bauer, M.; Oehme, M. New Virtual Substrate Concept for Vertical MOS Transistors. *Thin Solid Films* **1998**, *336*, 319.

[72] Yeh, W.; Matsumoto, A.; Sugihara, K.; Hayase, H. Sputter Epitaxial Growth of Flat Germanium Film with Low Threading-Dislocation Density on Silicon (001). *ECS Journal of Solid State Science and Technology* **2014**, *3*, Q195.

[73] Hua, F.; Sun, Y.; Gaur, A.; Meitl, M. A.; Bilhaut, L.; Rotkina, L.; Wang, J.; Geil, P.; Shim, M.; Rogers, J. A.; Shim, A. Polymer Imprint Lithography with Molecular-Scale Resolution. *Nano Letters* **2004**, *4*, 2467.

[74] Yu, C. C.; Chen, H. L. Nanoimprint Technology for Patterning Functional Materials and Its Applications. *Microelectronic Engineering* **2015**, *132*, 98.

[75]   Mihi, A.; Beck, F. J.; Lasanta, T.; Rath, A. K.; Konstantatos, G. Imprinted Electrodes for Enhanced Light Trapping in Solution Processed Solar Cells. *Advanced Materials* **2014**, *26*, 443.

[76]   Gómez-Castaño, M.; Garcia-Pomar, J. L.; Pérez, L. A.; Shanmugathasan, S.; Ravaine, S.; Mihi, A. Electrodeposited Negative Index Metamaterials with Visible and Near Infrared Response. *Advanced Optical Materials* **2020**, *8*, 2000865.

[77]   Fu, X.; Chen, Q.; Chen, X.; Zhang, L.; Yang, A.; Cui, Y.; Yuan, C.; Ge, H. A Rapid Thermal Nanoimprint Apparatus through Induction Heating of Nickel Mold. *Micromachines* **2019**, *10*, 334.

[78]   Chou, S. Y.; Krauss, P. R.; Zhang, W.; Guo, L.; Lei Zhuang. Sub-10 Nm Imprint Lithography and Applications. *Journal of Vacuum Science & Technology B* **1997**, *15*, 2897.

[79]   Austin, M. D.; Ge, H.; Wu, W.; Li, M.; Yu, Z.; Wasserman, D.; Lyon, S. A.; Chou, S. Y. Fabrication of 5nm Linewidth and 14nm Pitch Features by Nanoimprint Lithography. *Applied Physics Letters* **2004**, *84*, 5299.

[80]   Guo, L. J. Nanoimprint Lithography: Methods and Material Requirements. *Advanced Materials* **2007**, *19*, 495.

[81]   Bruinink, C. M.; Péter, M.; De Boer, M.; Kuipers, L.; Huskens, J.; Reinhoudt, D. N. Stamps for Submicrometer Soft Lithography Fabricated by Capillary Force Lithography. *Advanced Materials* **2004**, *16*, 1086.

[82]   Lam, R. H. W.; Sun, Y.; Chen, W.; Fu, J. Elastomeric Microposts Integrated into Microfluidics for Flow-Mediated Endothelial Mechanotransduction Analysis. *Lab on a Chip* **2012**, *12*, 1865.

[83]   Odom, T. W.; Love, J. C.; Wolfe, D. B.; Paul, K. E.; Whitesides, G. M. Improved Pattern Transfer in Soft Lithography Using Composite Stamps. *Langmuir* **2002**, *18*, 5314.

[84]   Choi, D.-G.; Jeong, J.; Sim, Y.; Lee, E.; Kim, W.-S.; Bae, and B.-S. Fluorinated Organic−Inorganic Hybrid Mold as a New Stamp for Nanoimprint and Soft Lithography. *Langmuir* **2005**, *21*, 9390.

[85]   Inglis, D. W. A Method for Reducing Pressure-Induced Deformation in Silicone Microfluidics. *Biomicrofluidics* **2010**, *4*, 026504.

References

[86] Li, Z.; Gu, Y.; Wang, L.; Ge, H.; Wu, W.; Xia, Q.; Yuan, C.; Chen, Y.; Cui, B.; Williams, R. S. Hybrid Nanoimprint−Soft Lithography with Sub-15 Nm Resolution. *Nano Letters* **2009**, *9*, 2306.

[87] Williams, S. S.; Retterer, S.; Lopez, R.; Ruiz, R.; Samulski, E. T.; Desimone, J. M. High-Resolution PFPE-Based Molding Techniques for Nanofabrication of High-Pattern Density, Sub-20 Nm Features: A Fundamental Materials Approach. *Nano Letters* **2010**, *10*, 1421.

[88] Jaeger, R. C. *Introduction to Microelectronic Fabrication*; Prentice Hall, **2002**.

[89] Bharat Bhushan. *Encyclopedia of Nanotechnology*; Springer, **2012**.

[90] Verruijt, A. Numerical Solution of Initial Boundary Value Problems Involving Maxwell's Equations in Isotropic Media. *IEEE Transactions on Antennas and Propagation* **1966**, *14*, 302.

[91] P. B. Johnson and R. W. Christy. Optical Constant of the Nobel Metals. *Physical Review B* **1972**, *6*, 4370.

[92] Vos, M. F. J.; Macco, B.; Thissen, N. F. W.; Bol, A. A.; Kessels, W. M. M. (Erwin). Atomic Layer Deposition of Molybdenum Oxide from $(NtBu)_2(NMe_2)_2Mo$ and O_2 Plasma. *Journal of Vacuum Science & Technology A: Vacuum, Surfaces, and Films* **2016**, *34*, 01A103.

[93] Pierce, D. T.; Spicer, W. E. Electronic Structure of Amorphous Si from Photoemission and Optical Studies. *Physical Review B* **1972**, *5*, 3017.

[94] König, T. A. F.; Ledin, P. A.; Kerszulis, J.; Mahmoud, M. A.; El-Sayed, M. A.; Reynolds, J. R.; Tsukruk, V. V. Electrically Tunable Plasmonic Behavior of Nanocube-Polymer Nanomaterials Induced by a Redox-Active Electrochromic Polymer. *ACS Nano* **2014**, *8*, 6182.

[95] Hsu, C. M.; Battaglia, C.; Pahud, C.; Ruan, Z.; Haug, F. J.; Fan, S.; Ballif, C.; Cui, Y. High-Efficiency Amorphous Silicon Solar Cell on a Periodic Nanocone Back Reflector. *Advanced Energy Materials* **2012**, *2*, 628.

[96] Oh, J.; Yuan, H. C.; Branz, H. M. An 18.2%-Efficient Black-Silicon Solar Cell Achieved through Control of Carrier Recombination in Nanostructures. *Nature Nanotechnology* **2012**, *7*, 743.

[97] Gu, X.; Yu, X.; Guo, K.; Chen, L.; Wang, D.; Yang, D. Seed-Assisted Cast Quasi-

References

Single Crystalline Silicon for Photovoltaic Application: Towards High Efficiency and Low Cost Silicon Solar Cells. *Solar Energy Materials and Solar Cells* **2012**, *101*, 95.

[98] Jarman, J. T.; Khalil, E. E.; Khalaf, E. Energy Analyses of Thermoelectric Renewable Energy Sources. *Open Journal of Energy Efficiency* **2013**, *02*, 143.

[99] White, T. P.; Catchpole, K. R. Plasmon-Enhanced Internal Photoemission for Photovoltaics: Theoretical Efficiency Limits. *Applied Physics Letters* **2012**, *101*, 073905.

[100] Govorov, A. O.; Zhang, H.; Gun'Ko, Y. K. Theory of Photoinjection of Hot Plasmonic Carriers from Metal Nanostructures into Semiconductors and Surface Molecules. *Journal of Physical Chemistry C* **2013**, *117*, 16616.

[101] Zhang, Y.; Yam, C.; Schatz, G. C. Fundamental Limitations to Plasmonic Hot-Carrier Solar Cells. *Journal of Physical Chemistry Letters* **2016**, *7*, 1852.

[102] Jiang, R.; Li, B.; Fang, C.; Wang, J. Metal/Semiconductor Hybrid Nanostructures for Plasmon-Enhanced Applications. *Advanced Materials* **2014**, *26*, 5274.

[103] Tang, H.; Chen, C. J.; Huang, Z.; Bright, J.; Meng, G.; Liu, R. S.; Wu, N. Plasmonic Hot Electrons for Sensing, Photodetection, and Solar Energy Applications: A Perspective. *Journal of Chemical Physics* **2020**, *152*, 220901.

[104] Zhang, H.; Govorov, A. O. Optical Generation of Hot Plasmonic Carriers in Metal Nanocrystals: The Effects of Shape and Field Enhancement. *Journal of Physical Chemistry C* **2014**, *118*, 7606.

[105] Sousa-Castillo, A.; Comesaña-Hermo, M.; Rodríguez-González, B.; Pérez-Lorenzo, M.; Wang, Z.; Kong, X. T.; Govorov, A. O.; Correa-Duarte, M. A. Boosting Hot Electron-Driven Photocatalysis through Anisotropic Plasmonic Nanoparticles with Hot Spots in Au-TiO$_2$ Nanoarchitectures. *Journal of Physical Chemistry C* **2016**, *120*, 11690.

[106] Sivasubramaniam, S.; Alkaisi, M. M. Inverted Nanopyramid Texturing for Silicon Solar Cells Using Interference Lithography. *Microelectronic Engineering* **2014**, *119*, 146.

[107] Trompoukis, C.; Massiot, I.; Depauw, V.; El Daif, O.; Lee, K.; Dmitriev, A.; Gordon, I.; Mertens, R.; Poortmans, J. Disordered Nanostructures by Hole-Mask Colloidal Lithography for Advanced Light Trapping in Silicon Solar Cells. *Optics Express* **2016**,

24, A191.

[108] Razzaq, A.; Depauw, V.; Cho, J.; Radhakrishnan, H. S.; Gordon, I.; Szlufcik, J.; Abdulraheem, Y.; Poortmans, J. Periodic Inverse Nanopyramid Gratings for Light Management in Silicon Heterojunction Devices and Comparison with Random Pyramid Texturing. *Solar Energy Materials and Solar Cells* **2020**, *206*, 110263.

[109] Zhao, Y.; Zhang, K.; Li, H.; Xie, C. Fabrication and Characterization of Inverted Silicon Pyramidal Arrays with Randomly Distributed Nanoholes. *Micromachines* **2021**, *12*, 931.

[110] Lindquist, N. C.; Nagpal, P.; Lesuffleur, A.; Norris, D. J.; Oh, S. H. Three-Dimensional Plasmonic Nanofocusing. *Nano Letters* **2010**, *10*, 1369.

[111] Alba, M.; Pazos-Perez, N.; Vaz, B.; Formentin, P.; Tebbe, M.; Correa-Duarte, M. A.; Granero, P.; Ferré-Borrull, J.; Alvarez, R.; Pallares, J.; Fery, A.; De Lera, A. R.; Marsal, L. F.; Alvarez-Puebla, R. A. Macroscale Plasmonic Substrates for Highly Sensitive Surface-Enhanced Raman Scattering. *Angewandte Chemie - International Edition* **2013**, *52*, 6459.

[112] Rigó, I.; Veres, M.; Pápa, Z.; Himics, L.; Öcsi, R.; Hakkel, O.; Fürjes, P. Plasmonic Enhancement in Gold Coated Inverse Pyramid Substrates with Entrapped Gold Nanoparticles. *Journal of Quantitative Spectroscopy and Radiative Transfer* **2020**, *253*, 107128.

[113] Desiatov, B.; Goykhman, I.; Mazurski, N.; Shappir, J.; Levy, U. Plasmonic Enhanced Schottky Detectors Based on Internal Photoemission in Nano Pyramids for near IR Regime. *Optica* **2015**, *2*, 335.

[114] Qi, Z.; Zhai, Y.; Wen, L.; Wang, Q.; Chen, Q.; Iqbal, S.; Chen, G.; Xu, J.; Tu, Y. Au Nanoparticle-Decorated Silicon Pyramids for Plasmon-Enhanced Hot Electron near-Infrared Photodetection. *Nanotechnology* **2017**, *28*, 275202.

[115] Syu, H.-J.; Chuang, H.-C.; Lin, M.-J.; Cheng, C.-C.; Huang, P.-J.; Lin, C.-F. Ultra-Broadband Photoresponse of Localized Surface Plasmon Resonance from Si-Based Pyramid Structures. *Photonics Research* **2019**, *7*, 1119.

[116] Zhai, Y.; Li, Y.; Ji, J.; Wu, Z.; Wang, Q. Hot Electron Generation in Silicon Micropyramids Covered with Nanometer-Thick Gold Films for Near-Infrared Photodetectors. *ACS Applied Nano Materials* **2020**, *3*, 149.

[117] Dore, C.; Osmond, J.; Mihi, A. A Water-Processable Cellulose-Based Resist for Advanced Nanofabrication. *Nanoscale* **2018**, *10*, 17884.

[118] Kelf, T. A.; Sugawara, Y.; Baumberg, J. J.; Abdelsalam, M.; Bartlett, P. N. Plasmonic Band Gaps and Trapped Plasmons on Nanostructured Metal Surfaces. *Physical Review Letters* **2005**, *95*, 116802.

[119] Gao, H.; McMahon, J. M.; Lee, M. H.; Henzie, J.; Gray, S. K.; Schatz, G. C.; Odom, T. W. Rayleigh Anomaly-Surface Plasmon Polariton Resonances in Palladium and Gold Subwavelength Hole Arrays. *Optics Express* **2009**, *17*, 2334.

[120] Kumarasinghe, C. S.; Premaratne, M.; Bao, Q.; Agrawal, G. P. Theoretical Analysis of Hot Electron Dynamics in Nanorods. *Scientific Reports* **2015**, *5*, 12140.

[121] Giugni, A.; Torre, B.; Toma, A.; Francardi, M.; Malerba, M.; Alabastri, A.; Proietti Zaccaria, R.; Stockman, M. I.; Di Fabrizio, E. Hot-Electron Nanoscopy Using Adiabatic Compression of Surface Plasmons. *Nature Nanotechnology* **2013**, *8*, 845.

[122] Knight, M. W.; Sobhani, H.; Nordlander, P.; Halas, N. J. Photodetection with Active Optical Antennas. *Science* **2011**, *332*, 702.

[123] Li, W.; Valentine, J. G. Harvesting the Loss: Surface Plasmon-Based Hot Electron Photodetection. *Nanophotonics* **2017**, *6*, 177.

[124] Cushing, S. K.; Wu, N. Progress and Perspectives of Plasmon-Enhanced Solar Energy Conversion. *J. Phys. Chem. Lett.* **2016**, *7*, 666.

[125] Jang, Y. H.; Jang, Y. J.; Kim, S.; Quan, L. N.; Chung, K.; Kim, D. H. Plasmonic Solar Cells: From Rational Design to Mechanism Overview. *Chemical Reviews* **2016**, *116*, 14982.

[126] Sönnichsen, C.; Franzl, T.; Wilk, T.; von Plessen, G.; Feldmann, J.; Wilson, O.; Mulvaney, P. Drastic Reduction of Plasmon Damping in Gold Nanorods. *Physical Review Letters* **2002**, *88*, 774021.

[127] Melikyan, A.; Minassian, H. On Surface Plasmon Damping in Metallic Nanoparticles. *Applied Physics B: Lasers and Optics* **2004**, *78*, 453.

[128] Hasegawa, K.; Nöckel, J. U.; Deutsch, M. Curvature-Induced Radiation of Surface Plasmon Polaritons Propagating around Bends. *Physical Review A-Atomic, Molecular, and Optical Physics* **2007**, *75*, 063816.

[129] Issa, N. A.; Guckenberger, R. Fluorescence near Metal Tips: The Roles of Energy

References

Transfer and Surface Plasmon Polaritons. *Optics Express* **2007**, *15*, 12131.

[130] Wiener, A.; Fernández-Domínguez, A. I.; Horsfield, A. P.; Pendry, J. B.; Maier, S. A. Nonlocal Effects in the Nanofocusing Performance of Plasmonic Tips. *Nano Letters* **2012**, *12*, 3308.

[131] Bharadwaj, P.; Bouhelier, A.; Novotny, L. Electrical Excitation of Surface Plasmons. *Physical Review Letters* **2011**, *106*, 226802.

[132] Kats, M. A.; Yu, N.; Genevet, P.; Gaburro, Z.; Capasso, F. Effect of Radiation Damping on the Spectral Response of Plasmonic Components. *Optics Express* **2011**, *19*, 21748.

[133] Wen, G.; Zou, X.; Hu, R.; Peng, J.; Chen, Z.; He, X.; Dong, G.; Zhang, W. Ground- And Excited-State Characteristics in Photovoltaic Polymer N2200. *RSC Advances* **2021**, *11*, 20191.

[134] Su, W.; Meng, Y.; Guo, X.; Fan, Q.; Zhang, M.; Jiang, Y.; Xu, Z.; Dai, Y.; Xie, B.; Liu, F.; Zhang, M.; Russell, T. P.; Li, Y. Efficient and Thermally Stable All-Polymer Solar Cells Based on a Fluorinated Wide-Bandgap Polymer Donor with High Crystallinity. *Journal of Materials Chemistry A* **2018**, *6*, 16403.

[135] Yan, Y.; Liu, Y.; Zhang, Q.; Han, Y. Increasing N2200 Charge Transport Mobility to Improve Performance of All Polymer Solar Cells by Forming a Percolation Network Structure. *Frontiers in Chemistry* **2020**, *8*.

[136] Lee, H.; Lee, Y. K.; Hwang, E.; Park, J. Y. Enhanced Surface Plasmon Effect of Ag/TiO$_2$ Nanodiodes on Internal Photoemission. *Journal of Physical Chemistry C* **2014**, *118*, 5650.

[137] Pelayo García De Arquer, F.; Mihi, A.; Konstantatos, G. Molecular Interfaces for Plasmonic Hot Electron Photovoltaics. *Nanoscale* **2015**, *7*, 2281.

[138] Medintz, I.; Hildebrandt, N. *FRET – Förster Resonance Energy Transfer*; Wiley-VCH, **2013**.

[139] Lin, K. Te; Chen, H. L.; Lai, Y. S.; Yu, C. C. Silicon-Based Broadband Antenna for High Responsivity and Polarization-Insensitive Photodetection at Telecommunication Wavelengths. *Nature Communications* **2014**, *5*, 3288.

[140] Wen, L.; Chen, Y.; Liu, W.; Su, Q.; Grant, J.; Qi, Z.; Wang, Q.; Chen, Q. Enhanced Photoelectric and Photothermal Responses on Silicon Platform by Plasmonic

Absorber and Omni-Schottky Junction. *Laser and Photonics Reviews* **2017**, *11*, 1700059.

[141] Wen, L.; Chen, Y.; Liang, L.; Chen, Q. Hot Electron Harvesting via Photoelectric Ejection and Photothermal Heat Relaxation in Hotspots-Enriched Plasmonic/Photonic Disordered Nanocomposites. *ACS Photonics* **2018**, *5*, 581.